Projections of Sea Level Along the East Coast of North America

Ryan Love

Thesis submitted to the
Faculty of Graduate and Postdoctoral Studies
in partial fulfillment of the requirements
for the Master's degree in Physics

Department of Physics
Faculty of Science
University of Ottawa

Abstract

Projections of sea level rise for the east coast of North America at 2100CE were generated considering contributions from: ocean warming, land ice melting and isostatic land motion. The primary contribution of this study is the development of an improved glacial isostatic adjustment (GIA) model that includes an assessment of model uncertainty using 36 ice loading histories, 363 Earth models and a new sea level proxy database comprising over 500 sea level index points. We find that, while there are differences between our projections and the global mean sea level (GMSL) projections from the recent International Panel on Climate Change (IPCC) Assessment Report, the two sets of results agree to within uncertainty largely because some of the regional processes cancel. Our results indicate that the isostatic signal is large, contributing up to 1/4 of sea level change at 2100CE, and so must be included to generate accurate projections for this region.

Contents

List of Tables

List of Figures

Acronyms

AOGCM Atmosphere Ocean General Circulation Model. 19, 38, 39, 42

CMIP5 Coupled Model Intercomparison Project Phase 5. 19, 20, 38, 39, 42, 51

CSR Center for Space Research. 43–45, 47

GFZ Deutsches GeoForschungsZentrum. 43, 45, 47

GIA glacial isostatic adjustment. i, 1, 2, 5, 6, 8, 11, 12, 20, 22, 23, 25, 27, 28, 32, 34–37, 57–61

GICs glaciers and ice caps. 15, 37, 51, 52, 54, 56–58, 60

GMSL global mean sea level. i, 18, 19, 36, 37, 39, 42, 50, 58

GPS global positioning systems. 7

GRACE Gravity Recovery and Climate Experiment. 43–45, 47, 48

IPCC International Panel on Climate Change. i, 1, 16, 18, 36, 37, 39, 40, 42, 44, 47, 49, 50, 58

JPL Jet Propulsion Laboratory. 43–45, 47

LGM Last Glacial Maximum. 2, 9, 10, 34

LMV lower mantle viscosity. 25, 28, 30, 34, 36

NAIS North American Ice Sheet. 8, 30

PREM Preliminary Reference Earth Model. 6, 7

RCP Representative Concentration Pathway. 16, 17, 36, 39–41, 51, 52, 57, 60

RGI Randolph Glacier Inventory. 18, 21, 51–53, 55

RSL relative sea level. 1, 2, 5, 8, 16, 20, 22, 25–29, 32, 34–36

SLIP sea level index point. 24–27, 29

UMV upper mantle viscosity. 25, 28, 30, 34, 36

Thanks

My greatest thanks are to my supervisor Dr. Glenn Milne, without whom I know I could not have accomplished what I have thus far. Your guidance and advice has has let me see this project from its inception through to this conclusion. To Martin Wolstencroft, many thanks for your advice at the outside of this project, it helped to get things off the ground and on firm footing. To Candice, your patience and love helped to keep me going when events conspired to halt me in my tracks.

Chapter 1

Introduction

1.1 Motivation

Changing sea level is an inevitable consequence of an ever changing climate. We live in an age that has seen some of the highest rates of sea level rise that have been observed in the last few millennia (Church et al. [2013]). Similarly, it is also expected that sea level will continue to rise past the close of the 21st century. Changing sea level is of greatest importance to those who live along coastlines, particularly those in the developing world, however the impacts of changing sea level will be felt globally. This work examines the changes of sea level for the East Coast of North America from ≈ 10 kybp to the close of the current century. Due to the long time scale of one of the primary contributors to relative sea level (RSL) change for the East Coast of North America, glacial isostatic adjustment (GIA), we are required to examine how sea level has changed in the past to determine how it can change in the future.

Two useful metrics to examine the impact that changing sea levels can have are: the population that may be directly exposed to changes in sea level and the values of the assets exposed to changes in sea level. To give a measure of the importance of changing sea level we look at the work of Hanson et al. [2011] which provides values of these metrics for major coastal cities, several of which are in our region of interest. In particular, New York City, NY, USA currently has a population of $1,540,000$ people who are exposed to coastal flooding, and that number is projected to increase to $2,931,000$ by the year 2070 when taking into account both climate[1] and socio-economic change. Miami, FL, USA, while only having of the order of $2,000$ people exposed at present, is projected to have $4,795,000$ exposed by 2070. With regards to the economic exposure, New York City currently has \$320.20 billion in USD increasing to \$$2,147.35$ billion in USD by 2070. Similarly, Miami currently has \$416.29 billion USD is exposed assets and that is projected to increase almost $10\times$ to \$$3,513.04$ by 2070.

Consequences of climate change are of course not isolated to large urban areas, Figure 1.1 demonstrates that there is significant population along the East Coast of North America. As well, examining Figure 1.2 one can easily see that there are large areas which are vulnerable to sea level rise of the

[1]The work of Hanson et al. [2011] assumes an increase in relative sea level of $50cm$ globally, which is of the same order of magnitude as well as consistent with the latest work by the International Panel on Climate Change (IPCC) and results of this body of work.

order of 1 m, a figure which can become magnified due to processes such as storm surges and tides. Studies such as this can aid policy makers and planners in preparing for changing sea levels by placing bounds on possible changes in a given location.

1.2 Introduction to Sea Level

Changes in sea level, in particular RSL, are the central theme of this study. Sea level may be defined in two ways; the definition that is used for this work is the height of the sea surface relative to the solid Earth surface, see 'relative sea level' on Figure 1.3. We can measure this kind of sea level directly through the use of devices such as tide gauges. Tide gauges have been used in some locations for centuries and provide a diverse and rich history of modern changes in sea level for various places in the world, albeit with some limitations. The other definition is the radial distance from the sea surface to the center of mass of the Earth, see 'geocentric sea level' on Figure 1.3. We can measure geocentric sea level through the use of remote sensing devices like satellites and these devices allow us to obtain global coverage maps of changes in sea level however over a much smaller window of time.

Sea level is affected by many varying processes such as changes in ocean properties(temperature, salinity), influx of water due to melting land ice, perturbations to the Earth's gravitational field and more. Figure 1.3 diagrams some of the primary climate-related mechanisms by which changes in sea level can happen. The cause of changes in sea level which are most familiar are changes in land ice volume, however not entirely for the reasons one initially expects. While mass does flow into the oceans from melting land ice, one of the other primary mechanisms involved in the change of sea level relates to the perturbation to the gravitational field caused by this migration of mass from the body of ice to the oceans. This effect is explored further in 1.2.1. Another primary cause of sea level change is the thermal expansion of water due to changes in temperature of the water, known as thermosteric changes in sea level. A similar sea level change due to differences in density arising from changes in salinity are defined as halosteric changes in sea level. Much of the heat uptake of the oceans takes place in the upper layers. These changes are not globally uniform, and there are regions of both expansion and contraction, this spatial information is garnered though the use of models of the climate system. Other interactions between the atmosphere and the oceans are similarly treated and their effects investigated by modelling the climate system in coupled models. As well, all of these effects can strongly influence ocean currents which in turn enact their own changes in sea level through their influence on the height of the ocean surface (so-called 'dynamic topography') and affecting the internal density structure of the oceans. These processes are captured in coupled climate models (see Section 3.2). Finally, there are also the changes due to GIA which relate primarily to changes in the solid Earth. GIA is the on-going response of the solid Earth to past land ice melting that is dominated by the recent transition of the climate system from a glacial maximum to the current interglacial period. Since the surface of the Earth was loaded with large ice sheets ice and many of these have disappeared or reduced in size since the Last Glacial Maximum (LGM) due to changes in the climate system, the solid Earth is rebounding to this unloading of mass and subsequently effecting a change in RSL. More detail on this process is presented in Section 1.2.1.

All of the processes introduced in the above paragraph are investigated in this work with respect

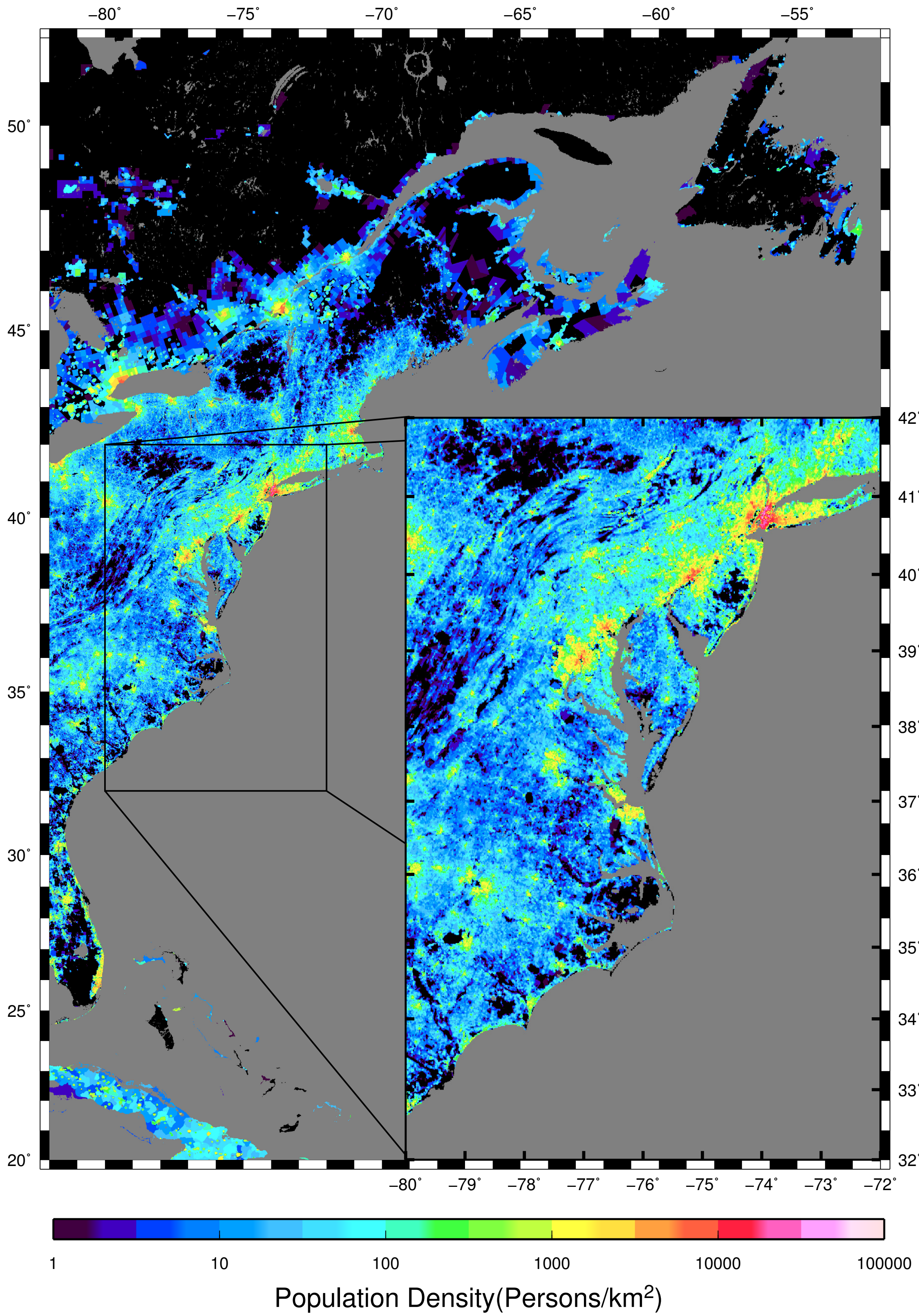

Figure 1.1: Population density map for the East Coast of North America; data from the Global Rural-Urban Mapping Project(GRUMP) V1(Center for International Earth Science Information Network - CIESIN - Columbia University et al. [2011], Balk et al. [2006]).

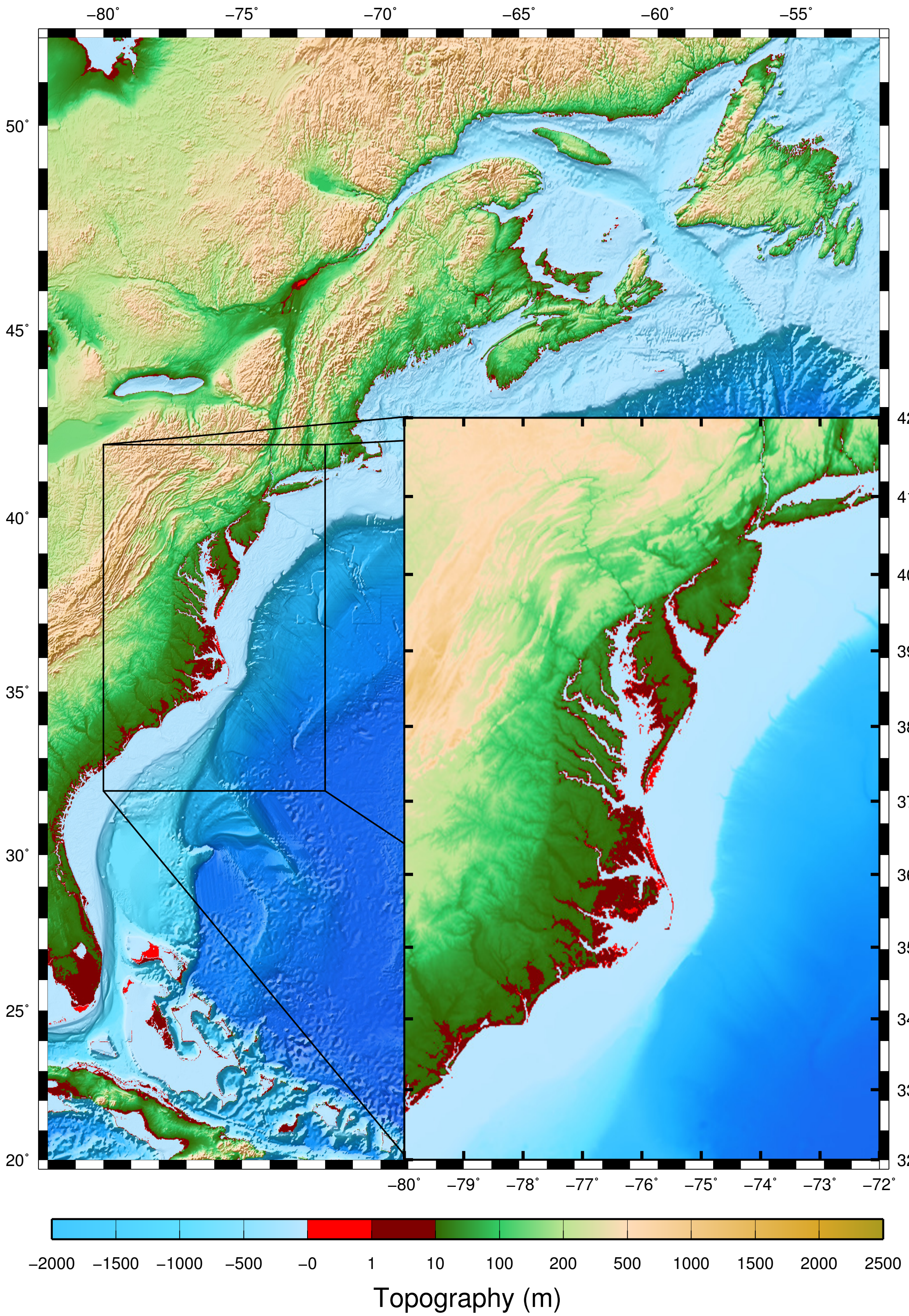

Figure 1.2: Topography map for the East Coast of North America. Regions within 1 m of sea level as defined by the ETOPO1 global topography model(Amante and Eakins [2009]) are highlighted in bright red while regions between 1 m and 10 m of mean sea level are in dark red. The resolution of the ETOPO1 model is 1 arc-minute, ≈ 2 km resolution at the equator. The vertical uncertainty of the ETOPO1 model is ≈ 10 m.

to estimating future changes in RSL along the east coast of North America. As GIA is a primary focus of this thesis, a relatively in-depth introduction to this process and some relevant theory is provided in 1.2.1. The sea level contributions due to future climate change (i.e. thermal expansion of the oceans due to heat uptake and changes in land ice volume) and the methods used to estimate these are introduced in Section 1.2.2.

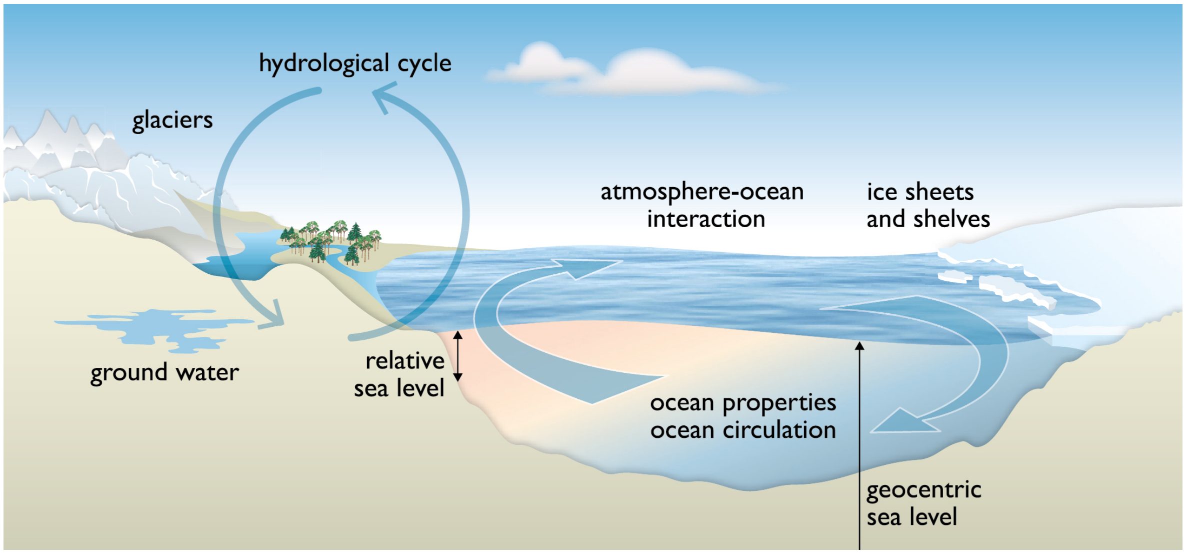

Figure 1.3: Diagram outlining some the major processes which affect sea level(Church et al. [2013]). This work focuses mainly on changes in RSL due to GIA, thermal expansion and changes in land ice volume. Other processes such as ocean-atmosphere interaction and the hydrological cycle are captured in this study by their incorporation into climate models which are also used to determine the contribution due to thermal expansion and changes in ocean properties. Figure obtained from Church et al. [2013] as Figure 13.1

1.2.1 Glacial Isostatic Adjustment

GIA is, at its most concise, the process of the solid Earth rebounding to the unloading of ice from the surface of the Earth. However, GIA is a complex process and so modelling it has many uncertainties which need to be investigated. The two primary uncertainties are the properties of the Earth, such as viscosity and density for a given depth and location, and the loading history, the location and volume of ice for a given point in time. The former can be investigated via various methods such as seismic inversion studies(Dziewonski and Anderson [1981]) as well as through studies such as this. The latter is investigated by studies such as those conducted by Peltier [2004] and Tarasov et al. [2012]. Such reconstructions of ice history typically can also use knowledge of GIA and can use studies such as this to then refine their results and inputs.

In order to extract useful information from a model we need to compare model output to measurements of the real world so that we may infer the best fitting model parameters. In order to extract information regarding Earth's structure and, in particular, ice volume history we couple a model of GIA to a model of sea level. Using such a model we are able to, for a given solid Earth response and ice history, obtain values of RSL for a given location at a given point in time. We can then compare our modelled sea level history to real-world sea level data. By examining the model-data misfits we garner information about which Earth structure and ice history parameters are preferred by the data. Unfortunately, the timespan we need to examine sea level to effectively constrain GIA model parameters are much longer than that of instrumental sea level observations; therefore, information about sea level is obtained via the geological record to reconstruct past sea level changes using sea level proxies, see Section 2.2.1.

Features of the Solid Earth

The Earth, while familiar as the simple ground we walk on, is significantly more complex than is often considered. To complicate matters further we are unable to directly observe more than the shallow features of the outermost layers of it, with the deepest borehole reaching no more than ≈ 12 km of the 6371 km mean radius of the Earth(Digranes et al. [1996]). Features in the Earth vary not only as a function of depth but, as on the surface, with latitude and longitude and often not monotonically. As a consequence, it is difficult to map the interior of the Earth, although much progress has been made by monitoring the surface response of the solid Earth to earthquakes. Seismic wave inversion studies such as those by Dziewonski and Anderson [1981], Ritsema et al. [2011] have provided constraints on whole Earth (seismic) velocity structure, which can be used, given appropriate assumptions, to infer variations in density and rheology (elasticity and viscosity) - key parameters in GIA models. Most

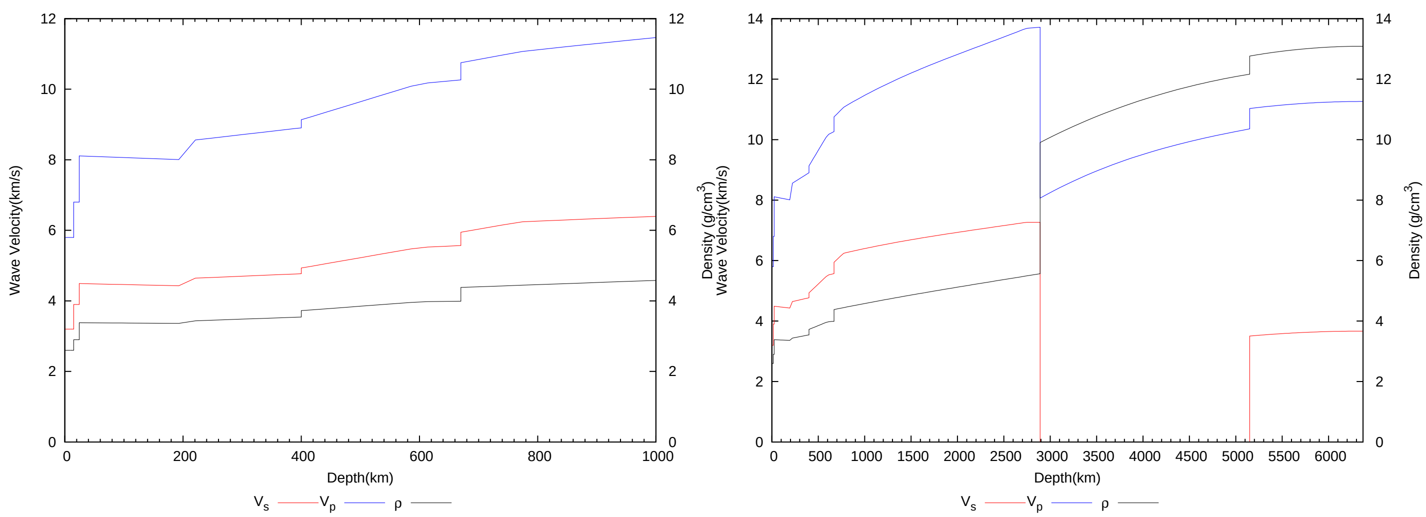

Figure 1.4: Variations of Earth's properties as a function of depth as given by the Preliminary Reference Earth Model (PREM) of Dziewonski and Anderson [1981], ρ is the density, v_p is the p-wave velocity, and v_s is the s-wave velocity.

Earth models used in GIA studies assume that material properties of the Earth vary only as a function of depth and so, the Preliminary Reference Earth Model (PREM) seismic model of Dziewonski and Anderson [1981] is commonly used, details of which can be seen in Figure 1.4. In many GIA models, including the one applied here, PREM is used to define Earth elastic and density structure with gravity being computed from the latter. PREM does not provide useful constraints on viscous structure and so this is constrained as part of the GIA modelling procedure. When more complex Earth models with 3D structure are considered, lateral variations in seismic wave speeds, such as those from S40RTS Ritsema et al. [2011] are employed to infer lateral variations in other GIA-relevant parameters(Latychev et al. [2005]). Figure 1.5 exemplifies the amplitude and scale of lateral variations that can occur in seismic wave velocity in the interior of the Earth. We can see that our region of interest, which the data in Figure 1.5 transects, includes a transition from low to high velocity moving northwards.

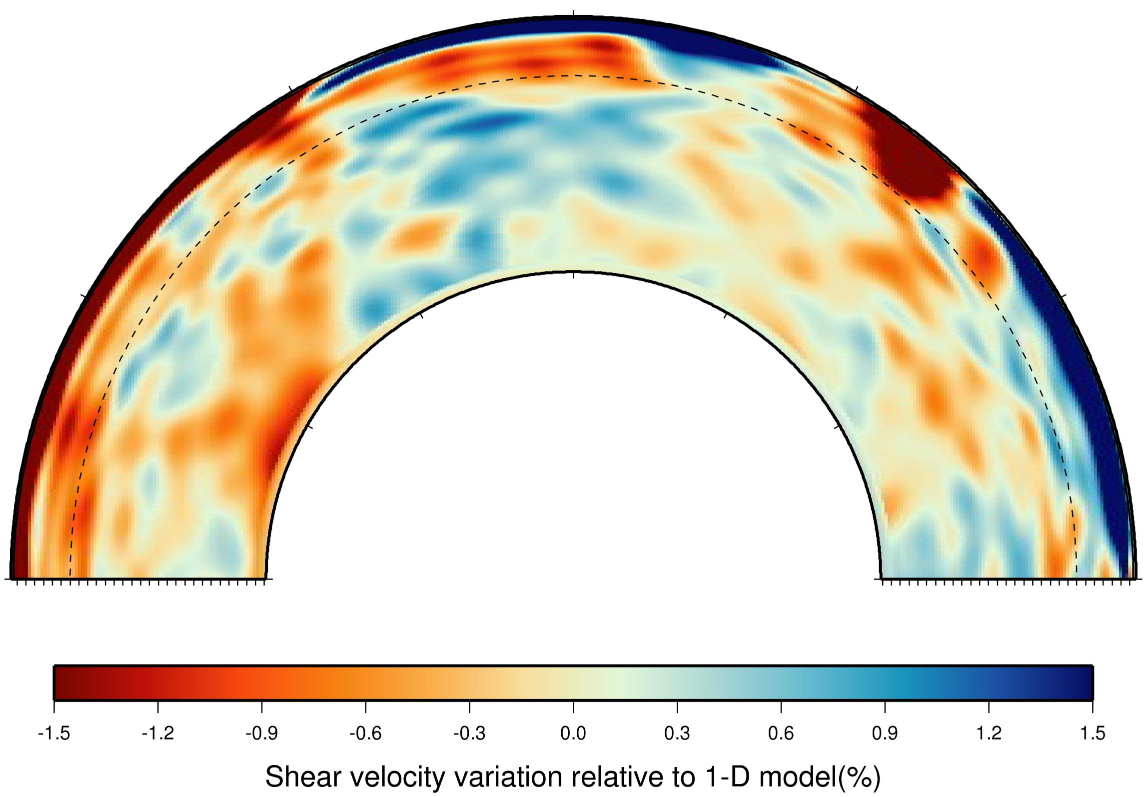

Figure 1.5: A cross-section[2] of velocity perturbations relative to PREM from the base of the Earth's mantle to the base of the lithosphere through the S40RTS model of Ritsema et al. [2011]. This cross-section traverses our region of interest with the center of our region of interest positioned at the top of the slice. What is shown is velocity perturbations relative to PREM. The dashed line denotes the transition from upper mantle to lower mantle at the depth of $\approx 660km$. Note that deviations from homogeneity can be large and over short length scales.

Ice Load Reconstruction

Using the geological record it is possible to determine that the Earth has gone through many glacial cycles during its history. The latest glacial cycle reached its maximum at $\approx$ 21 kabp when several large ice sheets covered the Earth's surface(Marshall [2011]), see Figure 1.6 for a sample reconstruction since 21 kabp. Examining Figure 1.6 we can see that much of North America was covered with a

[2] the cross-section has a center of 40° N, −74° E and an azimuth of 36°

minimum of 1 km of ice, and in our region of interest we did not see a retreat of the ice sheet until ≈ 15 kabp with ice remaining nearby until ≈ 9 kabp. It was the mass of these large bodies of ice, and their subsequent mass transfer from the surface of continents to the oceans, that drives much of the present day vertical land motion observed using global positioning systems (GPS). Although these ice complexes were exceptionally large, of the same scale as the present day Antarctic ice sheets in the case of the North American Ice Sheet (NAIS), their distribution and volumes remain imprecisely known. This uncertainty in the ice loading history raises issues for modellers as it presents yet another input parameter set that must be explored and evaluated when comparing model input to data, thus increasing the complexity of interpretation when making such a comparison to infer model parameters. Obtaining a spread in the geography of sea level histories is useful as there are different behaviours of the Earth given the distance from a body of ice. For a location directly under a body of ice the Earth surface will rebound exponentially until it reaches its new equilibrium. The magnitude of the displacement is proportional to the height of ice at the location and so we can infer the location of the greatest height of ice by finding those areas which rebound the swiftest. At the outside edge of the ice sheet the land is displaced upward while the ice is loading the surface, this area is known as the peripheral bulge. Once the body of ice is removed the peripheral bulge subsides back to equilibrium, as is occurring for areas along the east coast of North America.

There are various ways in which to produce an ice loading reconstruction. Some methods, (Peltier [2004]), involve manually tuning the ice thickness distributions to best match model output to observations (such as RSL curves and present-day land uplift rates). However, such an approach often does not take into account the physical laws governing how ice sheets evolve to a changing climate. The other end of the spectrum involves using glaciological models and tuning them to fit an array of observations relating to ice extent and GIA (Tarasov and Peltier [2002]). The limitation of this approach is the large number of parameters required for a glaciological model. Thus, the issue of non-uniqueness often arises. As well, it is a much more time consuming exercise, especially when trying to fully explore the parameter space of a glaciological model(Tarasov et al. [2012]). The work of Tarasov et al. [2012] involves the treatment of the problem of an ice loading history from a Bayesian statistics point of view, in that they compute a probability distribution for the ice loading history given the constraints involved from both field observations as well as the physics surrounding the evolution of ice. Such an approach not only allows the use of the a large dataset but also results in formal uncertainty estimates for the inferred ice loading reconstruction.

Solid Earth Response Theory

GIA is commonly modelled as a combination of two different responses of the solid Earth to an applied stress, a short time-scale elastic response where the material behaves like a Hookean solid and a long time-scale viscous response where the material behaves as a Newtonian fluid. These two response types are accommodated in the Maxwell-viscoelastic rheology, which can be represented by elastic and viscous elements coupled in series. The constitutive equations for the three rheologies mentioned above (elastic, viscous, and viscoelastic) are respectively(Ranalli [1995])

$$\tau_{kl} = 2\mu e_{kl} + \lambda e_{kk}\delta_{kl}, \tag{1.1}$$

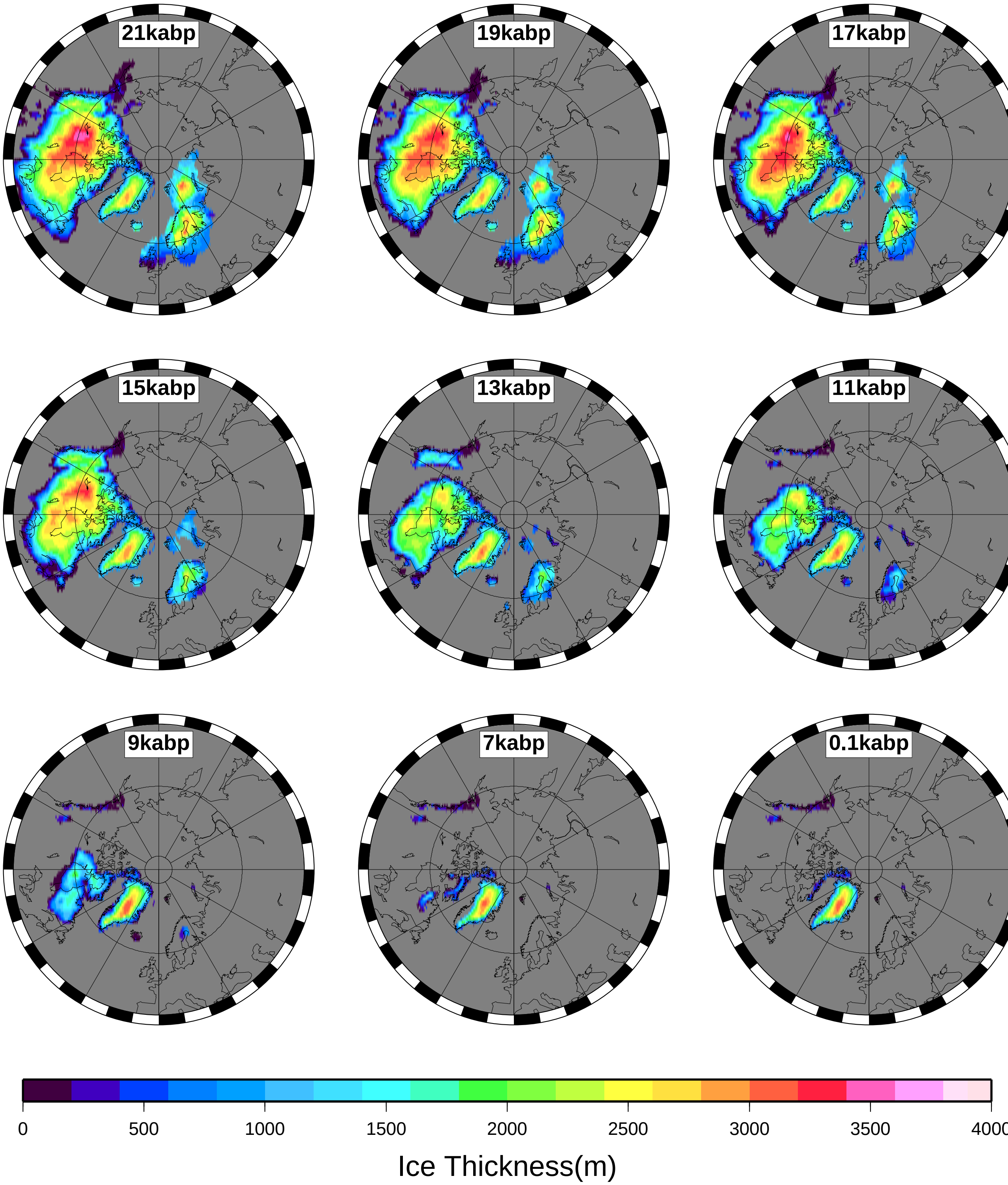

Figure 1.6: The North American ice model reconstruction of Tarasov et al. [2012] combined with the reconstruction of Peltier [2004] since the LGM 21 kabp. The northern hemisphere's ice complexes were significantly more active than their southern counterpart during the most recent de-glaciation, with multiple ice sheets vanishing within $10 - 15$ ka. The Antarctic ice model reconstruction of Peltier [2004] can be seen for comparison in Figure 1.7.

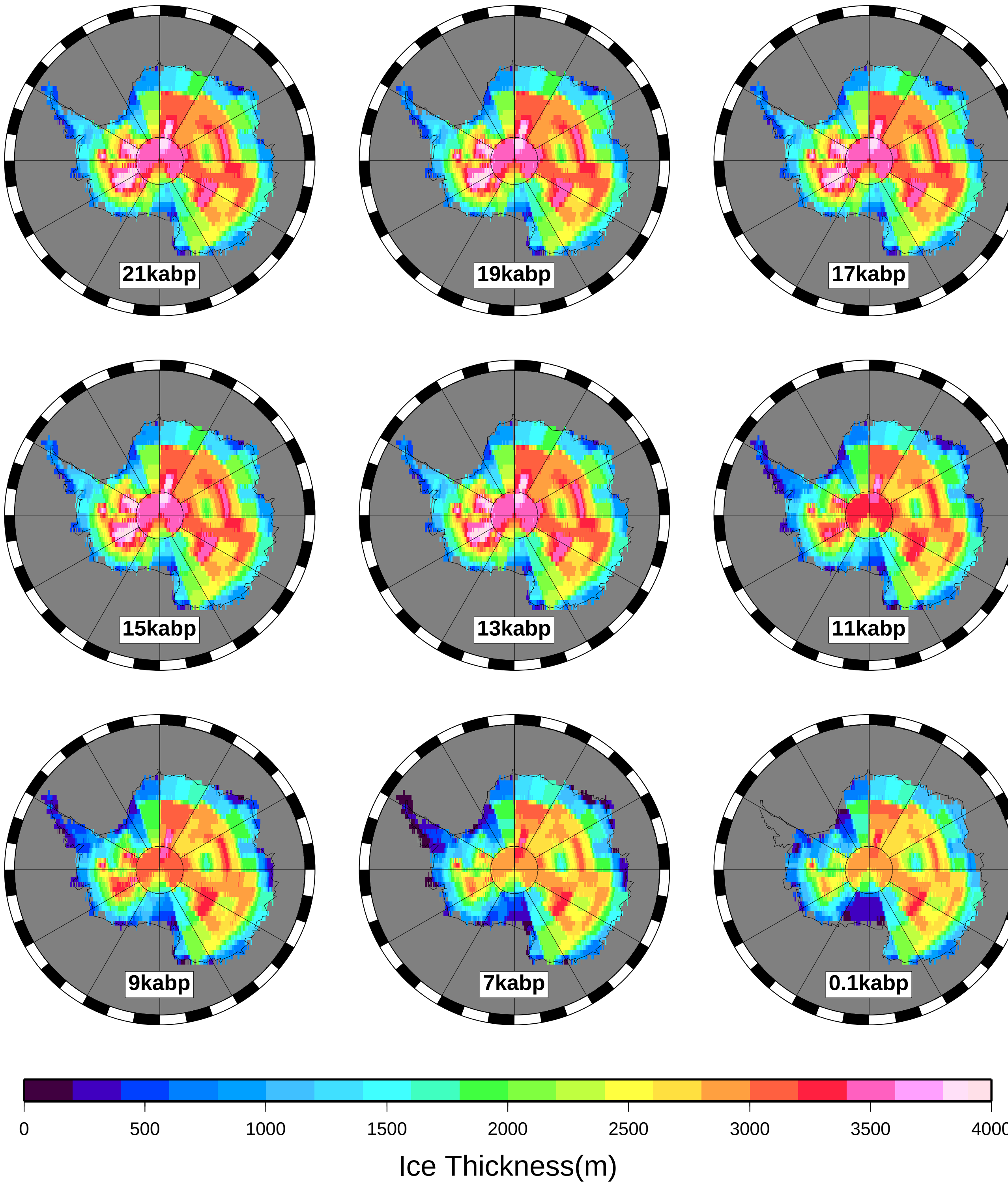

Figure 1.7: The ICE5G ice model reconstruction of Peltier [2004] since the LGM 21 kabp. The Antarctic ice sheets are much less constrained than their more Northern counterparts but reconstructions are improving as Antarctic databases become more comprehensive.

$$\tau_{kl} = 2\nu\dot{e}_{kl}, \tag{1.2}$$

$$\dot{\tau}_{kl} + \frac{\mu}{\nu}\left(\tau_{kl} - \frac{1}{3}\tau_{kk}\delta_{kl}\right) = 2\mu\dot{e}_{kl} + \lambda\dot{e}_{kk}\delta_{kl}, \tag{1.3}$$

where τ_{kl} and e_{kl} are the stress and strain tensors respectively, the over-dot denotes the time derivative of these values, δ_{kl} is the diagonal unit tensor, ν is the viscosity of the material, finally, λ and μ are the elastic Lamé parameters inherent to the material. If we proceed to take the Laplace transform of equation 1.3 we obtain

$$\tilde{\tau}_{kl} = 2\mu(s)\tilde{e}_{kl} + \lambda(s)\tilde{e}_{kk}\delta_{kl}, \tag{1.4}$$

$$\lambda(s) = \frac{\lambda s + \mu K/\nu}{s + \mu/\nu}, \tag{1.5}$$

$$\mu(s) = \frac{\mu s}{s + \mu/\nu}, \tag{1.6}$$

$$K = \lambda + \frac{2}{3}\mu, \tag{1.7}$$

where we now have the viscoelastic moduli, $\lambda(s)$ and $\mu(s)$, the bulk modulus, K, and we use a tilde to denote implicit dependence upon s. Note, that by transforming Equation 1.3, we have effectively obtained an elastic problem since the constitutive equation has the same form as equation 1.3. As such, according to the correspondence theory(Eringen [1967]), solving the elastic problem using the expressions for $\lambda(s)$ and $\mu(s)$ for a range of the transform variable s provides a solution to the viscoelastic problem upon transformation back to the time domain.

To apply this to our problem we take our Earth model to be in a state of gravitationally induced hydrostatic pre-stress. Thus, if we are to perturb this system, its response must satisfy momentum conservation

$$0 = \nabla \cdot \tau_1 + \nabla \cdot (u \cdot \nabla)\tau_0 - \rho_1 \nabla\phi_0 - \rho\nabla\phi_1, \tag{1.8}$$

as well as Poisson's equation that relates deformation to changes in the gravitational field,

$$\nabla^2\phi_1 = -4\pi G(\nabla \cdot u)\rho_0, \tag{1.9}$$

finally, to ensure mass is conserved we utilize the continuity equation

$$\rho_1 = -(\nabla \cdot u)\rho_0, \tag{1.10}$$

where equations 1.9 and 1.10 are to first order only, $\tau_0(r)$, $\rho_0(r)$ and $\phi_0(r)$ are the equilibrium states of stress, density, and gravitational potential respectively and G is the familar gravitational constant. Similarly, $\tau_1(r)$, $\rho_1(r)$ and $\phi_1(r)$ are the perturbations to these values and u is the load induced vector displacement field. The perturbed gravitational potential is a composite of two potentials, ϕ_2 and ϕ_3, the perturbation due to the applied load and the perturbation due to the resultant mass redistribution caused by the load induced deformation. In equation 1.8, the first term is the stress field gradient which perturbs the body from equilibrium, the second term is the advection of pre-stress as a result of the initial elastic displacement as given by Love [1927]. The third term is due to the equilibrium gravitational field acting on the perturbation to the equilibrium density field and acts as a buoyant force. The last term is of the perturbation to the gravitational field acting on the equilibrium density field. Note here that due to the long time-scales involved in GIA, of the order of > 1 ka, that the the inertia term is set to zero. To obtain information regarding the Earth's response we need to express our unknown fields, namely ρ_1 and τ_1 in terms of u and ϕ_1. We can use the expression we obtained for τ previously, equation 1.3 to relate τ_1 to our displacement field. To utilize the correspondence principal here we need to take the Laplace transform of equation 1.8 and utilize equation 1.4 to relate stress to the strain in the Laplace transform domain. Further details of this procedure may be sought out in Wu and Peltier [1982] and Peltier [1974].

The solutions to the viscoelastic problem in the time domain can be expressed as an expansion of Legendre polynomials

$$u(a,\gamma,t) = \sum_{l=0}^{\infty} u_l(a,t) P_l(\cos(\gamma)), \tag{1.11}$$

$$v(a,\gamma,t) = \sum_{l=0}^{\infty} v_l(a,t) \frac{dP_l(\cos(\gamma))}{d\gamma}, \tag{1.12}$$

$$\phi_1(a,\gamma,t) = \sum_{l=0}^{\infty} \phi_{1,l}(a,t) P_l(\cos(\gamma)), \tag{1.13}$$

where $u(a,\gamma,t)$, $v(a,\gamma,t)$, $\phi_1(a,\gamma,t)$ are the horizontal and tangential components of the displacement field and the perturbation to the geo-potential, respectively, each of which are defined at the surface of the unperturbed Earth (where $r = a$). P_l and γ are the Legendre polynomials and the great circle angle from the impulse load to the observation point respectively. The Legendre coefficients are defined as follows:

$$u_l(a,t) = u_l^E \delta(t) + \sum_{k=1}^{K} \delta u_{l,k}^V \exp(-s_k^l t), \tag{1.14}$$

$$v_l(a,t) = v_l^E \delta(t) + \sum_{k=1}^{K} \delta v_{l,k}^V \exp(-s_k^l t), \tag{1.15}$$

$$\phi_{1,l}(a,t) = \phi_{1,l}^E \delta(t) + \sum_{k=1}^{K} \delta \phi_{1,l,k}^V \exp(-s_k^l t). \tag{1.16}$$

Examining these equations we can see that the coefficients $u_l(a,t)$, $v_l(a,t)$, and $\phi_{1,l}(a,t)$ are a sum of two responses: an instantaneous elastic response(denoted by the superscript E) and a time varying viscous response(denoted by the superscript V). The elastic response is an instantaneous response to the loading given the presence of the Dirac delta function, whereas the viscous response is comprised of exponential decay weighted by the δu, δv, $\delta \phi$ coefficients. Rather than use these coefficients directly to determine the GIA response, it is more common to utilize a triplet of non-dimensional values known as viscoelastic Love Numbers which are functions of l,r and s. We can relate these Love numbers to our coefficients by

$$\begin{pmatrix} h_l^L(t) \\ l_l^L(t) \\ k_l^L(t) \end{pmatrix} = \frac{g}{\phi_{2,l}(a)} \begin{pmatrix} u_l(a,t) \\ v_l(a,t) \\ -\frac{\Phi_{3,l}(a,t)}{g} \end{pmatrix} \tag{1.17}$$

where h_l^L, l_l^L, and k_l^L are the degree l Love numbers associated with the surface load (which is denoted by the superscript L, there are also Love numbers associated with a general forcing not due to a load on the surface of the Earth such as body tides due to other planetary bodies and the rotational potential from the rotation of the Earth about its axis). As well, h, l, k are associated with the radial and tangential components of the displacement field and perturbation to the gravitational field, respectively. Similarly, $\phi_{2,l}(a)$ is the degree l Legendre expansion of the perturbation to the gravitational field and g is the familiar gravitational acceleration at the surface of the Earth. Now, to utilize these Love numbers to determine quantities we can observe and use such as land motion and changes in gravity we need to construct a Green's function, the exact details of which can be sought out in Peltier [1974]. The Green's function for radial displacement is

$$G_r(\gamma, t) = \frac{a}{M_E} \sum_{l=0}^{\infty} (h(t)_l^L) P_l(cos\gamma). \tag{1.18}$$

Similar expressions for the gravitational perturbation and tangential components can be constructed. Now to determine the response of the Earth due to an unloading event (which we will take to occur instantaneously at $t = 0$, and use a Heaviside function to accomplish this) we need only convolve the relevant Green's function with the loading function $L(\theta, \lambda)$ where θ is the co-latitude[3] and λ is the East longitude[4]. The Green's function is

$$\Delta R(\theta, \lambda, t) = \int\int d\Omega \int_0^t G_r(\theta - \theta', \lambda - \lambda', t - t') H(t') L(\theta', \lambda') dt' \tag{1.19}$$

where H is the Heaviside function and $d\Omega$ is the element surface area. Solving the above integration gives us the radial displacement response to the loading. Again similar such equations can be constructed for the other Green's functions and the reader is directed to Peltier and Andrews [1976] for further details on this procedure.

The Sea Level Equation

Contrary to what could be ones first intuition, changes in sea level due to melting land ice are not globally uniform. Changes in sea level have a complex spatial pattern in even the simplest of cases, such as will be demonstrated shortly. The primary reason for these complex patterns is that the ocean surface is bounded to rest at a gravitational equipotential[5], the geoid, and as such any changes to the Earth's gravitational field cause a subsequent change in sea level. Changes in sea level for a model of reasonable complexity and capacity to represent the Earth system require solving via numerical means. Much of the initial theoretical framework for changes in sea level is outlined in Farrell and Clark [1976]. Over the subsequent decades the theory was expanded through various other works, much of which is summarised in Mitrovica and Milne [2003] and Kendall et al. [2005]. For the simplest case of a uniform and a rigid Earth an analytical solution which describes this departure from uniformity may be obtained. For such a body with radius a, the gravitational potential on and above the surface at a

[3]Degrees latitude difference between 90° and the latitude

[4]Longitude measured East of the Prime Meridian

[5]This is true if we neglect high frequency variations in sea level such as waves, localized weather systems and the like. Such effects as these can all cause sea level to depart from the equipotential on short time scales.

distance of r can be expressed as

$$\phi(r) = \frac{GM_E}{r} \qquad r \geq a \tag{1.20}$$

where G is the usual gravitational constant and M_E is the mass of the Earth. Now, should we perturb the gravitational field of this body by removing a uniform layer of water from the surface of the body, with mass M_I, and collect it into a point body of ice at the co-ordinates of $r = a, \theta = 0$ whereas θ is the angular distance from the body of ice we obtain a new gravitational potential function

$$\phi^*(r,\theta) = \frac{G(M_E - M_I)}{r} + \frac{GM_I}{\sqrt{r^2 + a^2 - 2ar\cos(\theta)}}. \tag{1.21}$$

By evaluating 1.21 at the Earth's surface we find that it is not constant and as such $r = a$ cannot be a possible surface for ocean surface because, as was mentioned before, ocean surface is bound to rest on a gravitational equipotential. If we seek out a new equipotential, we can determine that there is one quite close at a radial distance of $\epsilon(\theta)$ from a such that

$$\phi^*(a + \epsilon, \theta) = \phi(a). \tag{1.22}$$

Since $M_I \ll M_E$ we can safely expect $\epsilon \ll a$ and as such we can take $\phi^*(a + \epsilon, \theta)$ to first order as

$$\phi^*(a + \epsilon, \theta) = \phi^*(a, \theta) + \epsilon \frac{\partial \phi^*(a, \theta)}{\partial r}. \tag{1.23}$$

As well, to the level of accuracy we require $\partial\phi^*/\partial r = \partial\phi/\partial r = -g$, where g is the usual gravitational acceleration at the surface, therefore we can obtain an expression for $\epsilon(\theta)$

$$\epsilon(\theta) = \frac{\phi^*(a, \theta) - \phi(a)}{g}. \tag{1.24}$$

Using the typical form for g as $g = GM_E/a^2$ we can obtain the following form for $\epsilon(\theta)$

$$\epsilon(\theta) = \frac{M_I a}{M_E}\left(\frac{1}{2\sin(\theta/2)} - 1\right). \tag{1.25}$$

While we have found an equipotential at $r = a + \epsilon$ we have not accounted for the volume which was lost from the oceans in forming the point mass of ice. If our value of $a + \epsilon$ is an equipotential then $a + \epsilon + c = a + \epsilon^*$, where $c \ll a$ is a constant, must also be an equipotential. We can determine the form of c by invoking the conservation of mass. As the volume between $r = a$ and $r = a + \epsilon$ is 0 we have

$$\int_0^\pi 2\pi\rho_w c a^2 \sin(\theta) d\theta + M_I = 0, \tag{1.26}$$

$$a^3 = \frac{3}{4\pi}\frac{M_E}{\rho_E}. \tag{1.27}$$

where we have ρ_w and ρ_E as the density of sea water the mean density of the Earth respectively. Solving for c we obtain

$$c = -\frac{M_I}{M_E}\frac{a\rho_E}{3\rho_w}. \tag{1.28}$$

Now we can obtain an expression for $\epsilon + c = \epsilon^*$

$$\epsilon^*(\theta) = \frac{M_I a}{M_E}\left(\frac{1}{2\sin(\theta/2)} - 1 - \frac{\rho_E}{3\rho_w}\right). \tag{1.29}$$

In order to examine the effect that this can have, we can use the ratio of the change that occurs as expressed above to that which would occur if the gravitational effects were neglected

$$R = \left(\frac{1}{2\sin(\theta/2)} - 1 - \frac{\rho_E}{3\rho_w}\right)\left(\frac{\rho_E}{3\rho_w}\right)^{-1}. \tag{1.30}$$

Examining this ratio we can see that near the point body of ice that the effect can be quite large with a resulting large positive change in sea level, but with larger values of θ the effect is $\approx 30\%$ lower sea level than would be expected when considering mass conservation alone and no pertubations to the gravitational field. Now, in this study, we typically will consider changes in ice mass that result in smaller bodies of ice. These same arguments still apply with the exception that the effect has the opposite sign. That is, near a shrinking body of ice sea level will drop locally whereas further away from the body of ice the sea level will rise above the global average. This is an effect which we will see arise again when we consider mass changes in both the glaciers and ice caps (GICs) and the ice sheets. Even with this almost simplest of examples we obtain drastic spatial differences in sea level. This is among the simplest of cases which can be considered in this framework, more complex cases are presented in Farrell and Clark [1976]. We go on to discuss attributes of the full sea level equation below, the net result of which is added complexity in regards to the deformational response of the solid Earth, more complex bodies of ice and changes through time. For this part of the discussion, sea level will be defined as the height difference between the geoid, the gravitational equipotential that the sea surface rests at, and the surface of the solid Earth, G and R respectively. We define θ, ψ and t_j as the colatitude, longitude and time at time-step j and define sea level as follows

$$SL(\theta, \psi, t_j) = G(\theta, \psi, t_j) - R(\theta, \psi, t_j). \tag{1.31}$$

Note that the fields G and R can be computed using the Love number approach outlined previously, see Equations 1.18 and 1.19. We also define topography as the inverse of this field

$$T(\theta, \psi, t_j) = -SL(\theta, \psi, t_j) = R(\theta, \psi, t_j) - G(\theta, \psi, t_j). \tag{1.32}$$

The depth of the ocean is described as the projection of global sea level onto ice-free oceans. We further define two additional fields, our ocean function and grounded ice function, $C(\theta, \phi, t_j)$ and $\beta(\theta, \phi, t_j)$ respectively as follows

$$C(\theta, \psi) = \begin{cases} 1 & : SL(\theta, \psi, t_j) > 0 \\ 0 & : SL(\theta, \psi, t_j) \leq 0 \end{cases} \tag{1.33}$$

$$B(\theta,\psi,t_j) = \begin{cases} 1 & : \text{ no grounded ice} \\ 0 & : \text{ grounded ice} \end{cases} \tag{1.34}$$

Determining sea level relative to a reference time, t_0 is frequently considered and as such we will define topography, the geoid and the ocean function in a similar manner

$$SL(\theta,\psi,t_j) = SL(\theta,\psi,t_0) + \Delta SL(\theta,\psi,t_j), \tag{1.35}$$

$$T(\theta,\psi,t_j) = T(\theta,\psi,t_0) + \Delta T(\theta,\psi,t_j), \tag{1.36}$$

$$G(\theta,\psi,t_j) = G(\theta,\psi,t_0) + \Delta G(\theta,\psi,t_j), \tag{1.37}$$

$$C(\theta,\psi,t_j) = C(\theta,\psi,t_0) + \Delta C(\theta,\psi,t_j), \tag{1.38}$$

$$B(\theta,\psi,t_j) = B(\theta,\psi,t_0) + \Delta B(\theta,\psi,t_j). \tag{1.39}$$

We can then obtain,

$$\Delta SL(\theta,\psi,t) = \Delta G(\theta,\psi,t_0) - \Delta R(\theta,\psi,t), \tag{1.40}$$

and from these we can obtain a form for the generalized sea level equation,

$$\Delta S(\theta,\phi,t_j) = \Delta SL(\theta,\phi,t_j)C(\theta,\phi,t_j)B(\theta,\phi,t_j) - T(\theta,\phi,t_0)[C(\theta,\phi,t_j)B(\theta,\phi,t_j) - C(\theta,\phi,t_0)B(\theta,\phi,t_0)]. \tag{1.41}$$

It is this generalized form of the sea level equation which outlines the theoretical base of much of this research. For a thorough discussion of the numerical solving of this equation see the work of Kendall et al. [2005]. There are two useful applications of this theory, the primary use is in conjunction with the theory outlined in 1.2.1 along with an ice loading history to calculate the ongoing RSL response to past changes in ice. The secondary use is to solve the sea level equation to determine the contribution from a future change in ice volume, as we use later to determine the spatial pattern of sea level change from the melting of a glacier complex or mass changes in an ice sheet, known as a sea level fingerprint (Mitrovica et al. [2001]). e

1.2.2 Climate Change

Representative Concentration Pathways

The Representative Concentration Pathway (RCP)s of the IPCC (IPCC) are an interesting blend of geophysical science, climatology and sociology. Each one is an attempt to distil possible future changes in world politics, technological developments and emissions laws among many other factors that can affect climate into inputs which can be used as a forcing for a model. Each RCP is a scenario that is composed of time series of emissions and concentrations of greenhouse gases, aerosols, chemically active gasses, and land usage/coverage. To conveniently compare and discuss the RCPs, the metric of radiative forcing is used. Radiative forcing is the net change in radiative flux at the tropopause, a boundary layer in the atmosphere that separates the troposphere from the stratosphere, relative to the global and annual average of the year 1750. There are four main RCPs, denoted by their radiative forcing at the year 2100, RCP2.6, RCP4.5, RCP6.0 and RCP8.5 each with 2.6 Wm^{-2}, 4.5 Wm^{-2}, 6.0 Wm^{-2}, and 8.5 Wm^{-2} respectively.

Of all the scenarios RCP2.6 is the most optimistic, it has a steady increase in radiative forcing with a peak at 3.0 Wm^{-2} before levelling off and decreasing to 2.6 Wm^{-2}. RCP4.5 and RCP6.0 are the intermediate pathways whereas RCP8.5 is the highest pathway. These concentration pathways have also been supplemented for model runs which can extend to 2500CE, known as the Extended Climate Pathways(ECPs). For the lowest scenario, ECP2.6, constant concentrations are assumed from 2100CE onward. ECP4.5 and ECP6.0 also assume constant concentrations but from 2150CE onward. Finally, ECP8.5 assumes constant emissions from 2100CE onward and constant concentrations from 2250CE onward. The reader is directed to Figure 1.8 to see the RCP & ECP scenarios.

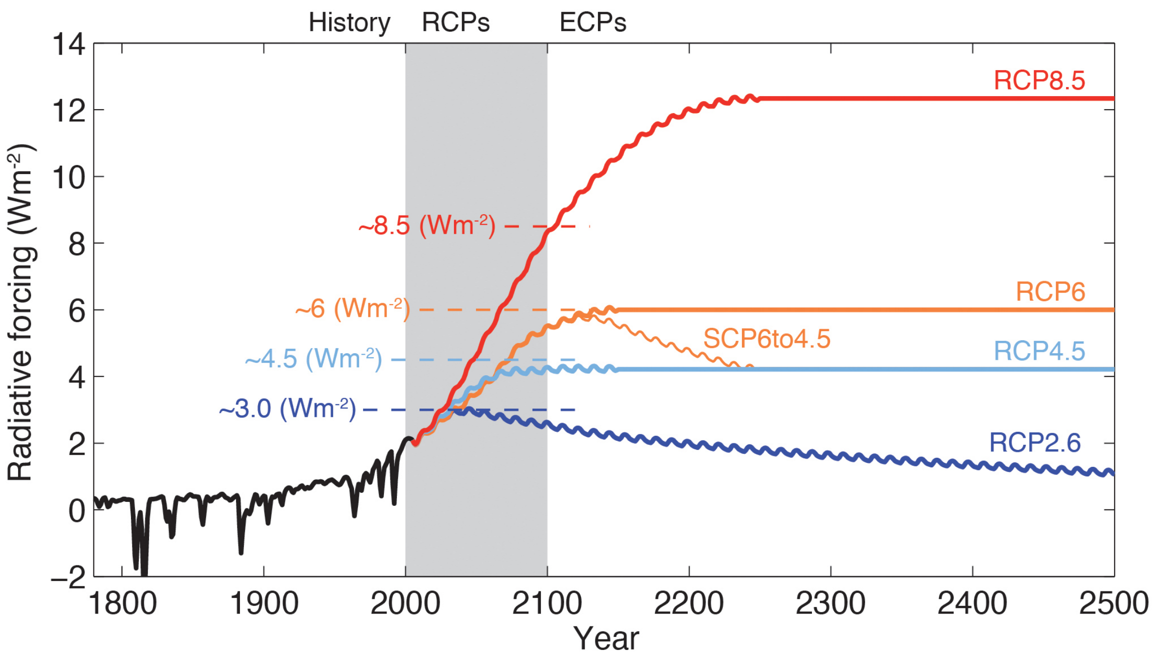

Figure 1.8: The radiative forcing for each of the RCPs and ECPs, along with the transitional SCP6to4.5 model between ECP6.0 and ECP4.5 and the historical record of radiative forcing (black line). Figure obtained from Cubasch et al. [2013] as Figure 1 in Box 1.1.

Melting Land Ice

There are several categories to distinguish between various bodies of ice on Earth. Ice sheets are the largest, with the Antarctic ice sheets(East and West) and the Greenland ice sheet being the only remaining ice sheets on Earth at present. Ice sheets are large bodies of ice with respect to both volume and geographical area ($> 50,000$ km^2), with the latter on the scale of a continent, and thick enough such that its shape and behaviour are governed by the ice dynamics of the body as well as changing climate, which in turn is influenced by changes in ice sheets. Ice flows from the domes down to the margins of the ice sheet, where mass is lost through glacier calving events (resulting in icebergs) and surface melt water run-off. Ice sheets may also have attached ice shelves in many areas. These are large slabs of floating ice of the order of 100 m thick that extend out into the oceans for kilometres, as is the case in present day Antarctica. However, since they are floating, their melting will not contribute to global mean sea level (GMSL) change. The spatial extent and thus volume of the Greenland and Antarctic ice sheets is well constrained through geophysical surveying techniques (Bamber et al. [2013],Fretwell et al. [2013]). Also, various remote sensing techniques can be used to estimate current rates of mass loss for the Greenland and Antarctic ice sheets(Shepherd et al. [2012]). One of the more powerful techniques in this regard involves monitoring changes in the Earth's gravitational potential via satellites(Velicogna and Wahr [2005]).

Glaciers are much smaller bodies of ice by comparison to an ice sheet and fall below the $50,000$ km^2 area designation. A glacier which develops upon the peak of a mountain is referred to as an ice cap. The extent of the world's glaciers is much less well known, even more uncertain yet is the volume of ice they represent. To date the most comprehensive and complete inventory of glacier data is the Randolph Glacier Inventory (RGI)(Arendt et al.) which is a community driven effort and comprises of over $170,000$ individual glacier outlines. The RGI comprises of 19 distinct regions into which glacier outlines have been sorted, each of which is displayed in Figure 1.10. To determine volumes of ice contained in the world's glaciers statistical up-scaling studies are done using the small subset of known glacier thicknesses and volumes. From these studies one is able to determine approximate values for volumes and mean thicknesses for a given glacier outline.These studies can also give us constraints on the maximum contribution of these bodies to GMSL(Marzeion et al. [2012]). Each of these sources of melt produce unique spatial distributions of sea level change due to the changes in the Earth's graviational potential as well as vertical land motion and rotational motion of the Earth as discussed in 1.2.1 and Tamisiea et al. [2003]. We determine these changes by solving the sea level equation for a prescribed ice load such as a glacier complex. We utilize future changes in land ice over the next century as input to the sea level equation. We typically normalize these results by the global mean change in sea level, known as the eustatic change. These normalized results allow us to produce regional changes in sea level by multiplying the eustatic sea level change [6] by the normalized value at a given location. An example fingerprint can be seen in Figure 1.9 where we can see that in the near field, those locations close to the periphery of the body of ice, that there is a local drop in sea level. While in the far field, those locations quite distant from the body of ice we find that we have above average sea level rise. For this particular glacier complex we find that there is a distinct North-South gradient such that those locations further north will experience a below average increase in sea level and in some locations an actual decrease in sea level.

Changes in Ocean Properties

Various mechanisms in the world's oceans can cause regional to local scale changes in sea level. The primary contributor that is considered in this report and in the work of the IPCC's latest assessment report is thermal expansion of the oceans. In a warming climate much of the increase of energy in the Earth system is taken up by the upper most layers of the worlds oceans. While the effect of thermal expansion due to an increase in temperatures of only a fraction of a degree centigrade is quite small - with a coefficient of 207×10^{-6} K^{-1} - this effect is important given the immense volume of the world's oceans. In general, the contribution of this effect to GMSL change is estimated to be $\frac{1}{3}$ to $\frac{1}{2}$ of the

[6] which can come from a different source so long as the ice load is comparable in geometry and magnitude

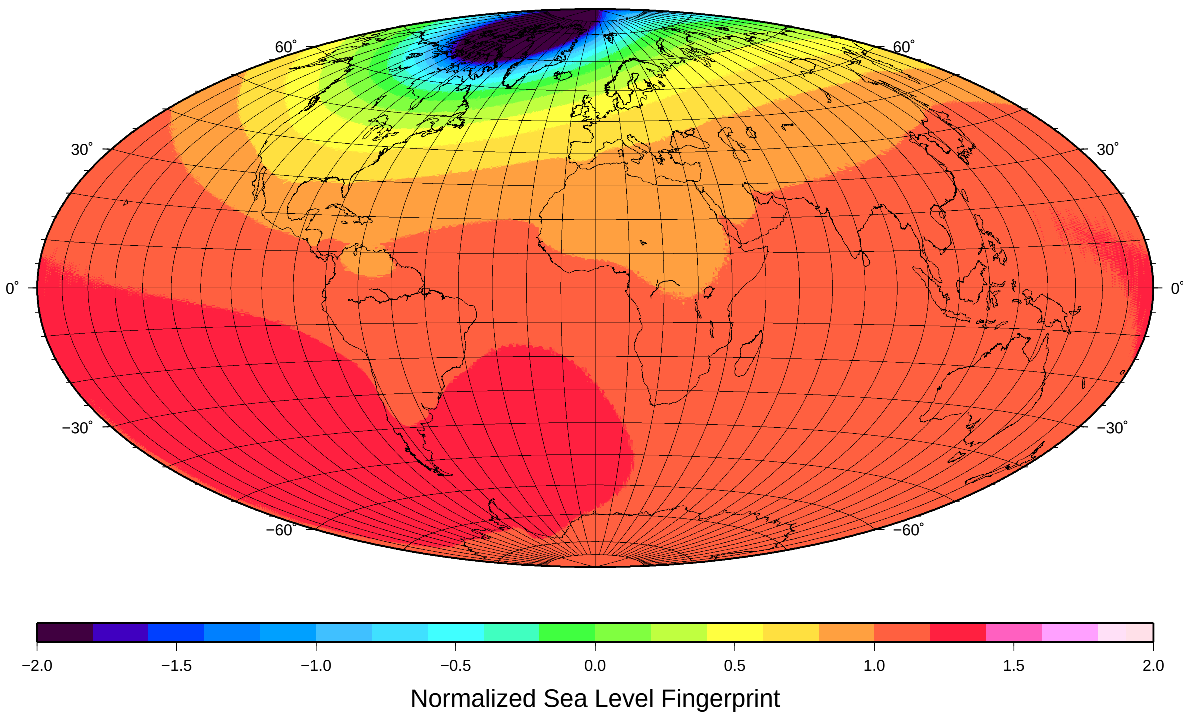

Figure 1.9: A normalized sea level fingerprint for the melting of the Canadian Arctic Glaciers.

total over the next century(Church et al. [2013]). This effect is sensitive to the thermal forcing of the planet as well as various other factors which affect the heat uptake by the oceans vs the heat uptake of other bodies in the climate system. As such we are required to utilize a model of the climate system to estimate the magnitude and spatial pattern of sea level change associated with this effect. It is of note however that recent work by **?** has shown that over long time scales, there is a clear correlation between global mean temps and GMSL therefore, if temperatures continue to rise so will sea levels. However, it is important to note that the sea level rise will not be uniform and there is a time lag in the response, hence the need for models for regional projections over century (as opposed to millennial) timescales.

Atmosphere Ocean General Circulation Model (AOGCM)s are used to simulate changes in the ocean and atmosphere for a specified climate forcing. These are large scale parallel computational models of the atmosphere coupled to an equally complex model of the oceans. As of the writing of this document, models of this level of complexity are typically run at a spatial resolution of $\approx (1^\circ \times 1^\circ)$ with the order of 10 layers in both the atmosphere and the oceans. These AOGCMs are computationally intensive and a single century run on computer clusters can take months to complete. Due to the large resource requirements of these models many research groups which utilize and develop them choose to participate in Coupled Model Intercomparison Project Phase 5 (CMIP5) to make their output readily available and retrievable from a centralized location[7](ICPO [2011]). In order to determine the contribution to sea level change due to thermal expansion, CMIP5 output is used in this thesis work. Other effects such as changes in ocean circulation and salinity, which can also contribute to regional

[7] http://cmip-pcmdi.llnl.gov/cmip5/

changes in sea level, are simulated by AOGCMs and thus implicit in their output.

1.3 Research Aims and Thesis Structure

This body of work provides a first look at the regional scale departures of sea level from the global mean for the east coast of North America. The primary aim of this thesis is to provide a more accurate regional scale projection for future changes in sea level due to the processes outlined above: GIA, ice melting, and changes in ocean properties. Similar studies have been conducted for Fennoscandia by Slangen et al. [2012] and to a more limited extent, for various regions by Church et al. [2013]. As discussed in Section 1.1 the East Coast is a region that is not only densely populated but is also has a great deal of infrastructure and economic value tied to it and so the motivation for such a regional study is clear. Making regional scale sea level projections involves collating data from numerous sources along with the requisite analysis and post-processing of the source data, all of which provides unique challenges and obstacles to overcome.

The primary contribution of this thesis is an improved analysis of the GIA response of the region (Chapter 2). The study region is subject to complications that arise from not only the location relative to the North American Ice Sheet (NAIS), and uncertainties in its past history, but from the influence of lateral Earth structure. In Chapter 2, an extensive modelling study is performed that considers these implications. One of the primary benefits of the GIA aspect of this study is that, while there will always be large uncertainty in the amplitude and climactic impact of continued anthropogenic emissions, the GIA response of this region will be unaffected and so the results presented in Chapter 2 will remain relevant well into the future.

The aim of the work presented in Chapter 3 is the generation of regional scale changes from global scale changes in the climate. These contributions, from land ice melting and changes in the ocean, must be added to the GIA contribution to obtain the total RSL projection for a given location. One of the primary goals of this chapter with regards to changes in land ice volume, is the generation of sea level fingerprints - the unique pattern of sea level change for a given source geometry - for the various bodies of land ice considered. The approach taken to produce the fingerprints for Greenland and Antarctica is described in Section 3.3 whereas the slightly different approach taken for generating the fingerprints of glaciers & ice caps will be outlined in Section 3.4. These fingerprints in combination with information regarding the changes in land ice volumes over the next century allows for the generation of projections regarding the change in sea level due to these sources, which as it will be shown in Sections 3.3 and 3.4, can depart significantly from the global mean for our region of interest. Similarly, through the use of climate model output provided by the research groups that participated in the latest CMIP5, the regional scale changes in sea level due to the thermosteric changes in the ocean are considered in Section 3.2.

Finally, I combine the sea level contributions and discuss the results in Chapter 4. I also discuss further inroads of study for the material discussed in this thesis and possible avenues of improvement for future work of this type.

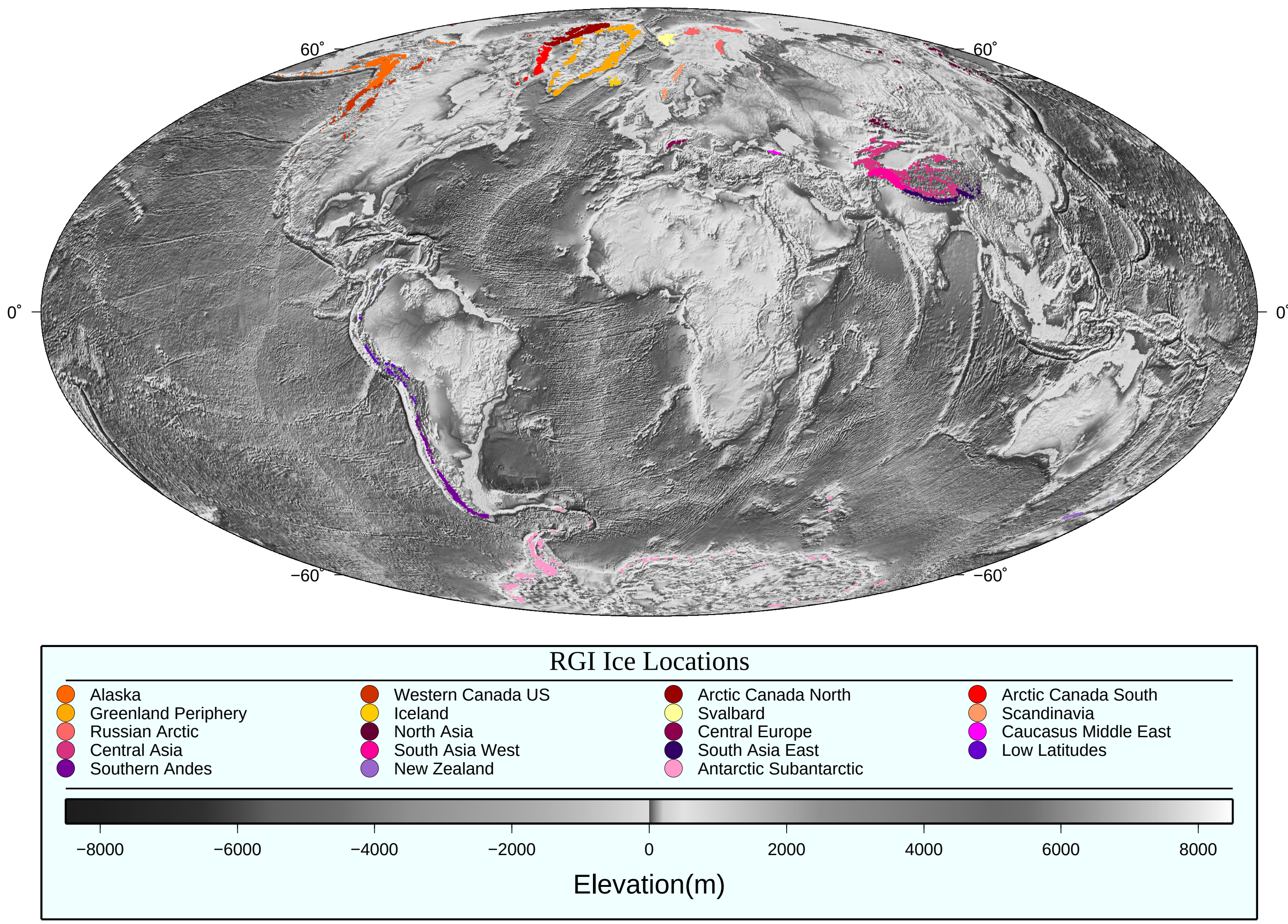

Figure 1.10: The RGI's glacier outlines are sorted into 19 geographic regions. Each one in this figure is outlined in a unique colour. Due to the difficulty in distinguishing the outlying glaciers from their parent ice sheets, the periphery glaciers for Antarctica are commonly included in projections of the Antarctic ice sheets and not evaluated as part of the world's glacier network.

Chapter 2

Estimation of the Contribution of Glacial Isostatic Adjustment to Future Sea Level Changes

2.1 Introduction

Glacial isostatic adjustment (GIA) presents an interesting facet to the modern picture of climate change and contemporary changes in sea level. Since GIA exhibits such a long time scale response, it links changes in the climate system's distant past to changes in the present day and the future. While we are able to determine information regarding past changes in the geographic distribution of ice, we are still presented with many unknowns with regard to this GIA model input. Similarly, despite advances in data quality, quantity and modelling methods, there remain many uncertainties with respect to defining the structure of the Earth's interior. Both are necessary components to determine the GIA response at present and into the future. We evaluate uncertainty in these GIA model inputs by examining a large range of possible model parameters such as the ice history and Earth viscosity structure (lateral variation and depth variation). Using models of GIA as described in Mitrovica and Milne [2003], Kendall et al. [2005] and Latychev et al. [2005] we seek to determine a set of model parameters such that we can accurately reproduce RSL changes evident in the Holocene database of Engelhart and Horton [2012]. Our primary goal is to use these parameters and the resulting model output to produce predictions of the GIA induced changes in sea level for the east coast of North America from the present to the close of the next century and beyond. These predictions will be used in conjunction with projections of sea level changes due to other processes such as thermal expansion and contemporary melting of land ice to produce projections of total sea level change.

2.1.1 Literature Review & Previous Studies

Here we will discuss those results presented in various other publications for the east coast of North America against which we can compare. The first study which we examine is also the most recent, Engelhart et al. [2011] provided the first comparison of GIA model results to data in this region using the dataset later published in Engelhart and Horton [2012]. Using the ICE5G and ICE6G global ice loading histories in conjunction with the VM5a and VM5b viscosity models [1] they achieved reasonable fits in Maine but found that their model results deviated significantly from the sea level data further south. As described below, our results also indicate that it is not possible to fit all of the observations with a single Earth viscosity model.

Given the relative population density and historical and continuing importance of sea based trade for the east coast of North America, there is a fairly extensive network of tide gauges along the length of the coast line with data reaching back as far as the start of the 20th century in some locations. If one examines the rates of sea level change recorded by these tide gauges, the presence of GIA land motion is clearly seen: there is a distinct peak in rates of change at the center of the collapsing peripheral bulge and decreasing rates on either side which fall to a background value. This behaviour is discussed further along with relevant figures in Davis and Mitrovica [1996], who found that the behaviour of the peripheral bulge in their model of GIA is dependant upon the upper and lower mantle viscosity values. Changes in the value for the upper mantle served to change the magnitude of the rate of collapse whereas changes in the value for the lower mantle serve to change the location of the peripheral bulge with respect to the margin of the body of ice. This effect will help explain some of observed trends in our model parameters. Wake et al. [2006] uses tide gauge data along with hydrographic data to determine the steric effect and examine its influence upon their inferences of GIA model parameters. They found that the steric signal dominates the sea level trends estimated for this area and so must be corrected for when using the tide gauge data to infer GIA model parameters. In applying this procedure their results indicate a clear preference for upper mantle viscosity values below $\approx 3 \times 10^{20}$ Pa $\cdot$ s.

2.2 Data

While we are able to generate a multitude of modelled sea level histories by using various combinations of model parameters, we need a method to quantify which of these models best represents the actual GIA response. A variety of data exists that allows us to compare model output to the actual GIA response, such as tide gauge data and datasets of present day rates of uplift obtained from a global positioning system. However, these geodetic data sets are often contaminated by non-GIA processes and so [2] we utilize instead a dataset of sea level changes for our region of interest which was garnered from sea level proxies and extends to over 10 kabp. The signals recorded in this data are dominated by the GIA process and so allow us to examine how well our model can reproduce past trends in sea level. We apply the premise that, if for a given set of parameters our model can accurately reproduce past changes in sea level, we can then use those same parameters to best estimate future changes in sea level due to GIA.

[1] The VM5a and VM5b viscosity models feature similar structure to that used in this study. They assume a 100km thick lithosphere, of which 60km behaves elastically and the remaining 40km has a viscosity of 10^{21} Pa $\cdot$ s. They also feature upper mantle viscosities of 0.5×10^{21} Pa $\cdot$ s and 0.25×10^{21} Pa $\cdot$ s respectively and they both feature the same multi-layer lower mantle of $\approx 5 \times 10^{21}$ Pa $\cdot$ s, for further detail see the work of Peltier and Drummond [2008].

[2] for more detail on this subject see Wake et al. [2006]

2.2.1 Sea-Level Proxies

A sea level proxy is a physical source of information from which one can determine values of sea level for a given location and time in the past. A singular such point in space and time is a sea level index point (SLIP). This study utilises the sea level database of Engelhart and Horton [2012], whose main body of data is garnered from the use of foraminifera. Foraminifera are a family of microscopic amoeboid protists which, depending on species, have specific tolerances for the salinity of the environment they dwell in, several examples of which may be seen in Figure 2.1. As seen in the few examples of Figure 2.1, each foram species has a distinct structure thus allowing for a straightforward means to determine population sizes for a given time period through the use of microscopy. By examining the present day

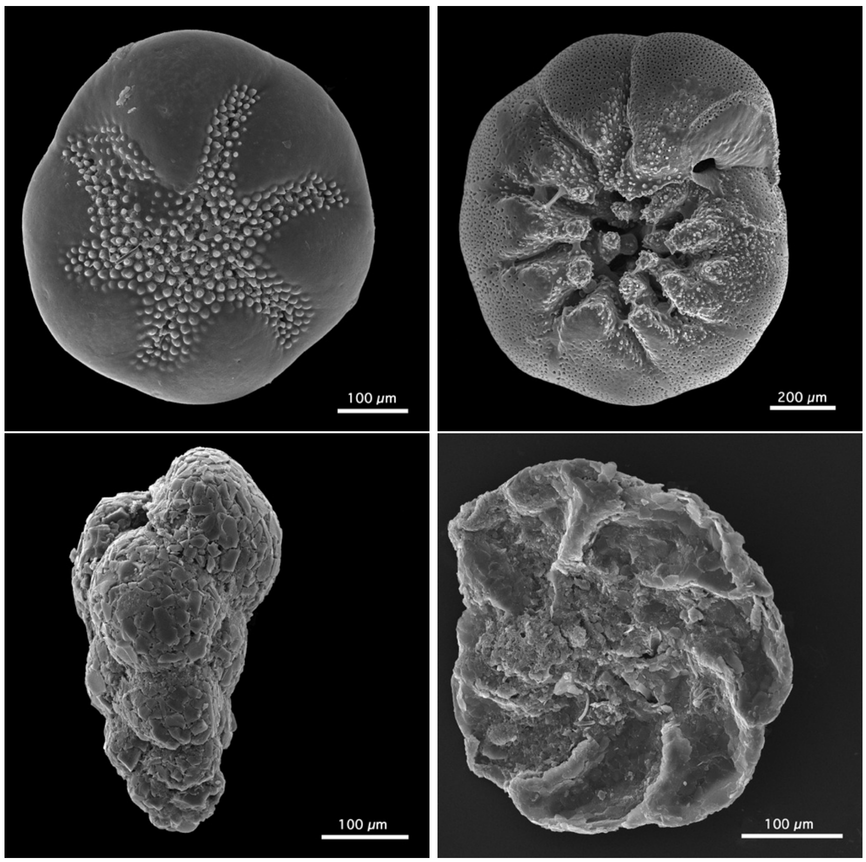

Figure 2.1: Scanning electron microscope images of various species of foraminifera. Clockwise from the upper left the species are Buccella Frigida, Ammonia Beccarii, Trochammina Squamata and Eggerella Advena. The contrasting geometric forms of different species allows for straightforward determination of foraminifera populations in any given sediment sample. Images obtained from the United States Geological Survey(USGS)(Thomas et al. [2000]).

distribution of foraminifera species as a function of altitude relative to mean sea level one is able to construct a sea level transfer function for a given location. In this same location cores are drilled and the distribution of fossilized forams can, in combination with the transfer function, provide information of the value of sea level at some past time that corresponds to a given depth in the sediment core.

Information regarding the age for a given sample is usually obtained by radiocarbon dating of the fossilized remains of the forams. While forams provide a useful array of information they are not a singular source, particularly in the dataset of Engelhart and Horton [2012]. The remains of vegetation which exhibits similar forms of zonation according to salinity can be used as well. Finally, fossilized remains of species that live in intertidal zones (such as mussels) can provide limiting values of sea level, that is, a height at which local sea level must have been above (marine limiting) or below (terrestrial limiting) location and time. Note that in the use of this data we assume that steric changes for our region of interest and the available time over which we have data are negligible, while a standard assumption used in GIA modelling this has not been rigorously tested. The dataset provided by Engelhart and Horton [2012] provides data for 18 distinct regions and three types of data. Much of the data provided by Engelhart and Horton [2012] have unique values for latitude and longitude. To facilitate plotting them in a clear manner in order to compare to model output we chose to sort them into 18 different sites, see Figure 2.3 for the database as sorted into the various sites. Each of these sites along with locations of the SLIPs are shown in Figure 2.2. Examining Figure 2.3 we can see that there is a distinct trend in the RSL data. Typically, a near monotonic rise is observed during the majority of the record, as observed in the New Jersey and Delaware RSL records. The differences in rates occur due to the differing locations of the sites relative to the peripheral bulge, with those sites which lie on the peak of the peripheral bulge showing a greater rate of RSL change while those located further from the peak showing a lower rate. Given that the eustatic change in sea level due to melt water addition has been only a few meters since 7 kabp (and zero within data uncertainty within the last few thousand years), we see that GIA is a major contributor to increasing sea level for this region.

2.3 Model and Methods

2.3.1 1D Model

The 1D model of GIA & sea level we utilize is as detailed in Mitrovica and Milne [2003], Kendall et al. [2005]. We use a pseudospectral technique to determine the changes in sea level for a given ice history and Earth model; this method is computationally efficient with respect to time, which allows us to explore the parameter space quite well. Typically the model we utilize is truncated at harmonic degree 256, however for some elements of this study (Chapter 3) we were required to increase the harmonic resolution to degree 2048. The structure of the Earth is assumed to be spherically symmetric, that is, parameters in the Earth vary only as a function of depth and, with the exception of viscosity, are defined by the Preliminary Reference Earth Model of Dziewonski and Anderson [1981]. Contrary to the spherically symmetric nature of the interior of the Earth model, features on the surface of the Earth such as initial sea level, topography and the loading history may be prescribed anywhere on the surface of the Earth, that is, these parameters are allowed to vary as a function of latitude, longitude and in the appropriate cases, time.

We vary the Earth parameters as follows: ourupper mantle viscosity (UMV) varies from 0.05×10^{21} Pa$\cdot$ s to 5×10^{21} Pa$\cdot$ s; lower mantle viscosity (LMV) varies from 1×10^{21} Pa$\cdot$ s to 90×10^{21} Pa$\cdot$ s and the thickness of the elastic lithosphere varies from 71 km to 120 km. For this part of the analysis we utilize 36 ice loading histories. These ranges of model parameters leads to a total of 13068 unique

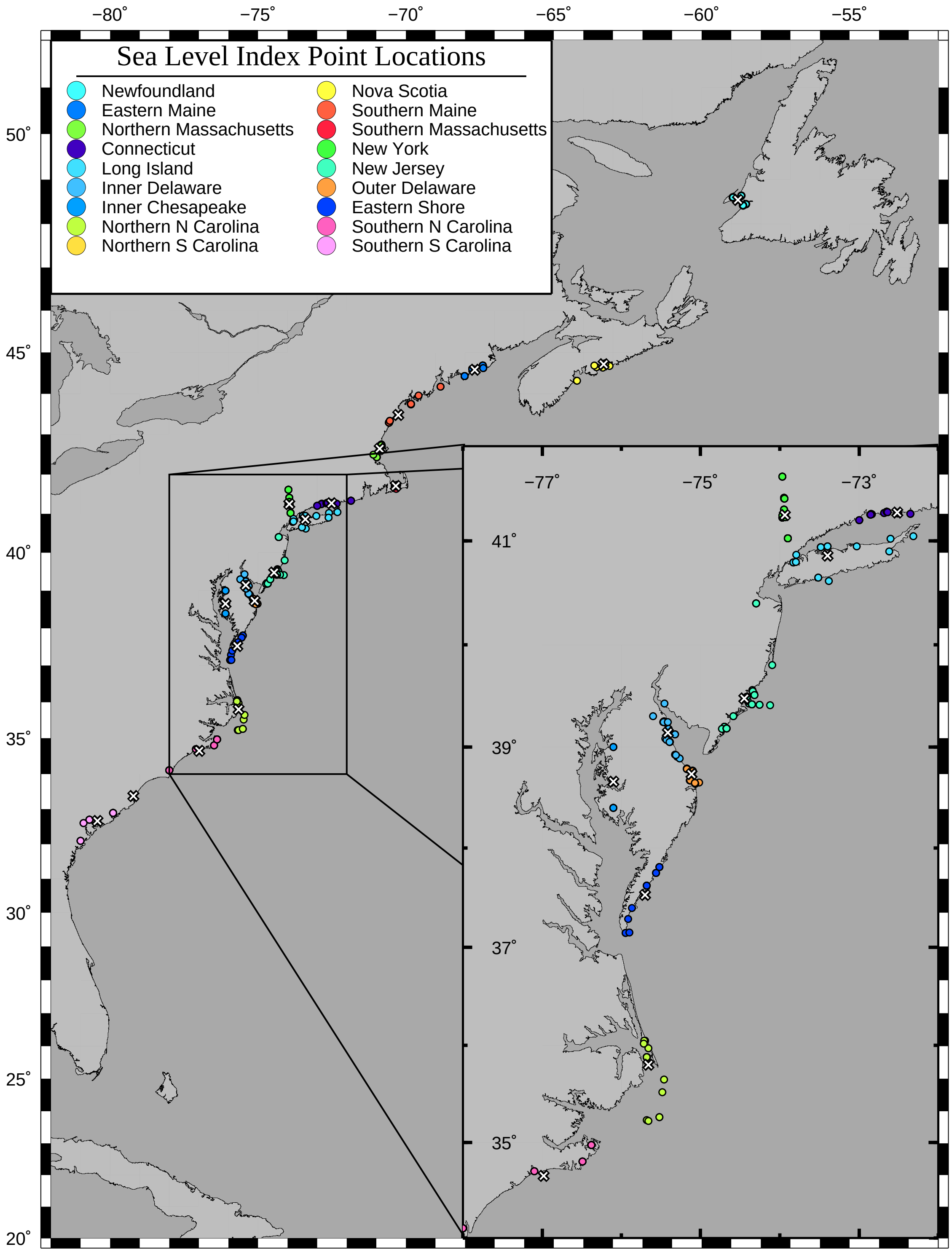

Figure 2.2: Locations of SLIPs in the Holocene sea level database of Engelhart and Horton [2012] marked as coloured circles. The 18 locations used for grouping the data to generate model RSL curves are shown as white 'X's outlined in black. Most sites show a close grouping of SLIPs with many overlapping at the map scale, indeed, with multiple SLIPS as being located at the same geographical point. Given the slowly varying spatial nature of RSL, the relatively minor differences in locations do not result in significant error being incurred when compiling SLIPs into curves at the 18 chosen locations.

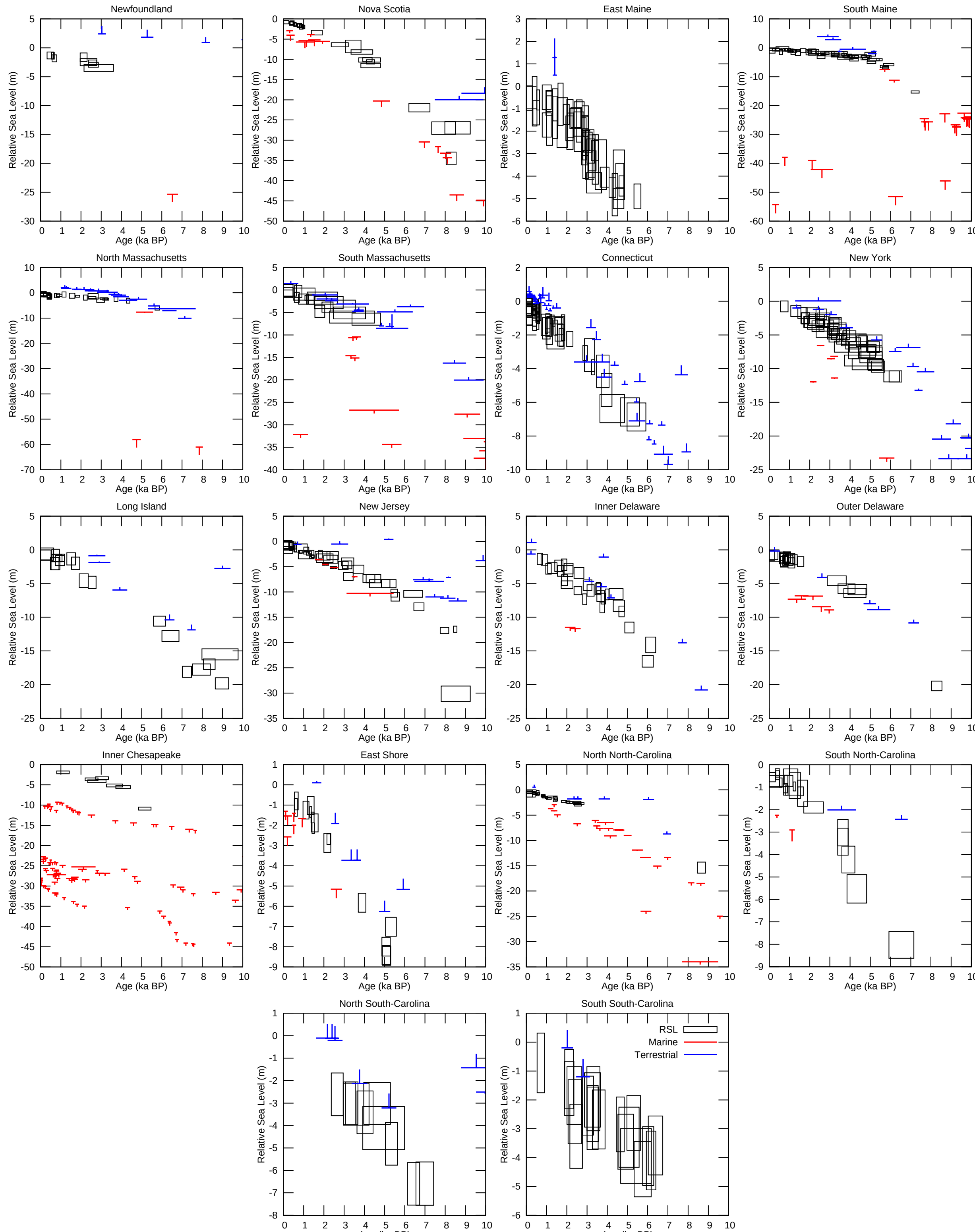

Figure 2.3: The Holocene sea level database of Engelhart and Horton [2012]. We seek to fit this dataset using our model such that we can accurately project the GIA response into the next century for the East Coast. The boxes denote SLIPs and their uncertainty in RSL and time whereas the upright and inverted 'T's are marine (red) and terrestrial (blue) limiting points respectively.

model runs and modelled RSL histories to compare to the real world data. Utilizing the database of Engelhart and Horton [2012] we compare ≈ 6534000 modelled to observed SLIPs.

2.3.2 3D Model

We also utilize the 3D finite volume model of GIA whose description and parameters are described and provided by the authors of Latychev et al. [2005]. The model determines the response of a 3D self-gravitating Maxwell viscoelastic Earth which is elastically compressible. The primary motivation behind the use of this model is to investigate the possible variations in the GIA response that arise due to lateral variations Earth structure - see Figure 1.5 for the magnitude of changes that are present in the region of interest. In order to determine lateral changes in mantle viscosity from a model of seismic wave velocities we utilize the following relationships

$$\delta \ln \rho(r, \theta, \phi) = \left(\frac{\partial \ln \rho}{\partial \ln v_s}(r) \right) \delta \ln v_s(r, \theta, \phi), \tag{2.1}$$

$$\delta T(r, \theta, \phi) = -\frac{1}{\alpha(r)} \delta \ln \rho(r, \theta, \phi), \tag{2.2}$$

$$\nu(r, \theta, \phi) = \nu_0(r) e^{\epsilon \delta T(r, \theta, \phi)}, \tag{2.3}$$

where r, θ, ϕ are the usual spherical co-ordinates, ρ is the material density, v_s is the velocity of shear waves, T is the material temperature, α is the material's coefficient of thermal expansion, ϵ is a control parameter, ν and ν_0 are, respectively, the viscosity we determine and the viscosity of the background model. The control parameter is used such that if a value of 0 is prescribed no lateral viscosity structure is applied and only the 1D background viscosity structure is implemented. When ϵ is non-zero, the 3D viscosity structure is adjusted such that the global average of the viscosity of any given layer matches the prescribed 1D viscosity profile. We obtain $\delta \ln v_s(r, \theta, \phi)$ from the S40RTS model of Ritsema et al. [2011] and we utilize the same layered structure that is used in the 1D spherically symmetric model for our background viscosity model. We chose to use the same depth layering such that their differences are only due to the lateral structure. Therefore, the difference in model output directly reflects the influence of lateral structure. For full details regarding the finite volume implementation of the related GIA response theory see Latychev et al. [2005].

To examine the influence of lateral Earth structure we utilize a control case where the 3D model has the same internal Earth structure and ice loading history as one of the best-fitting 1D models. Changes in RSL due to the lateral structure applied will be with reference to this 1D case. The computational run time of this particular model is significantly longer than the 1D model. A single model run using > 100 processors in parallel takes ≈ 6 days and so the parameter space we can explore in a reasonable timespan is much smaller. This fact, compounded with the significant uncertainty in defining lateral structure makes any conclusions on the impact and significance of lateral structure somewhat tentative. As such, we utilize the results of the 1D analysis to help determine the range of model parameters to investigate.

For our suite of 3D model runs we utilize the 9894 ice model of Tarasov et al. [2012] for the North

American Ice Sheet (NAIS) complex with the rest of the global ice history from Peltier [2004]. We also use the best scoring Earth structure with this ice model, a model with a 71 km lithosphere, 3×10^{21} Pa$\cdot$ s and 30×10^{21} Pa$\cdot$ s UMV and LMV values, respectively. We explored a few scenarios with this set of parameters such as utilizing the S40RTS perturbation globally or regionally by employing the S40RTS perturbation inside a cylinder with a 30° aperture and a larger cylinder with an aperture of 60°, where for both the cylinder of perturbation is centered about our region of interest[3]. We also investigated the effects of perturbing only the upper and lower mantle regions individually with the global S40RTS model. As mentioned previously, the depth averages of the parameters inside the region of perturbation are equal to those in our 1D model. Finally, we chose one of our best fitted sites near the center of our region of interest and perturbed the model using S40RTS at each layer as in the global model, then adjusting it such that our chosen reference site will match our 1D background model[4].

2.4 Results

To determine which of the model's set of input parameters produces the best match to observations, we quantify the model-observation misfit for RSL as follows

$$\delta = \frac{1}{n}\sum_{i=1}^{n}\left(\frac{S_i^{obs}(\theta,\phi,t) - S_i^{mod}(\theta,\phi,t)}{\sigma_i}\right)^2 \tag{2.4}$$

where n is the total number of SLIPs, θ is the latitude, ϕ is the longitude, t is the time, S^{obs} is the observed RSL value, S^{mod} is the modelled RSL volume, σ_i is the uncertainty of the RSL value and δ is the mean model-observation weighted misfit. As such, using δ, should any given model run exactly reproduce our history of sea level it would have $\delta \leq 1$, while models deviating away would have ever increasing values of δ. Note that, to compute δ, model output is computed at each SLIP location rather than at the 18 localities adopted to make a more qualitative visual comparison of model output and data such as in Figure 2.4. As well, while marine and terrestrial limiting data are shown in various figures throughout we do not use them in quantifying model misfits.

In general we utilize the entirety of the available SLIP dataset to determine the value of δ for a given model run. However, over the course of this investigation it became useful to split the datasets into each individual region and then into two groups, northern sites and southern sites (with the boundary being the 44th parallel of latitude). For the remainder of this chapter, unless otherwise noted, the term northern sites will refer to the Nova Scotia and Newfoundland locations while the southern sites will refer to all other sites.

2.4.1 1D Model

Examining the results in Figure 2.4 we are able to make several observations regarding trends in how δ varies as a function of the input parameters varied in this analysis. In frames A-C the optimum region of Earth model viscosity space (low δ values) is defined by relatively high[5] upper and lower

[3]outside of which no perturbation from the background 1D profile was applied
[4]We refer to this as the 'shifted' model
[5]With respect to the ranges of mantle viscosity we examined.

mantle viscosities. There exists a secondary region of intermediate-low viscosity values in which the model fits are also relatively good. Examining frames A through C in Figure 2.4 we see that there is minimal impact on the lowest δ regions when varying the thickness of the lithosphere and in general we find that the results are fairly insensitive to the thickness of the elastic lithosphere. Typically, if a combination of UMV, LMV and ice loading history has a low value for δ, model runs with the same parameters but different elastic lithosphere thickness have similarly low values for δ. In most cases models with a thinner lithosphere score better, albeit only marginally so. For the southern sites, the values for UMV and LMV which result in the lowest δ were among the highest in our range of possible values. Our best scoring parameters for the southern sites were 71 km thickness lithosphere, 3×10^{21} Pa$\cdot$ s UMV, and 30×10^{21} Pa$\cdot$ s whereas for the northern sites we find that 2×10^{21} Pa$\cdot$ s UMV and 10×10^{21} Pa$\cdot$ s are the preferred values. Note that in Figure 2.5 and Table 2.1 we use the best scoring 1% of model runs rather than a 95% or 99% confidence interval. This was done as given the contraints of our model we cannot construct a formal uncertainty or confidence interval for our results and simply chose the best scoring %1 as a cut-off for the discussion of the results.

Figure 2.4, frames D and E are somewhat more difficult to interpret. The purpose of these plots is to examine the influence of upper and lower mantle viscosity on δ between differing ice loading histories. Frame D demonstrates that our preferred UMV values are somewhat invariant of our choice of ice loading history since our regions of lowest δ upper mantle viscosity do not change significantly between ice loading histories. Conversely, examining frame E we find that our LMV regions of lowest δ, while trending more towards the higher end of of LMV values, shows a less coherent pattern than that in frame D. However, this is at least partly due to the fact that almost the entire range of LMV values produced good fits to the data compared to only two sub-ranges (approximately $0.15 - 0.3 \times 10^{21}$ Pa$\cdot$ s and $2 - 3 \times 10^{21}$ Pa$\cdot$ s) for the range of UMV considered.

For sites closest to the margins of the former NAIS, the Earth structure is secondary to the ice loading history with regards to influence on the score of a given model run. In general we find that using the ice loading histories of Tarasov et al. [2012] as input to our model we are able to reproduce the trends of the sea level data far more effectively than when using the ICE5G loading history of Peltier [2004] and resultantly lower δ. In particular, the 9894 ice loading history [6] in conjunction with the adopted global model most accurately reproduces the trends present in paleo sea level data in our region of interest. However, for the northern sites we find that different parameters are preferred by the paleo sea level data. The model runs using the ice loading history history 1259 [7] of Tarasov et al. [2012] result in low δ values across a large variety of Earth structures for the northern sites and the Eastern Maine site, with 17 of the 20 lowest δ models runs. Results for the southern sites in the database reveal that the 9894 ice loading history typically gives the lowest δ values overall, but several other ice loading histories also perform well. For the southern sites we find that the top 1% model runs have an upper mantle viscosity of 3×10^{21} Pa$\cdot$ s. Similarly, model runs with lower mantle viscosity values of 20×10^{21} Pa$\cdot$ s $- 50 \times 10^{21}$ Pa$\cdot$ s make up the vast majority of the best fitting 1%.

By plotting the model output sea level curves alongside the real world data in Figure 2.5, we can examine the performance of a given set of model parameters qualitatively. We can see that by using the lowest δ model for the southern dataset, the sea level data at the majority of the sites

[6] number 34 in Figure 2.4

[7] number 5 in Figure 2.4

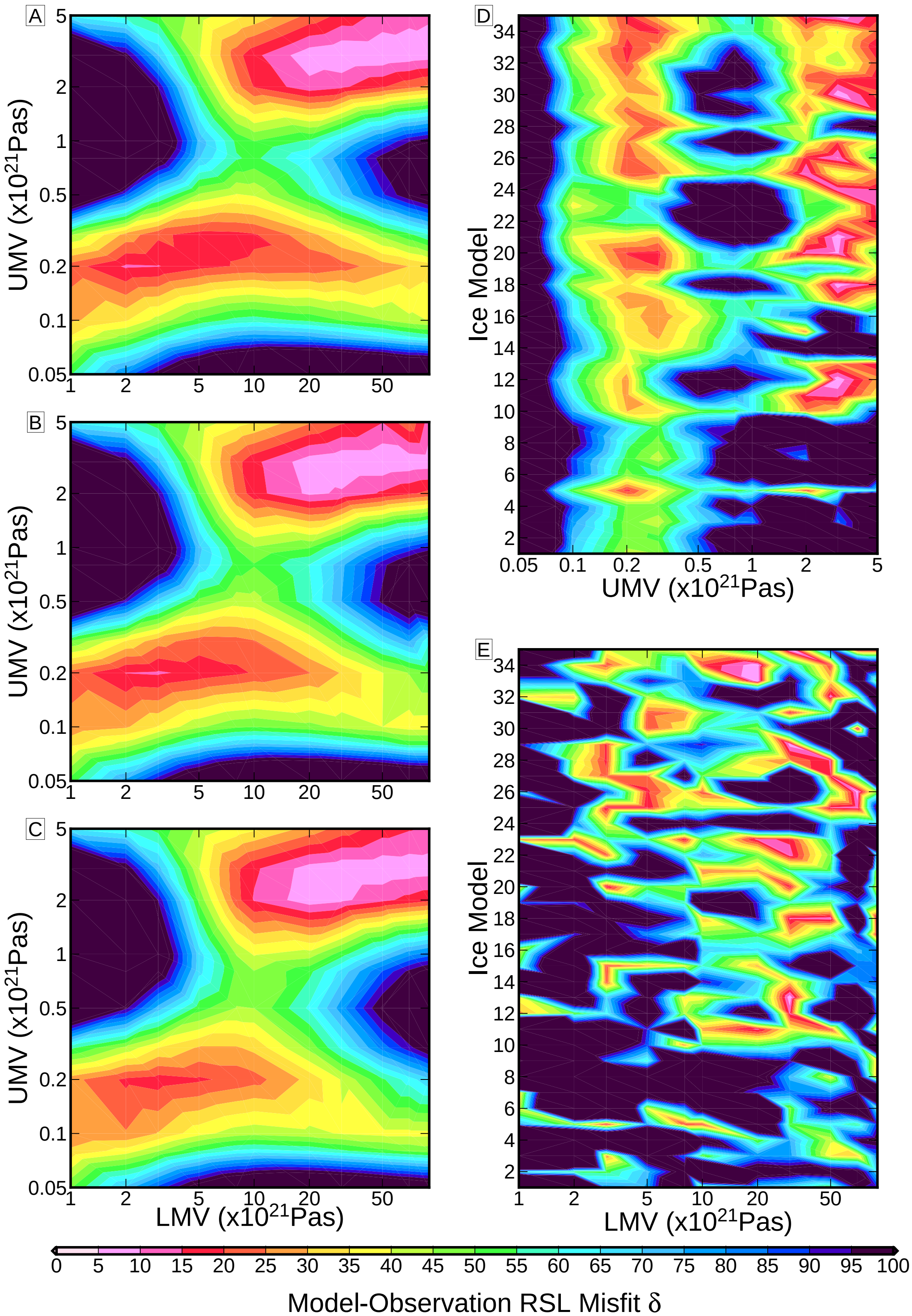

Figure 2.4: δ values as a function of various model parameters. Frames A through C show δ as a function of upper and lower mantle viscosity, respectively, for 71 km, 96 km and 120 km thick elastic lithospheres using the 9894 ice loading history of Tarasov et al. [2012]. Frames D and E show δ as a function of ice model and upper and lower mantle viscosity respectively.

are reproduced well. However, as indicated in Figure 2.5, these model parameters fail to accurately reproduce data from Nova Scotia and Newfoundland. On the other hand, the trends in both Nova Scotia and Newfoundland are reasonably well reproduced by the model run with the lowest δ for the northern dataset but this same model run does not reproduce well the RSL curves observed at the southern sites. It is of interest, therefore, to consider if this result can be explained by invoking lateral Earth structure via the use of the more complicated 3D finite volume Earth model as described above.

GIA-Component of Future RSL Changes

Given that we have established our best fitting parameter values (for the 1D Earth model case) we can proceed to address the primary aim of this chapter and provide a best estimate of the GIA-component of future RSL changes for the east coast of North America (Table 2.1).

2100CE	Southern Sites (cm)	Northern Sites (cm)	All Sites (cm)
St. John's, NF	5.0 (4.6±3.5)	4.2 (11.8±5.9)	7.2 (5.4±2.4)
Halifax, NS	12.2(11.5±1.8)	17.3(14.2±4.8)	13.4(12.3±1.5)
Portland, ME	5.1 (6.8±2.3)	4.5 (4.8±4.0)	5.5 (7.3±2.3)
Boston, MA	10.6(10.6±1.4)	12.8(11.3±4.3)	9.1 (10.9±1.4)
New York, NY	14.4(13.6±1.5)	22.6(16.3±5.6)	12.2(13.7±1.6)
Washington, DC	14.5(13.9±1.4)	22.6(17.7±5.7)	14.4(14.1±1.4)
Virginia Beach, VA	11.7(11.1±1.5)	15.6(17.7±4.7)	12.7(11.3±1.6)
Charleston, SC	7.0 (6.1±2.0)	5.9 (12.6±4.8)	7.6 (6.3±2.0)
2300CE			
St. John's, NF	15.1(13.7±10.6)	12.8(35.5±17.8)	21.8(16.2±7.3)
Halifax, NS	36.4(34.5±5.5)	51.7(42.6±14.5)	40.2(36.9±4.6)
Portland, ME	15.3(20.3±6.8)	13.4(14.6±12.0)	16.7(21.8±6.7)
Boston, MA	31.9(31.7±4.2)	38.4(34.1±13.2)	27.4(32.8±4.2)
New York, NY	43.2(40.7±4.5)	67.7(48.8±16.9)	36.6(41.0±4.7)
Washington, DC	43.5(41.6±4.3)	67.5(53.1±17.0)	43.4(42.1±4.3)
Virginia Beach, VA	35.1(33.1±4.5)	46.5(53.1±14.1)	38.2(33.7±4.7)
Charleston, SC	21.1(18.4±6.1)	17.8(37.8±14.6)	23.0(19.0±6.0)

Table 2.1: RSL projections at 2100CE and 2300CE for various cities along the East Coast of North America using data-preferred Earth and ice model parameters. The best fitting model is shown with the mean of the best scoring 1% of model parameters ± one standard deviation in brackets. The northern region values are the best scoring models when using data from only Newfoundland, Nova Scotia and Eastern Maine whereas the southern region values are those when using the rest of the dataset as well as Eastern Maine.

2.4.2 3D Model

Of the different variants upon the 3D Earth model investigated (Section 2.3.2), we found two distinct categories of response, as shown in Figure 2.6. All of the results, except those produced by the model in which only the lower mantle contained lateral variation, have similar shapes of RSL response, albeit with differing magnitudes. The model in which only the lower mantle was perturbed generally

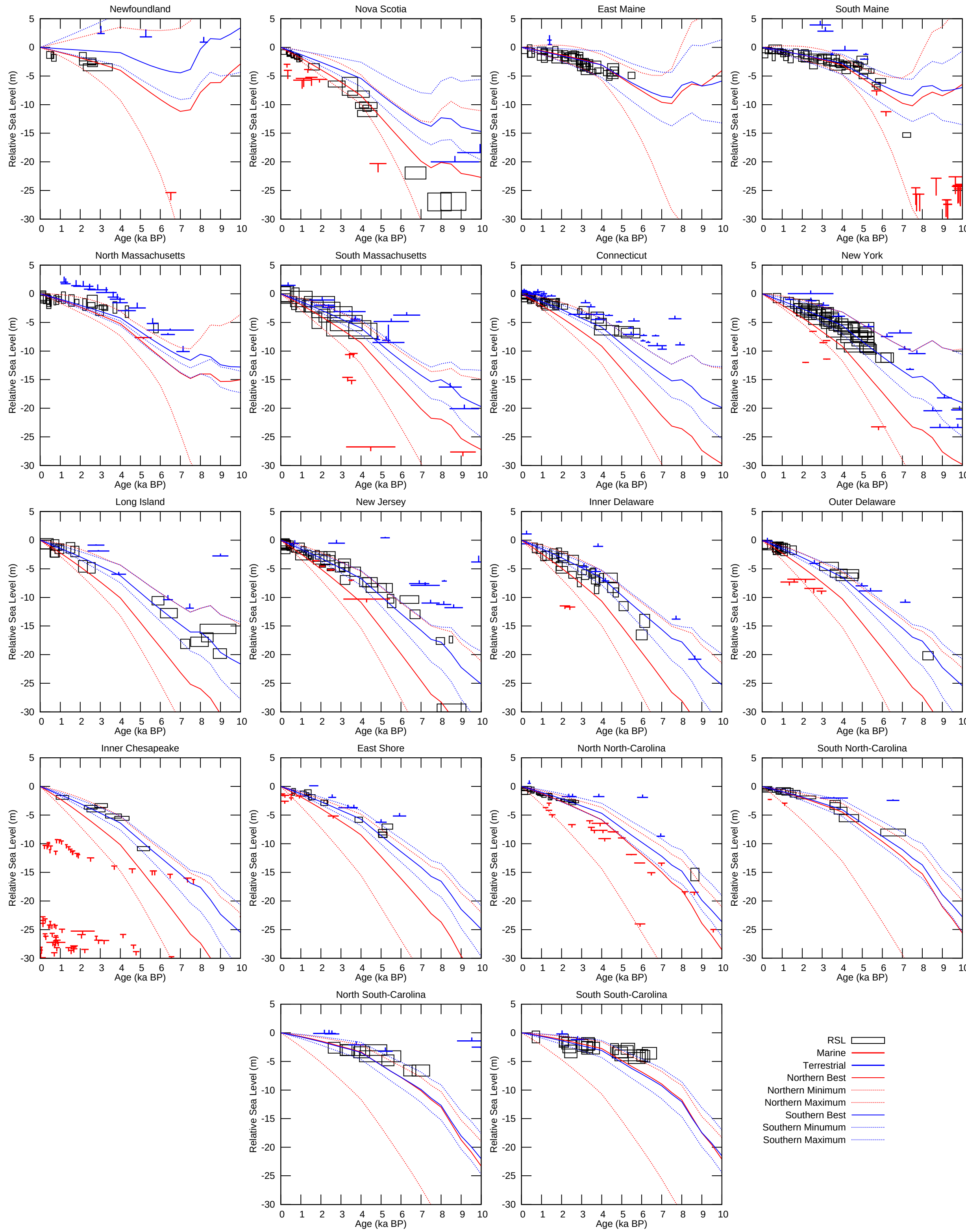

Figure 2.5: The best fitting models for our northern and southern datasets are shown with the maximum and minimum values at each time in the best fitting 1% set of models for both datasets.

produced a near linear deviation through time with respect to the control run for most of the sites investigated (dotted line in 2.6). By comparison, all other RSL curves deviated from the control run in the following manner: steadily decreases from a negative value ($\approx$ 15 m $-$ 20 m at $\approx$ 10 kabp), overshoots 0 m deviation and peaks around $\approx$ 7 kabp. From this peak the deviation approaches 0 m at present day. It is clear from these results that lateral Earth structure plays an important role in this region, with the deviation due to this structure being of similar amplitude to the observed RSL change at some sites.

The magnitude of the peak of the overshoot appears to be the distinguishing feature of the lateral variation models considered. Examination of the results in Figure 2.6 shows that two model runs (upper mantle only and small aperture model) have the peaks of greatest magnitude while the shifted and large aperture runs typically have the smallest peaks. For some locations the latter model runs do not even exceed 0 m deviation. If we examine the influence of these results in the context of our sea level data we find that none of the models allow us to obtain better fits to the data in the northern sites using the preferred Earth structure of the southern sites. That is, the 3D model considered (based on the S40RTS seismic tomography model of Ritsema et al. [2011]) cannot account for the preference of the northern sites for lower viscosity values.

2.5 Discussion

As discussed in Section 2.4, there are two geographical regions which have different model parameter sensitivity. We find that the northern sites (Nova Scotia, Newfoundland and to a lesser extent, Eastern Maine) are most sensitive to the ice loading history while the other sites are most sensitive to the solid Earth model parameters, particularly upper mantle viscosity.

This change in sensitivity from ice model to Earth model moving southwards is not surprising given that some of the northern sites were covered by ice at the LGM and, depending on the ice loading history considered, more recently. As such, it is readily apparent why the northern regions are more sensitive to the ice loading history used.

We also found that the northern sites do not have the same preference for solid Earth parameters as southern sites. This result suggested the influence of lateral variations in Earth properties which motivated the use of a more complex 3D Earth model of GIA. The results of this exercise, based on the seismic tomography model S40RTS of Ritsema et al. [2011], were unable to explain this difference between northern and southern sites. Rather, we found that the model we employed produced the opposite difference in RSL to that required. How this result comes about can be seen in Figure 1.5, where the region under the northern sites shows an increase in seismic velocity and correspondingly a higher viscosity rather than the desired lower viscosity by comparison to the southern sites. However, we only considered one tomography model in combination with one ice loading history and cannot completely rule out lateral structure as an avenue to resolve this issue. The results shown here indicate that lateral structure has a large effect on the modelled RSL curves and so further investigation is certainly warranted.

We compare these preferred values to those given in previously published works such as Engelhart et al. [2011] and Wake et al. [2006]. With respect to the values for UMV and LMV given in Engelhart

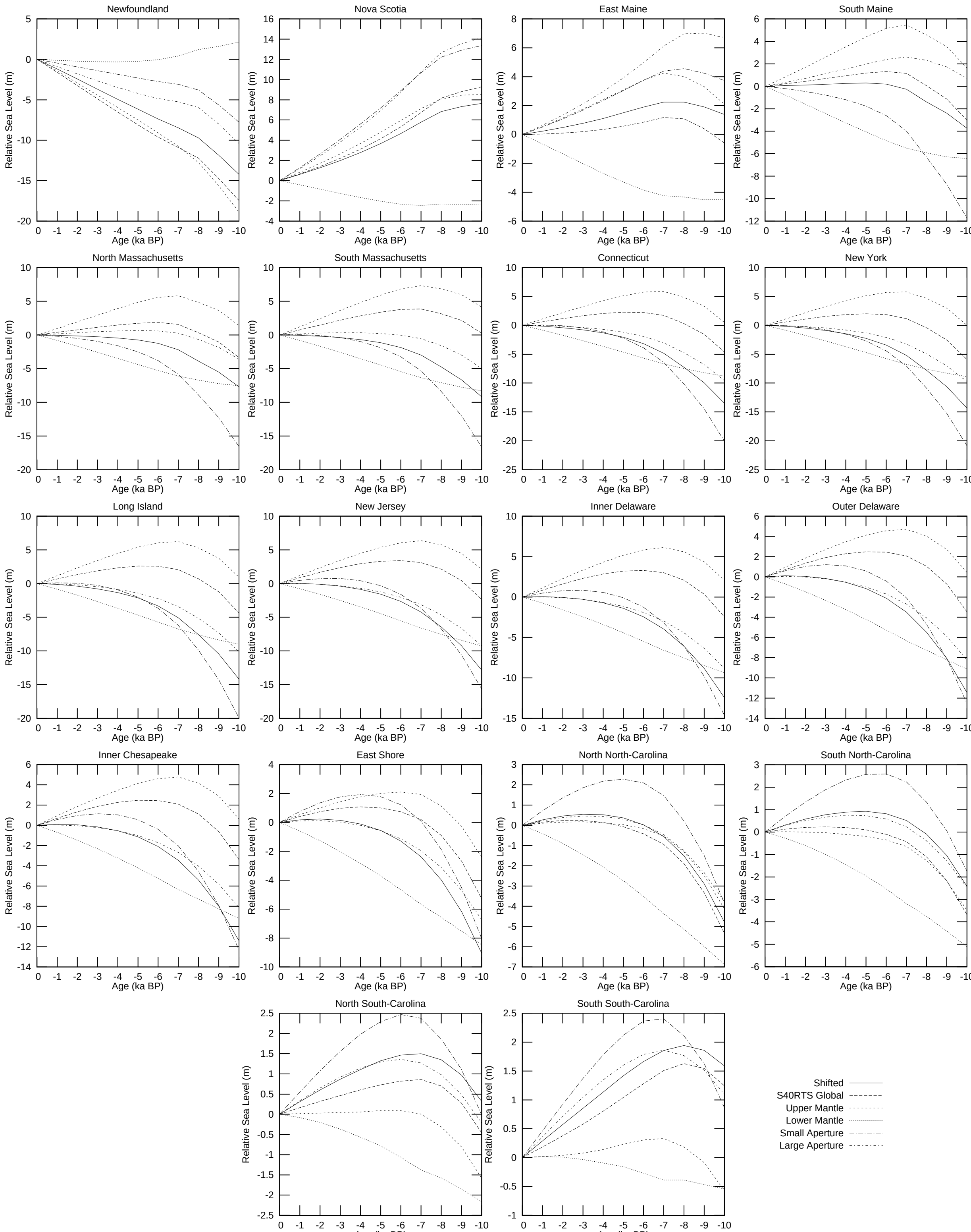

Figure 2.6: Differences in sea level from the 1D control run due to lateral structure using our 3D finite volume model of GIA. We can see that changing the structure in this region generally produces a very similar change in the predicted RSL curve but with differing magnitudes.

et al. [2011] [8] , the values we estimated for these parameters using data from the southern sites are very different, however we also obtain better fits in the southern sites by comparison. The values of UMV and LMV preferred by the northern sites are closer to those given in Engelhart et al. [2011], with 2×10^{21} Pa $\cdot$ s UMV and 10×10^{21} Pa $\cdot$ s LMV being preferred and while our fits are an improvement they are comparable. When we compare our UMV and LMV values to those presented in Wake et al. [2006] we find that we both obtain good fits for similar ranges of LMV, however their optimum values for UMV are much lower than those inferred in this analysis. We postulate that this is due to the issue of a large steric overprint in the tide gauge data, which may not have been accurately removed in their study.

Given the results presented in Davis and Mitrovica [1996] we can understand some of the behaviours and the non-uniqueness present in the results. Primarily, it is apparent why we find a range of LMV values across several differing ice models, as the combination of ice loading history and LMV will determine the location of the peripheral bulge. That is, it is possible that for a given value of LMV we can change the ice loading history and obtain good fits for certain combinations and vice-versa.

Finally, the results in Table 2.1 clearly show that the long time scale process of GIA can be a significant contributor to future changes in sea level along the east coast of North America and so should be considered when estimating the total RSL change for this coastline. At 2100CE we estimate the GIA-contribution of RSL to be in the range of 5 cm to 20 cm and this increases to 15 cm to 60 cm at 2300CE. In comparison to results from the latest IPCC report(Church et al. [2013]), these values are in the range of 1/4 to 1/2 of the total GMSL rise estimated for the most conservative climate change scenario (RCP2.6) and 1/6 to 1/3 of the most extreme scenario (RCP8.5).

2.6 Conclusions

Results for the southern sites in the database reveal that the 9894 ice loading history of Tarasov et al. [2012] typically gives the lowest δ values overall, however several other ice loading histories also perform well. The model runs using the ice loading history history 1259 result in the lowest δ values across a large variety of Earth structures for the northern sites and the Eastern Maine site demonstrating, in part, the strong sensitivity of this region to ice loading history. For the southern sites we find that the top 1% model runs have UMV of 3×10^{21} Pa $\cdot$ s and prefer LMV values in the range of 20×10^{21} Pa $\cdot$ s $-$ 50×10^{21} Pa $\cdot$ s whereas the northern sites prefer 2×10^{21} Pa $\cdot$ s UMV and 10×10^{21} Pa $\cdot$ s LMV. When we compare these values to those presented in similar studies such as Engelhart et al. [2011] and Wake et al. [2006] we find that the data prefers higher values for UMV and LMV than given in previous studies. We determine that the 3D model considered (based on S40RTS (Ritsema et al. [2011]) cannot account for the preference of the northern sites for lower viscosity values by comparison to those values preferred by the southern sites. However, we only considered one tomography model and cannot completely rule out lateral structure as an avenue to resolve this issue. The results shown here indicate that lateral structure has a large effect on the modelled RSL curves and so further investigation is certainly warranted. Finally we obtain one of the primary goals of the

[8] They use values of 0.5×10^{21} Pa $\cdot$ s and 0.25×10^{21} Pa $\cdot$ s for their UMV and utilize a multi-layer lower mantle of $\approx 5 \times 10^{21}$ Pa $\cdot$ s, see Section 2.1.1 for more detail

investigation and find that at 2100CE we estimate the GIA-contribution of RSL to be in the range of 5 cm to 20 cm and this increases to 15 cm to 60 cm at 2300CE.

Chapter 3

Other Contributions to Changes in Sea Level

3.1 Introduction

While the study of the GIA response of the east coast of North America remains one of the primary components of this thesis we can extend the usefulness of such projections and place the results in better context by including projections of changes in sea level from sources other than GIA. While in Chapter 2 we demonstrate that GIA will produce changes up to ≈ 20 cm by 2100CE, that contribution is only a fraction of the total expected sea level change. If we consult the latest IPCC assessment report(Church et al. [2013]), we can see that GIA can be as small as 1/6 of the total GMSL change and as large as 1/2 of GMSL change by the close of the 21st century. Here we discuss the processes introduced in Chapter 1 in more detail. In Section 3.2 we first discuss anthropogenic sea level changes resulting from changes in ocean properties such as temperature and changes in salinity, which influence density and therefore ocean circulation. We investigate contemporary mass changes in the Greenland and Antarctic ice sheets in Section 3.3 and the resultant contributions to changing sea level. Similarly, we elucidate sea level changes due to changes in GICs in Section 3.4. Finally, we examine the resultant sum of each of the processes considered in this chapter to future changes in sea level along the east coast of North America in Section 3.5.

3.2 Changes in Ocean Properties

Oceans cover over 70% of the surface of the Earth with an average depth of ≈ 3700 m, as such it is no great surprise to find that small changes in the properties of the world's oceans can lead to large changes in sea level. A change as small as 1/10 of a degree centigrade can cause an increase of ≈ 8 cm in GMSL. The latest IPCC report demonstrates that changes in sea level due to thermal expansion and changes in density are the largest of the ensemble of effects considered. Furthermore, they comprise of just under 1/2 of the total projected sea level rise. In this study the sea level contribution of thermal expansion, and related density and circulation changes that can affect changes in sea level, are determined via the use of AOGCMs.

AOGCMs are highly computationally intensive and complex, to the extent that a single model is often maintained by a dedicated team of researchers. To facilitate greater end-user applications of model output these modelling groups frequently participate in intercomparison projects. In such projects the inputs to the models are specified such that all models use the same inputs and the groups distribute their results for comparison and benchmarking of their models. We utilize data from such an intercomparison project, namely the Coupled Model Intercomparison Project which is in phase 5 (CMIP5), and obtain model outputs regarding the changes is sea-level of the models. While data from > 30 individual models have been uploaded to the CMIP5 repositories we utilize only those listed in Table 3.1 due to time and data constraints.

We utilize a suite of models rather than rely on any given single model as no single model is as of yet capable of completely simulating the climate system. Each model utilizes different implementations of the same underlying physics and climate science and as such they obtain different results to the same set of forcings. The differing results obtained comes primarily from these different implementations and parametrizations of different processes such as carbon cycle as well as using differing model parameters. Other factors such as differences in model resolution and coupling of the atmosphere to the ocean can be strong influences on the results.

In order to efficiently extract sea level change from the 14 models listed custom software was developed to interface to and process the data. This involved writing several thousand lines of computer code in multiple languages[1] using various application programming interfaces.

3.2.1 Methods

Although the CMIP5 project has outlined numerous standards that model output should adhere to, the results of each group often require post processing to various degrees. The issues most commonly encountered is the use of a non-uniformly spaced and non-regular grid upon which the relevant physics are modelled. To deal with these differences, the end user is required to perform co-ordinate transformations from one grid to another. There is also some degree of post processing required despite the choice of AOGCM to correct for effects such as model drift, an aberration discussed later on. We outline the methodology followed to produce sea level projections from the CMIP5 output below.

The CMIP5 project prescribes two primary data output fields that participating modelling groups need provide, ZOS and ZOSGA, which represent, respectively, sea surface height above geoid and global average sea level. ZOS is a field prescribed for all ocean surfaces on the Earth and is a function of time, that is $ZOS(\theta, \phi, t)$ whereas ZOSGA is only a function of time. As previously mentioned, multiple models utilize non-regular model grids and in order to utilize common software utilities on all ZOS model output we are required to convert the model grids to a more usable form through resampling routines. Once we have the model outputs in a usable format we can begin to make our appropriate corrections, the first being to correct for what has been termed 'model drift'(Katsman et al. [2008]). Model drift refers to a long term progression away from the steady state condition that AOGCMs are vulnerable to. To correct for this, model groups participating in the CMIP5 project are required to submit a model run where there is no forcing on the system and pre-industrial conditions have been

[1] Primarily Fortran, Python and the Bourne Shell

imposed on the system. These model runs, for sea level, typically exhibit a linear trend in changing sea level which is easily removed from the other output. To remove this signal we simply fit the ZOS and ZOSGA output with a linear trend to determine the correction as a function of time. Another such correction that must be made is to correct the ZOS output with respect to its global average. The area weighted global mean of ZOS data output should have been corrected to zero by each modelling group prior to uploading data to the CMIP5 servers. However, not all groups performed this step and so this value is calculated in the procedure applied here to ensure that all output is consistent in this respect. To summarise, in order to make a projection of sea level utilizing the climate data we use:

$$\Delta SL^{R,M}(\theta,\phi,t) = SL^{R,M}_{ZOS}(\theta,\phi,t) - SL^{R,M}_{ZOS}(\theta,\phi,t_0) + SL^{R,M}_{ZOSGA}(t) - SL^{R,M}_{ZOSGA}(t_0) - \Delta SL^{R,M}_{drift}(\theta,\phi,t) \quad (3.1)$$

where θ, ϕ are the usual spherical co-ordinates, t is the time of interest, t_0 is the initial reference time from which the projection is made[2], R denotes the RCP scenario used and M denotes the AOGCM. The last term, which corrects for model drift, is given by

$$\Delta SL^{R,M}_{drift}(\theta,\phi,t) = \left(D^{control,M}_{ZOS}(\theta,\phi,t) + D^{control,M}_{ZOSGA}(t)\right)(t - t_0), \quad (3.2)$$

where D_{ZOS} and D_{ZOSGA} are the rates determined by fitting linear trends to the pre-industrial control run output. However, often the model output is time averaged over several decades to remove higher frequency natural variability in the system, this correction is trivial and only requires one to use a running average function upon the output data.

3.2.2 Results & Discussion

For any given RCP scenario we utilize between $10 - 15$ individual model runs to estimate the sea level contribution due to changes in ocean properties. An example of model output for the site St John's, Newfoundland is shown in Figure 3.1; the time series are averaged over 10 year intervals. Results for other locations in the study are qualitatively similar. The results illustrate that, while models often agree on the general trend and sign of the change in sea level, the magnitude of the change can vary widely depending on the climate scenario. For RCP2.6, we find that most of the models clustered about 10 cm $-$ 20 cm of sea level change by 2100CE with two outliers projecting around 45 cm by the close of the century. Similarly, RCP4.5 has the majority of values clustered about 20 cm $-$ 30 cm with one model projecting as high as ≈ 55 cm, while RCP6.0 includes a similar maximum result and a similar mean but the model spread is considerably larger. Finally, for RCP8.5, the majority of the models project sea level between 30 cm $-$ 50 cm with a sea level high of 70 cm. Of note is that despite the differing magnitudes, almost all of the time series show an increase in sea level over the next century despite the climate scenario. Projections for the same 8 locations highlighted in Chapter 2 are given in Table 3.2. Note that every value is positive and > 14 cm. For comparison, the projected GMSL values from AOGCMs provided in the latest IPCC report, are 14 cm, 19 cm, 19 cm, and 27 cm for, respectively, RCP2.6, RCP4.5, RCP6.0, RCP8.5. The mean values for our study region are greater,

[2]typically this is usually the year 2006

Climate Research Center	Climate Model Name
Beijing Climate Center, China Meteorological Administration	BCC-CSM1-1 BCC-CSM1-1-M
Canadian Centre for Climate Modelling and Analysis	CanESM2
National Center for Atmospheric Research	CCSM4
Centre National de Recherches Météorologiques/ Centre Européen de Recherche et Formation Avancée en Calcul Scientifique	CNRM-CM5
NOAA Geophysical Fluid Dynamics Laboratory	GFDL-ESM2M
NASA Goddard Institute for Space Studies	GISS-E2-R
Met Office Hadley Centre(additional HadGEM2-ES realizations contributed by Instituto Nacional de Pesquisas Espaciais)	HadGEM2-ES
Institute for Numerical Mathematics	INM-CM4
Institut Pierre-Simon Laplace	IPSL-CM5A-LR
Japan Agency for Marine-Earth Science and Technology, Atmosphere and Ocean Research Institute (The University of Tokyo), and National Institute for Environmental Studies	MIROC-ESM MIROC5
Max-Planck-Institut f ur Meteorologie (Max Planck Institute for Meteorology)	MPI-ESM-LR
Meteorological Research Institute	MRI-CGCM3

Table 3.1: Providers and model names for the climate model output used in this work. Not every model listed provides model runs for all RCP scenarios but each provides at least 1 model run to 2100CE. On average each model provides data for ≈ 3 of 4 RCP scenarios.

reflecting spatial variability in the models (plus output from a greater number of models was considered in the IPCC report).

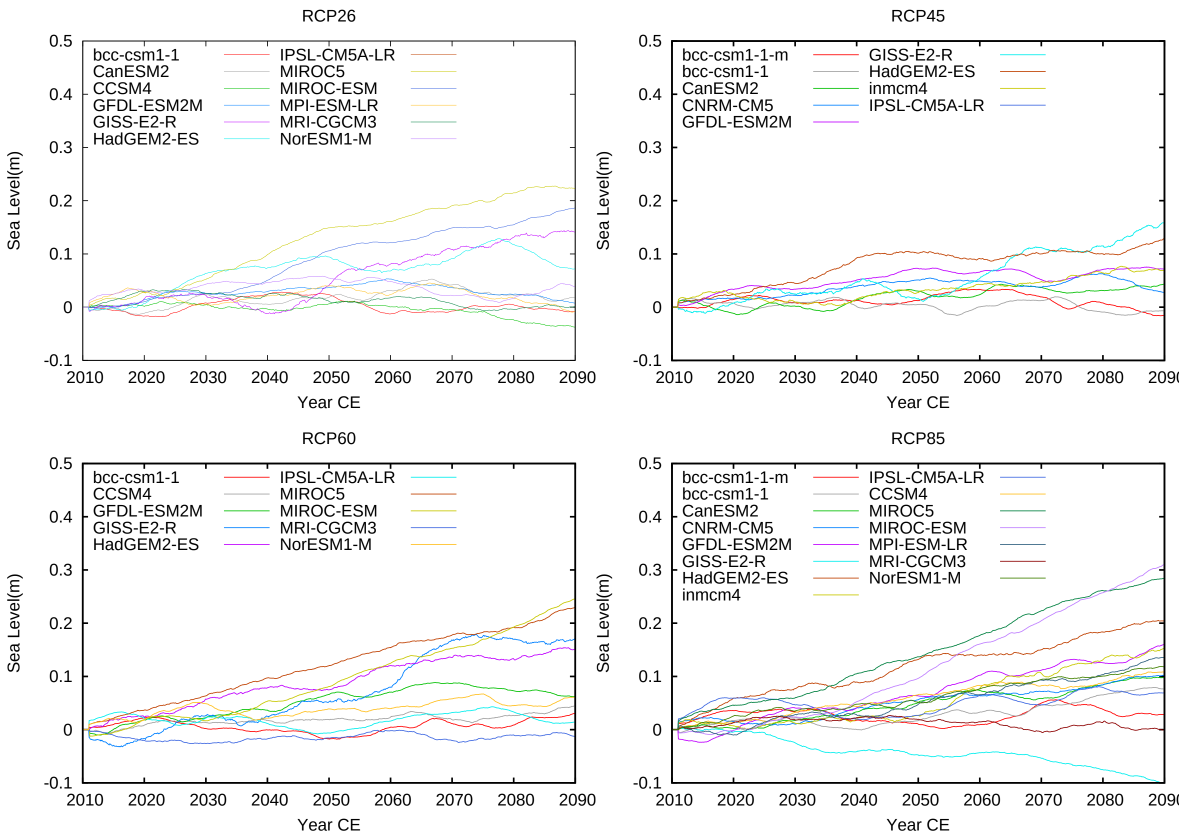

Figure 3.1: Ten year averaged time series for St. John's Newfoundland for all RCP scenarios. While the climate model results typically agree on the overall trend in sea level they often disagree in the magnitude.

2100CE	RCP2.6 (cm)	RCP4.5 (cm)	RCP6.0 (cm)	RCP8.5 (cm)
St. Johns, NF	18.5±13.7	23.5±16.5	26.0±20.2	33.2±22.6
Halifax, NS	18.2±13.6	23.0±16.8	25.3±20.5	33.1±22.4
Portland, ME	17.6±13.4	22.4±16.5	24.5±20.5	30.5±22.6
Boston, MA	17.3±13.4	21.9±16.3	24.1±20.1	32.1±21.9
New York City, NY	15.9±13.4	20.7±16.0	24.2±20.3	29.1±22.1
Washington, DC	15.7±12.6	20.3±14.9	22.3±18.6	25.6±21.9
Virgina Beach, VA	15.3±12.2	19.8±14.5	21.2±17.7	27.0±20.2
Charleston, SC	14.0±10.4	17.4±13.0	18.1±15.3	21.4±18.1

Table 3.2: Local sea level projections from AOGCM output as provided by CMIP5. Ensemble means of model output (differences between the time average of $2085 - 2100$ and $2006 - 2015$) are given $\pm$ 1 standard deviation of the ensemble. While our means are quite close to GMSL provided in the latest IPCC assessment report (Church et al. [2013]) our standard deviation is quite large by comparison to their provided likely range. The larger standard deviation could be due in part with the smaller selection of AOGCMs used in this study vs larger selection used in the latest IPCC report.

3.3 Projected Mass Changes of Ice Sheets

Future changes in the Greenland and Antarctic ice sheets are expected to be a significant contributor to the total sea level change this century. The global average contribution due to mass changes in the Greenland ice sheet is expected to be 4 cm to 21 cm while Antarctica's contribution is expected at -3 cm to 14 cm (Church et al. [2013]). However, due to the physics of sea level change associated with land ice melt (See Chapter 1, there will be significant regional departures from the global average value. To determine the difference from the global average change for any given location we calculate sea level fingerprints (Mitrovica et al. [2001]) which give the global pattern of sea level change for a given ice mass change. Sea-level fingerprints are generated via a model of sea level change where one solves the sea level equation, as discussed in Section 1.2.1, (Farrell and Clark [1976], Mitrovica and Milne [2003]) for a given input ice history over a short time period such that the Earth response is dominantly elastic. As discussed previously in Section 1.2.1. The calculated changes are commonly normalized by the global mean value for sea level, known as the eustatic value.

A small number of studies have estimated future changes in ice extent (Church et al. [2013]) and most of these changes are broadly similar in geometry to changes observed over the past decade or so. Therefore, we use output from the Gravity Recovery and Climate Experiment (GRACE) to define future patterns of mass changes for both ice sheets. Multiple facilities provide gridded GRACE data sets, the three that are used in this study are from the Jet Propulsion Laboratory (JPL), the Deutsches GeoForschungsZentrum (GFZ) and the Center for Space Research (CSR). Given that each facility uses the same raw data then uses various techniques to maximize the amount of noise removed while maintaining the geophysical signals, there are significant variations between provided data sets which represent the same region, period and processes. We adopt all three products and examine the influence these (relatively subtle) differences have upon sea level fingerprints. By using all three solutions we are incorporating these variations into a sensitivity analysis, which also considers the harmonic degree truncation (spatial resolution) of our calculations and the Earth model parameters used. We examine each of these aspects and their impacts on the final fingerprints in Section 3.3.3.

3.3.1 Gravity Recovery and Climate Experiment (GRACE)

GRACE monitors and reports on changes in the Earth's gravitational potential due to a variety of Earth processes. Once the raw output has been processed to remove signals due to changes in the ocean and atmosphere, the remainder is mostly attributed to changes in land water storage such as local hydrology or mass fluctuations in the crysophere. Monthly GRACE data are provided as a spherical harmonic expansion. The magnitudes of the error in the GRACE experiment data increase as a function of spherical harmonic degree (Landerer and Swenson [2012]). In addition there are systematic errors associated with particular degrees, the most commonly seen of these is striping from north to south. Once the output has been processed to reduce error in the output it is necessary to restore some of the signal that has been removed due to the filtering processes.

The filters, as used in the gridded data sets and presented in Landerer and Swenson [2012] consist of two parts. One is designed to remove errors in the GRACE data that are evident as striping from N-S, this signal is attributed to correlations between various spherical harmonic coefficients. The second is a Gaussian average whose half width is 300 km (Landerer and Swenson [2012]). The second filter acts to remove errors in the higher degree coefficients which have not been removed by the de-striping. Unfortunately the Gaussian filter is a trade off between signal-to-noise and spatial resolution as features smaller than the half width can no longer be resolved. This smoothing in the space domain is often performed twofold as GRACE data are typically truncated in a manner similar to a low pass filter by exclusion of harmonic degrees greater than 60, thus features smaller than $\approx$ 330 km will not be resolved either. To restore the strength to the real signals, data points are multiplied by an appropriate gain factor. These gain factors are determined by examining the effect the filters have on simulated data.

3.3.2 Methods

In order to obtain sea level fingerprints it was first necessary to convert the gridded GRACE data sets into a usable input format for our model of sea level. In order to do so, each point in the provided data sets was fitted with a linear function through the entire time series of provided GRACE data, approximately 2006CE to 2014CE. The rate of change for each point was then used as the input to the sea level code to generate sea level fingerprints. Since the resultant sea level predictions are normalized by the eustatic sea level value, they can be easily scaled to produce projections for a specified range of melt amplitudes. We chose the ranges determined in the recent IPCC report given above. This procedure is accurate as long as the geometry of melt does not deviate significantly from those used to generate the fingerprints. The ice sheet changes produced from each data center's gridded output is presented in Figure 3.2. These changes have been scaled such that their resultant rate of eustatic sea level rise is 1 mm/a on average, which is consistent with similar studies such as Mitrovica et al. [2011].

3.3.3 Results & Discussion

Influence of GRACE Data Processing

Examining Figure 3.2 it can be seen that for Greenland (A-E), while the results from each data center are broadly similar, there are some differences. The output from the CSR data center shows the greatest deviation from the mean. The CSR output has the greatest mass flux located at the southern most point of Greenland whereas the other two cases show the region of greatest mass flux along the western coast. Despite these differences, the expected trend of overall mass loss along the margins of the Greenland ice sheet with small amounts of mass gain in the center of the ice sheet is clearly evident. Inspection of Figure 3.3 shows that differences between the different GRACE solutions in frames A to C of Fig. 3.2 do produce significant differences in the associated sea-level fingerprints but only over Greenland (Frame F in Figure 3.3).

The data sets for Antarctica (Figure 3.2 F-J) show greater variation compared to Greenland. As expected, the region of greatest mass change is located in the West Antarctic ice sheet. However, regions of alternating positive and negative mass loss can be observed to varying extents in all three cases. These alternating patterns are parallel to lines of longitude and appear to be indicative of the striping pattern associated with systematic errors in the GRACE data due to correlations between coefficients. The output which shows the greatest magnitude of these systematic errors is that of

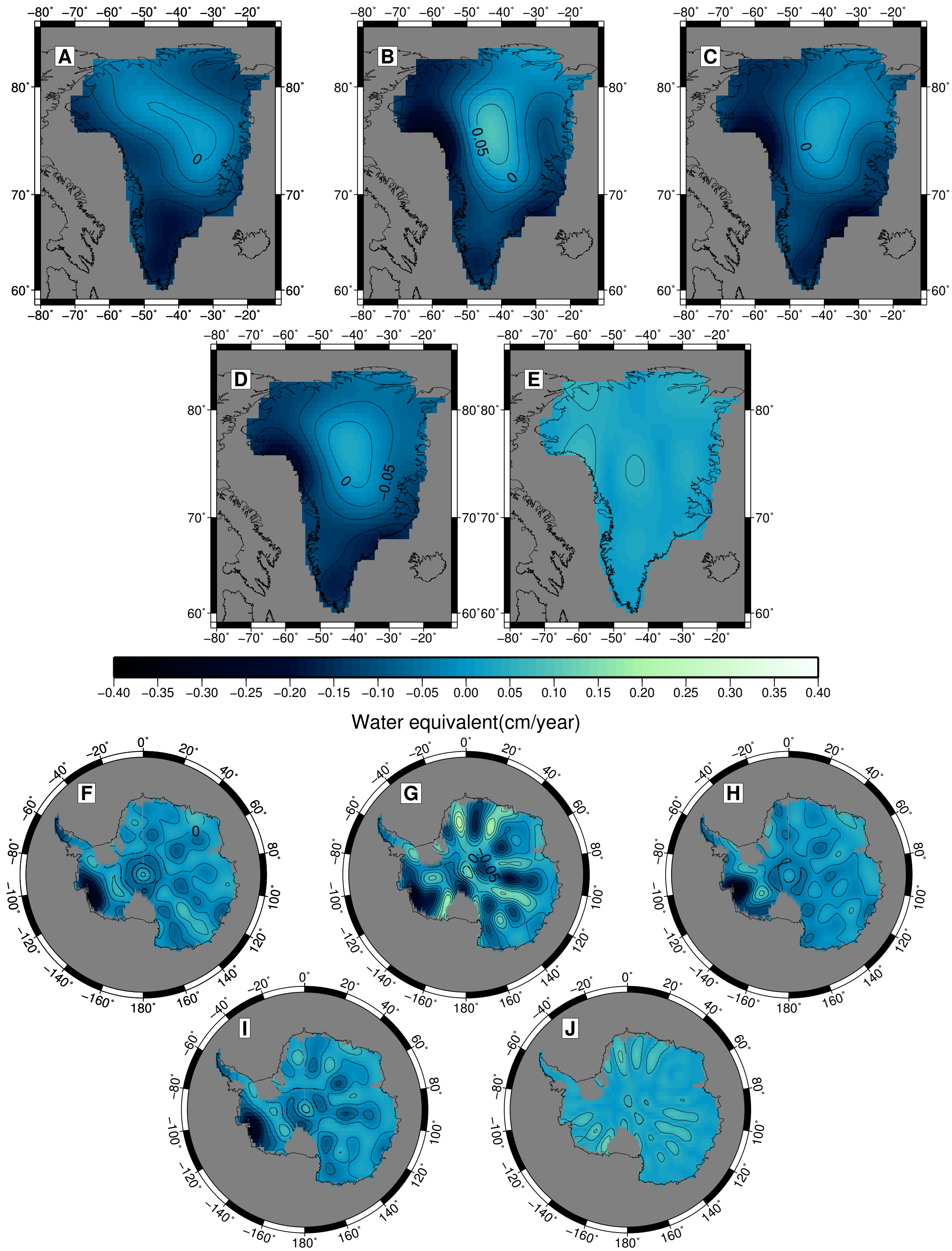

Figure 3.2: Ice thickness changes inferred using linear regression of the GRACE data time series from 2006CE-2012CE. A through C show Greenland changes for data provided by the CSR, JPL and GFZ processing facilities, respectively. The inputs to the sea level model have been scaled such that, prior to normalization, they have a global mean rate of 1 mm/ a sea level rise. The mean and standard deviation of these results are shown, respectively, in frames D and E. Frames F through J show the equivalent results but for Antarctica.

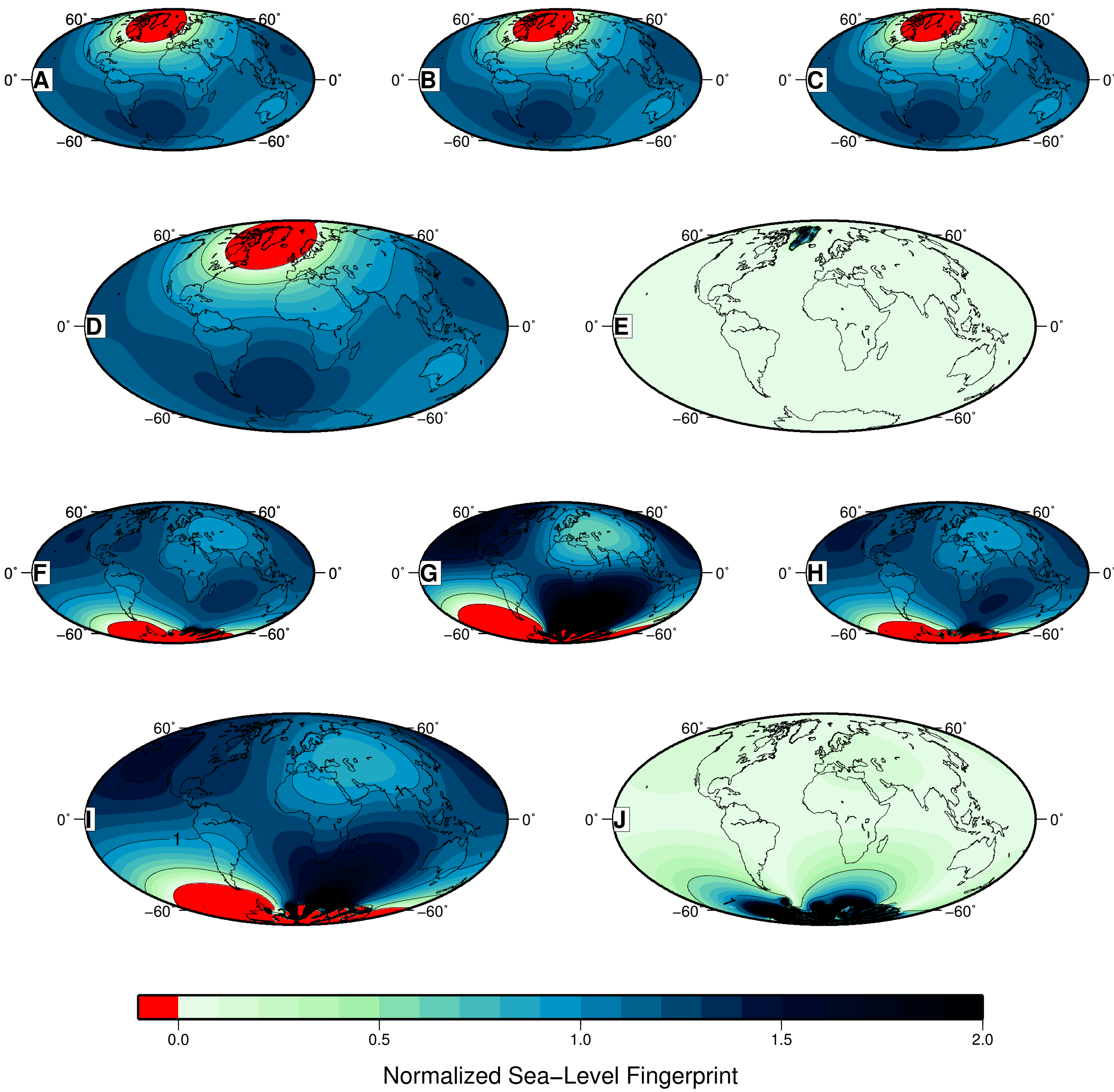

Figure 3.3: Frames A through E correspond to the normalized sea level fingerprints using the ice changes shown in the same frames in Figure 3.2. Similarly, frames F through J are the fingerprints associated with the result in frames F-J of Figure 3.2. All fingerprints are calculated using a spherical harmonic truncation of degree 512.

theJPL data center. Despite these systematic errors, we still see good agreement with a trend of mass loss in West Antarctica and relatively little change in the interior of East Antarctica. Examining the associated sea level fingerprints we see that the variation between models betweenJPL and either ofGFZ andCSR produces the largest differences in sea-level change. In this case, there are some significant differences between the fingerprints even in the far field. This is dominated by the different rotational signals produced (particularly that of theJPL solution compared to the other two).

In many past studies, sea-level fingerprints are often computed assuming relatively simple ice sheet change scenarios such as a uniform scaling of ice thickness as in Mitrovica et al. [2001]. More realistic ice sheet changes can produce significantly different fingerprint patterns as was shown in Mitrovica et al. [2011]. We therefore compute fingerprints assuming a uniform ice thickness scaling in order to evaluate the sensitivity of our results to this aspect of the computation. In Figure 3.4 it is evident that the GRACE derived results vary considerably from the uniform melt scenarios. We see a distinct dipole pattern over Greenland, likely due to the mass gains in the interior of the ice sheet in the GRACE derived melt scenarios. For the Antarctic scenarios, the rotational component (spherical harmonic degree 2 order 1, Y_2^1, pattern) plays a significant role in the difference between the uniform melt scenarios and the GRACE derived scenarios. Examining Figure 3.4 we can clearly see the dominance of Y_2^1 in the difference pattern.

Influence of Resolution

Our model solves the appropriate equations using the (spectral) viscoelastic Love number theory of Peltier [1974] and is discussed briefly in Section 1.2.1. As such our results are dependent upon the degree to which the results are calculated. To examine the impact of resolution on our results, the same raw input was used in our sea level code at 256, 512, and 1024 degree truncation, approximately equivalent to 40, 20 and 10 minute spatial resolution respectively. To examine the influence of this model aspect on our sea level estimates for our region of interest, we obtained the normalized sea level fingerprint values at 8 major cities along the east coast of North America and plotted the values as a function of spherical harmonic truncation (see Figure 3.5). Examining the results we see that there is little effect on the results between 512 and 1024 whereas there is a reasonably significant difference between 256 and 512, upwards of values of 0.3 between the two. As such it would seem that the results support running our model of sea level using a truncation of 512 or higher in order to adequately capture the response and calculate the fingerprints for any given melt scenario as examined in this study. All fingerprints used in this analysis are calculated at degree 512 unless otherwise noted. The only discrepancy of note is that the JPL Antarctic data set did not show as similar values between 512 and 1024 as was observed for both CSR and GFZ.

Projections Due to Changes in Ice Sheets

The results in Figure 3.5 examine the impact these fingerprints have on future sea level rise due to mass changes in the Greenland and Antarctic ice sheets. Changes in the Antarctic ice sheet will be magnified by a factor of $\approx 1.3 - 1.4$ times the eustatic sea level rise in our region of interest. Since this region is well into the far field of Antarctica we see a uniform shift along the coastline with little to no spatial variation. The change in sea level due to changes in Greenland, however, do vary along the

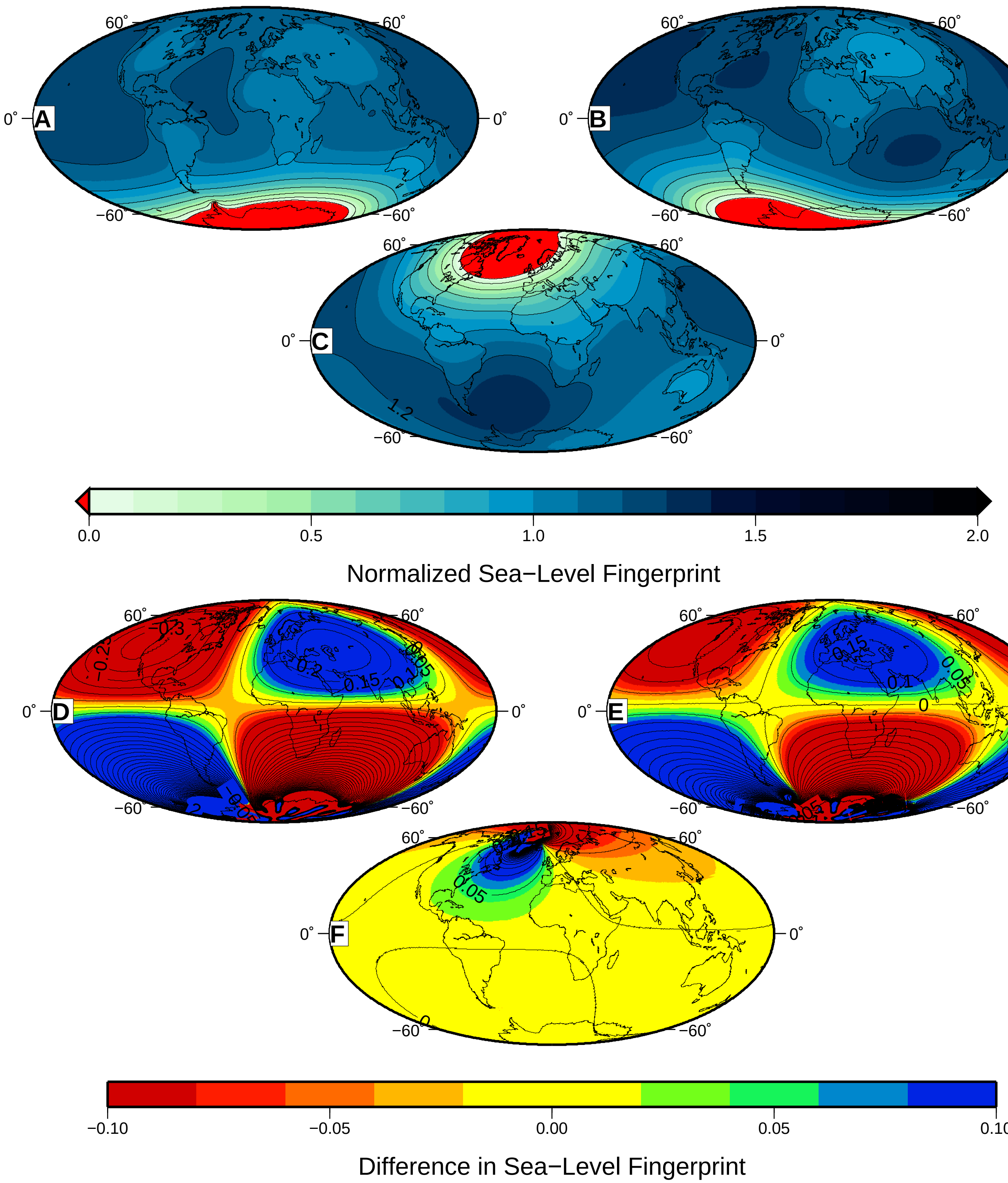

Figure 3.4: Normalized sea level fingerprints for the uniform melt scenarios, where a constant thickness of ice was removed for the whole of Antarctica (A), the West Antarctic ice sheet (B) and Greenland (C). Frames D, E, and F are the difference between A, B and C and their respective GRACE derived fingerprints (Figure 3.3 Frames D & I). All fingerprints were calculated using a spherical harmonic truncation of degree 512.

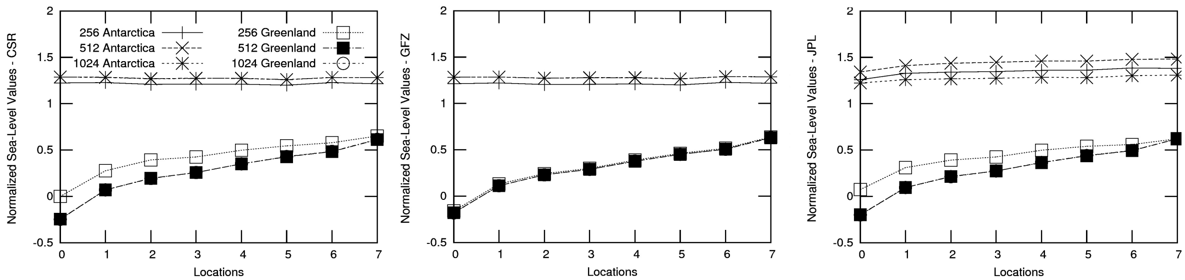

Figure 3.5: Normalized sea level fingerprints at varying spherical harmonic truncation for 8 cities along the east coast of North America. The locations are (North to South): 0-St. Johns NF, 1-Halifax NS, 2-Portland ME, 3-Boston MA, 4-New York City NY, 5-Washington DC, 6-Virginia Beach VA, 7-Charleston SC. Note that while there is a distinct difference truncating at degree 256 and 512, the difference between 512 and 1024 is almost not visable at this scale.

coastline with increasing values from North to South by a factor of $\approx -0.1 - 0.7$ times the eustatic sea level change. When we combine these values with projected sea level change as presented in the latest IPCC report we obtain the results in Table 3.3. If we examine the standard deviation in the Greenland and Antarctic fingerprints, $0.01 - 0.03$ and $0.03 - 0.1$ respectively, for our sites of interest, we see that this range in values is comparatively less than the likely range in the IPCC results. For comparison, assuming a eustatic sea level rise of 10 cm the differences between the models would result in at most order 1 mm and 1 cm for Greenland and Antarctica respectively.

Source/Location	RCP2.6 (cm)	RCP4.5 (cm)	RCP6.0 (cm)	RCP8.5 (cm)
Greenland (GMSL)	6.0 (4.0 – 10.0)	8.0 (4.0 – 13.0)	8.0 (4.0 – 13.0)	12.0(7.0 – 21.0)
St. Johns, NF	-1.2(-0.8 – -2.1)	-1.7(-0.8 – -2.7)	-1.7(-0.8 – -2.7)	-2.5 (-1.5 – -4.4)
Halifax, NS	0.6 (0.4 – 0.9)	0.7 (0.4 – 1.2)	0.7 (0.4 – 1.2)	1.1 (0.7 – 2.0)
Portland, ME	1.3 (0.9 – 2.1)	1.7 (0.9 – 2.8)	1.7 (0.9 – 2.8)	2.6 (1.5 – 4.5)
Boston, MA	1.6 (1.1 – 2.7)	2.2 (1.1 – 3.6)	2.2 (1.1 – 3.6)	3.3 (1.9 – 5.8)
New York City, NY	2.2 (1.5 – 3.6)	2.9 (1.5 – 4.7)	2.9 (1.5 – 4.7)	4.4 (2.5 – 7.6)
Washington, DC	2.6 (1.8 – 4.4)	3.5 (1.8 – 5.7)	3.5 (1.8 – 5.7)	5.3 (3.1 – 9.2)
Virgina Beach, VA	3.0 (2.0 – 4.9)	4.0 (2.0 – 6.4)	4.0 (2.0 – 6.4)	5.9 (3.5 – 10.4)
Charleston, SC	3.7 (2.5 – 6.2)	5.0 (2.5 – 8.1)	5.0 (2.5 – 8.1)	7.5 (4.4 – 13.1)
Antarctica (GMSL)	5.0 (-3.0 – 14.0)	5.0 (-4.0 – 13.0)	5.0 (-4.0 – 13.0)	4.0 (-6.0 – 12.0)
St. Johns, NF	6.5 (-3.9 – 18.3)	6.5 (-5.2 – 17.0)	6.5 (-5.2 – 17.0)	5.2 (-7.8 – 15.6)
Halifax, NS	6.6 (-4.0 – 18.6)	6.6 (-5.3 – 17.2)	6.6 (-5.3 – 17.2)	5.3 (-8.0 – 15.9)
Portland, ME	6.6 (-4.0 – 18.6)	6.6 (-5.3 – 17.2)	6.6 (-5.3 – 17.2)	5.3 (-8.0 – 15.9)
Boston, MA	6.7 (-4.0 – 18.7)	6.7 (-5.3 – 17.3)	6.7 (-5.3 – 17.3)	5.3 (-8.0 – 16.0)
New York City, NY	6.7 (-4.0 – 18.7)	6.7 (-5.3 – 17.4)	6.7 (-5.3 – 17.4)	5.3 (-8.0 – 16.0)
Washington, DC	6.6 (-4.0 – 18.6)	6.6 (-5.3 – 17.3)	6.6 (-5.3 – 17.3)	5.3 (-8.0 – 15.9)
Virgina Beach, VA	6.8 (-4.1 – 18.9)	6.8 (-5.4 – 17.6)	6.8 (-5.4 – 17.6)	5.4 (-8.1 – 16.2)
Charleston, SC	6.7 (-4.0 – 18.9)	6.7 (-5.4 – 17.5)	6.7 (-5.4 – 17.5)	5.4 (-8.1 – 16.2)

Table 3.3: Sea Level projections for selected cities along the East Coast of North America at 2100CE. Values for GMSL contributions obtained from (Church et al. [2013]) and the projections are the result of the multiplication of our normalized sea level fingerprints (Figure 3.3 D & I) by these GMSL values. The likely range given by the latest IPCC report (Church et al. [2013]) when multiplied by our fingerprint factors is given in brackets.

3.4 Projected Mass Changes of Glaciers & Ice Caps

The contributions to changing sea levels from GICs, as discussed in Section 1.2.2, present one of the greater unknowns in generating sea level predictions. While their locations and areas are reasonably well constrained via databases like the RGI(Arendt et al.), the volume of the world's glaciers remain quite uncertain. Ideally there would exist a global distribution of ice thickness produced via remote sensing techniques from which we could obtain ice volumes, but at present such an endeavour is beyond our means. We can absolve this issue somewhat through the use of various methods to approximate GICs volume from area which is much easier to determine via remote sensing. Multiple studies exist that allow us to determine volumes from areas for a given GIC, such as Radić and Hock [2010] and Huss and Farinotti [2012]. Despite their limitations in primarily employing empirical trends, these studies remain useful because, as more accurate estimates of ice area are produced, we ought to subsequently obtain more accurate volumes if the scaling relations hold. Given the combination of a database like the RGI and a scaling methodology like that presented in Huss and Farinotti [2012] we can obtain volumes of ice as a distribution on the surface of the Earth as described in Section 3.4.1.

3.4.1 Methods

We follow the methods adopted in Radić and Hock [2010] and Huss and Farinotti [2012] to approximate glacier volumes via statistical up-scaling from known glacier volumes. In this study we utilize the area to mean thickness scaling coefficients of Huss and Farinotti [2012] along with the glacier outlines of Arendt et al.. Huss and Farinotti [2012] use a relationship between area and average thickness

$$\bar{h} = cS^{\gamma}, \tag{3.3}$$

where $\bar{h}$ is the mean glacier thickness, c, γ are scaling coefficients and S is the glacier area. The study of Huss and Farinotti [2012] provides scaling coefficients for each of the 19 regions in the RGI, typical values for c are between 0.3 $\mathrm{m}^{1-2\gamma}$ and 0.6 $\mathrm{m}^{1-2\gamma}$ and typical values for γ are between 0.25 and 0.35. Using these values and determining volume from them we can then use the values as input to the sea level fingerprinting model applied to ice sheets in Section 3.3.To use the glacier volumes as input loads to our model we sum up the volumes of the glaciers and bin them at the required resolution[3].

In order to determine the contribution of the glaciers to changes in sea level we require information regarding their rates of mass loss, for which we adopt the results of Marzeion et al. [2012]. In their study they utilize climate model output (CMIP5) to drive a surface mass balance model of GICs. They provide information regarding the melt volume of GICs as a function of location(region in the RGI), time, climate model and RCP scenario. We can use this information in combination with the (normalized) sea level fingerprints we generated previous, some of which are shown in Figure 3.6) to determine the sea level rise due to a given glacier region in the RGI as a function of time, climate model, RCP scenario, latitude and longitude.

[3]This was done at a truncation of 512 as a similar resolution test was conduced as for the ice sheets and was found to be optimal

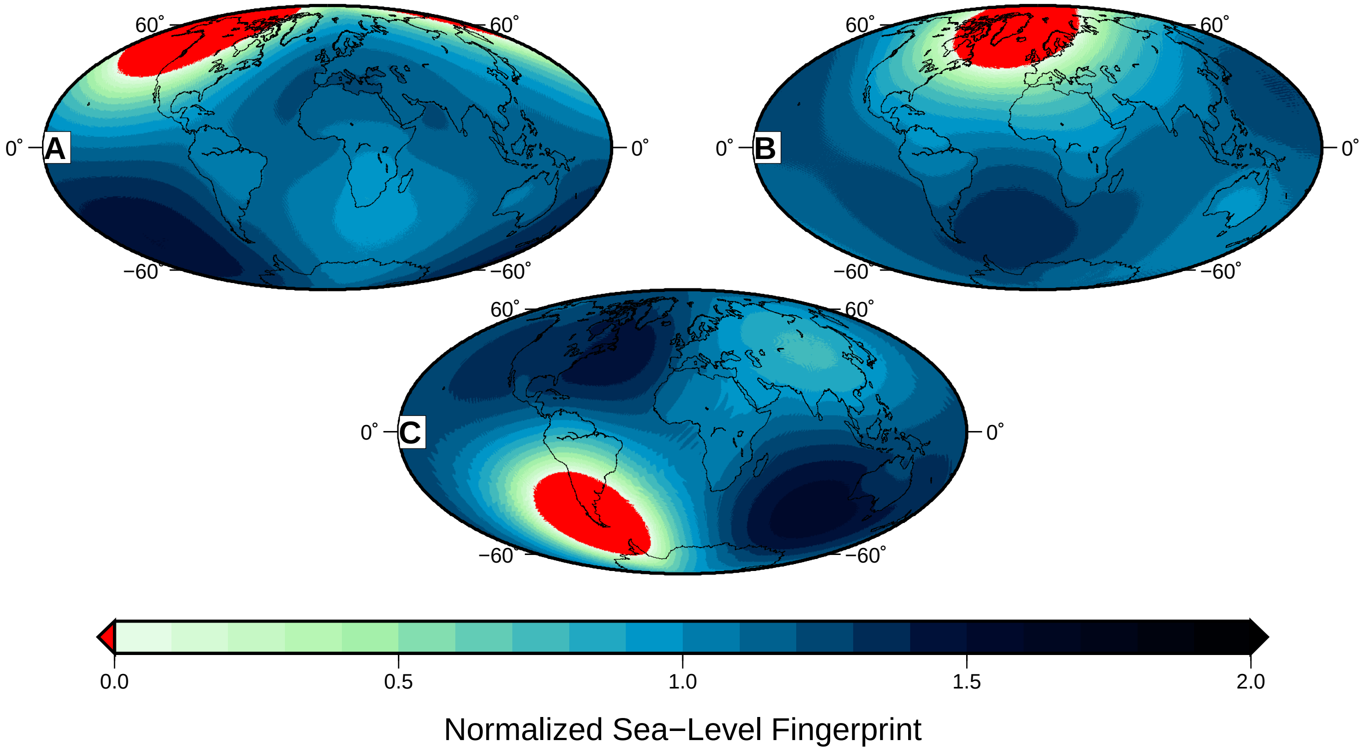

Figure 3.6: Normalized sea level fingerprints for Alaska, the Greenland periphery and Southern Andes GICs respectively. Alaska and the Greenland periphery are among the most influential contributors for the east coast of North America. The Southern Andes are included here for as an example of the pattern of a far field site for the east coast.

3.4.2 Results & Discussion

For our region of interest, the glacier complexes of greatest importance are those in closest proximity and largest melt rates, namely, those of the Canadian Arctic and the periphery of Greenland. The maximum contribution of each glacier complex present in the RGI that we calculate using the volume-area scaling coefficients presented in Huss and Farinotti [2012] are in Table 3.4. Note that, the Antarctic periphery glaciers are not going to be considered in this part of the study. Given the difficulty in distinguishing periphery glaciers from the main body of the ice sheet we have elected to combine them with the ice sheet for this study in the same fashion as other projection studies Church et al. [2013]. In general the more northerly the site, the greater the influence of the sea level fingerprint, as demonstrated in Figure 3.7. To determine the individual values for a location, we use the following

$$\Delta SL_{glacier} = (SL_{eust}(t, R, M, G) - SL_{eust}(t_0, R, M, G)) \times N_{fp}(\theta, \phi, G), \tag{3.4}$$

where SL_{eust} is the eustatic sea level value for a given RCP scenario R, climate model M, and a glacier complex G; N_{fp} is the normalized sea level fingerprint. As can be seen in Figure 3.7 the fingerprint values are fairly evenly split between below average values and above average, however when one considers the magnitude of the eustatic contribution we see that the values for our locations of interest are somewhat lower. Table 3.5 contains results of using the generated fingerprints in conjunction with the output of Marzeion et al. [2012]. We can see that in general the values for major cities along the east coast are lower than the eustatic.

Source	Maximum Eustatic Contribution (cm)
Alaska	4.86
Western Canada & US	0.23
Arctic Canada North	9.26
Arctic Canada South	2.38
Greenland Periphery	6.14
Iceland	0.61
Svalbard	2.39
Scandinavia	0.04
Russian Arctic	2.81
NorthAsia	0.03
CentralEurope	0.03
Caucasus Middle East	0.01
Central Asia	0.8
South Asia West	0.9
South Asia East	0.31
Low Latitudes	0.02
Southern Andes	0.98
New Zealand	0.01
Total:	25.67

Table 3.4: Maximum contributions for each of the RGI locations using the scaling coefficient of Huss and Farinotti [2012].

2100CE	RCP26 (cm)	RCP45 (cm)	RCP60 (cm)	RCP85 (cm)
St. Johns, NF	8.4±1.8	9.5±2.2	9.5±2.0	12.4±2.5
Halifax, NS	9.1±2.0	10.3±2.4	10.2±2.2	13.4±2.7
Portland, ME	9.1±2.0	10.3±2.4	10.3±2.3	13.4±2.7
Boston, MA	9.5±2.1	10.7±2.5	10.6±2.4	13.9±2.8
New York City, NY	9.8±2.2	11.1±2.7	11.1±2.5	14.5±2.9
Washington, DC	9.9±2.2	11.2±2.7	11.1±2.5	14.6±3.0
Virgina Beach, VA	10.5±2.3	11.9±2.9	11.8±2.7	15.5±3.2
Charleston, SC	11.0±2.5	12.4±3.0	12.4±2.9	16.3±3.4
Eustatic	12.3±2.8	13.8±3.5	13.8±3.3	18.2±3.9

Table 3.5: Using the fingerprints generated by our sea level model and the data provided by Marzeion et al. [2012] we determined the above projections due to the melting of GICs. Values provided are the multi-model ensemble mean ± one standard deviation.

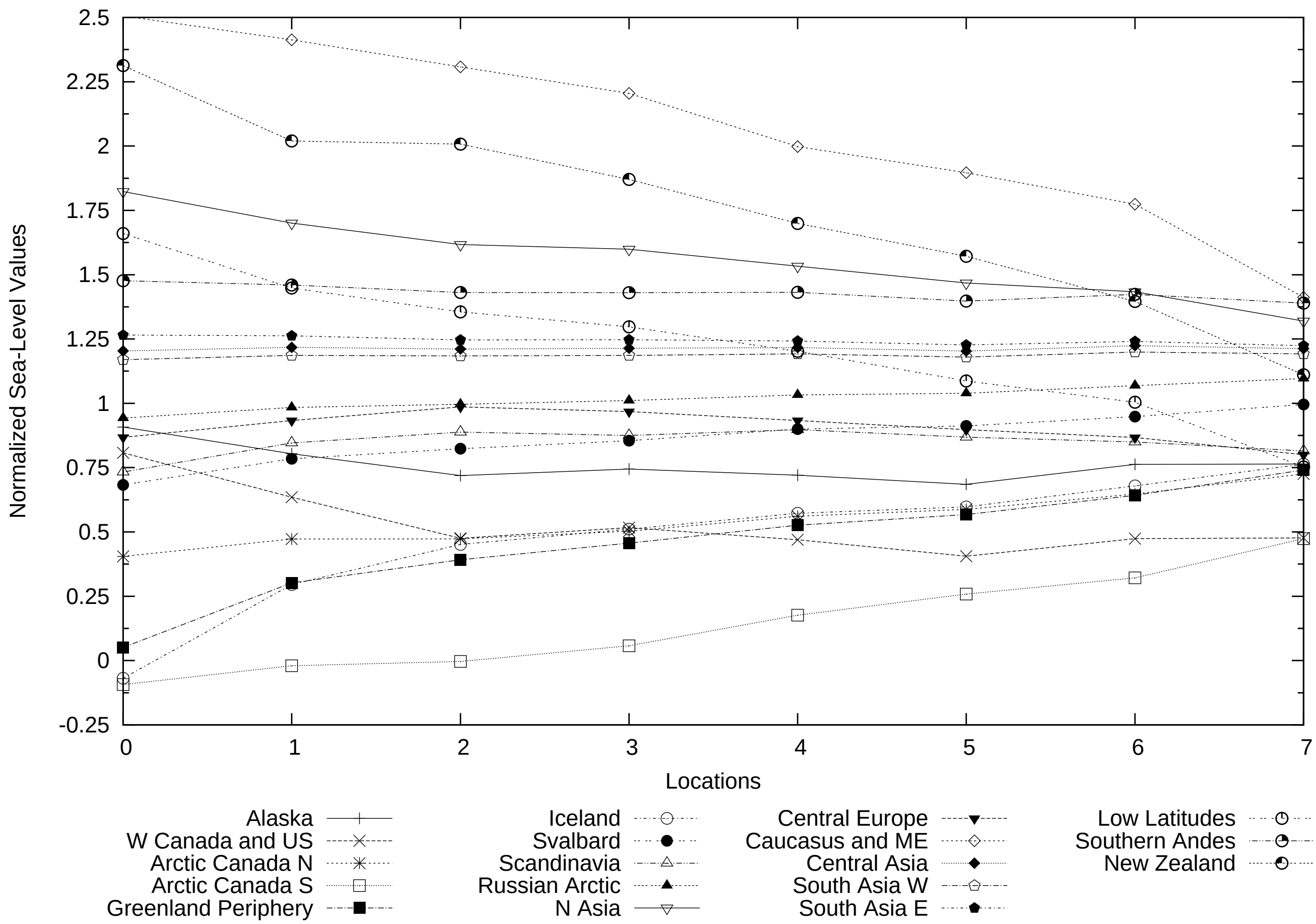

Figure 3.7: Normalized sea level fingerprints at 8 cities from North to South along the east coast of North America for each of the RGI regions considered in this study, calculated using the sea level equation as discussed in Sections 1.2.1 and 1.2.2. The locations are as follows, 0-St. Johns NF, 1-Halifax NS, 2-Portland ME, 3-Boston MA, 4-New York City NY, 5-Washington DC, 6-Virginia Beach VA, 7-Charleston SC. Note that these values are normalized with resepect to the global average sea level change for each source region.

3.5 Conclusions

Having determined the contributions from each component considered in this chapter we summarise the results in Figure 3.8, where the relative magnitudes of each contribution are given at a selection of locations. The greatest of the three contributions considered is due to ocean heat uptake and the associated effects as discussed in Section 3.2. The contributions from GICs are the second most prominent followed by the contribution from the Antarctic and Greenland ice sheets respectively. Interestingly, even though each contribution has an associated spatial pattern, we find that the summed contribution each site is quite similar. This is because while the thermal expansion contribution decreases southward along the coastline, the contribution from Greenland counters this effect. However, there is still a slight decrease in sea level change from South to North. In addition, this effect drops off as the thermal expansion contribution increases due to the changing climate scenario and we find differences of around 5 cm between sites. Finally, we find that using the mean values we obtain projections as high as 55 cm for the warmest and most extreme of climate scenarios for the major cities in our region of interest.

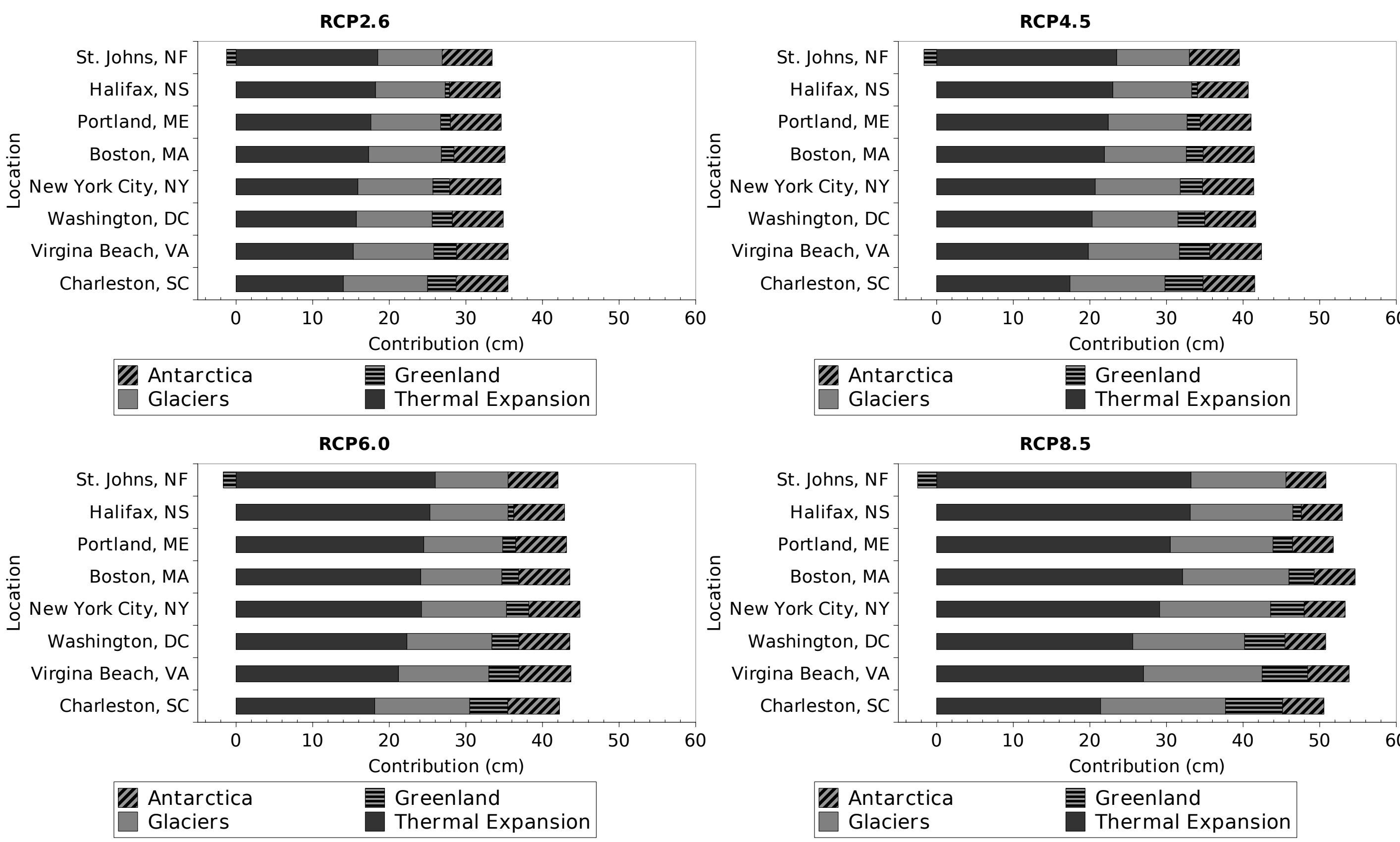

.

Figure 3.8: The total contributions to changes in sea level at 2100CE due to the processes discussed in this chapter. The greatest source of sea level change is that associated with heat uptake in the oceans and associated effects (see Section 3.2)

Chapter 4

Conclusions

Having produced the relevant data presented in Chapters 2 and 3, we have achieved our primary research goals: (i) providing an improved estimate of the GIA response of the east coast of North America and (ii) projecting future changes in sea level in this region at 2100CE associated with the expected dominant processes. In Chapter 2, using a model of sea level and GIA, along with the sea level dataset of Engelhart and Horton [2012], we determined the best fitting model parameters. These best fitting parameters allow us to use our model to project future changes in sea level due to GIA. Similarly, in Chapter 3, we determine the other relevant contributions to sea level change such as thermal expansion, mass changes in ice sheets, GICs along with their associated spatial distributions. The results of this investigation are presented in Figure 4.1 where we can see that the greatest contributor to future changes in sea level will be that of thermal expansion. This result is as expected given that similar studies such as Church et al. [2013] obtained the same conclusion. Location and RCP depending, we find that GIA is the second most prominent contributor and shows the greatest spatial variability (Figure 4.2). Due to the spatial variability involved from all contributors, but primarily from thermal expansion and GIA, we find that the center of our region exhibits the largest change in sea level. Including all sources of sea level change presented in this thesis, summarised in Figure 4.1, we can see that the lowest amount of change by 2100CE is ≈ 35 cm and the highest is ≈ 70 cm when we use the ensemble mean values.

The greatest source of uncertainty in the projections comes from differences between climate models and sea level changes due to thermal expansion and its associated effects. As discussed in Chapter 3, while the models typically agree on the sign of sea level change, they often disagree on the magnitude resulting in a large uncertainty in the model ensemble mean value for any given location and scenario. Subsequently, given that the results for the glaciers, ice caps and the ice sheets use as input the same climate scenarios and climate model output[1], this source of uncertainty also impacts these results. GIA, which for this region is independent of changes in contemporary and future climate, has the lowest uncertainty even amongst a large ensemble such as the best fitting 1% of model runs out of the total ensemble of ≈ 15000 considered in this study. Table 4.1 provides a summary of the contributions from the processes considered and their respective uncertainties.

[1] in the case of the GICs, less so in the case of the ice sheet changes

By comparison to the work of Church et al. [2013], we find our projections to be somewhat below those produced for GMSL despite our inclusion of the GIA contribution to sea level [2] along the east coast of North America (Figure 4.1). Excluding GIA, we find our regional projections to be even further below[3] those of GMSL presented by Church et al. [2013], which serves to highlight the importance of GIA in projections of sea level for this region as it can be upwards of 1/4 of the total change. This difference between our regional projections and the GMSL values of Church et al. [2013] is due primarily to the spatial variability of the signal from the Greenland and Antarctic ice sheets. Greenland, which is projected to contribute $\approx 12cm$ of GMSL change by the close of 2100CE, is quite close to our region of interest, as such, the gravitational effect due to the decreasing mass of the ice sheet will cause lower than average (eustatic) sea level rise. Spatial variability in the contribution from the Antarctic ice sheets counters this somewhat, but the signal is much smaller. Our determination of the contribution from GICs are very close to the GMSL values provided by Church et al. [2013], indicating that the spatial signal (fingerprints) due to the different sources largely cancels for this coastline. Of note, is that these changes in future sea level will exacerbate any extreme weather events, which are projected to occur with greater frequency according to the work of Church et al. [2013]. As well, referring back to the results found by Hanson et al. [2011], note that they utilized a sea level rise of only 50 cm and we project even higher for some locations, therefore the regions and resources susceptible to flooding and extreme weather events can quite possibly be larger.

Future work to improve upon or enhance this study should primarily focus upon the reduction of uncertainty, primarily in the contribution due to thermal expansion and the associated effects. The simplest and most straightforward approach would be to increase the number of climate models used in the study. Future work which constrain future changes in the ice sheets would also serve to reduce uncertainty as there have only been few studies in this regard and as such the contributions outlined here and in the work of Church et al. [2013] show a large range of uncertainty. Ideally, enhancements to climate models and refinement of future climate scenarios ought to reduce uncertainty in the estimates from thermal expansion and associated effects, however this remains uncertain given the complex nature of these models.

In conclusion, our results for the east coast of North America are within the likely range of the IPCC GMSL projections with the mean values generally being less (more so when GIA is not included). This is largely because the signal due to land ice melt (Greenland in particular) is considerably lower that the global mean and the contribution from GIA is not large enough to compensate. Finally, our results demonstrate that GIA is a major contributor to sea level change in this region and is expected to contribute upwards of $\approx 25\%$ of the total change in sea level by 2100CE.

[2] Note that GIA does not contribute to GMSL

[3] Note however that our projections are still within the likely range of the IPCC projections

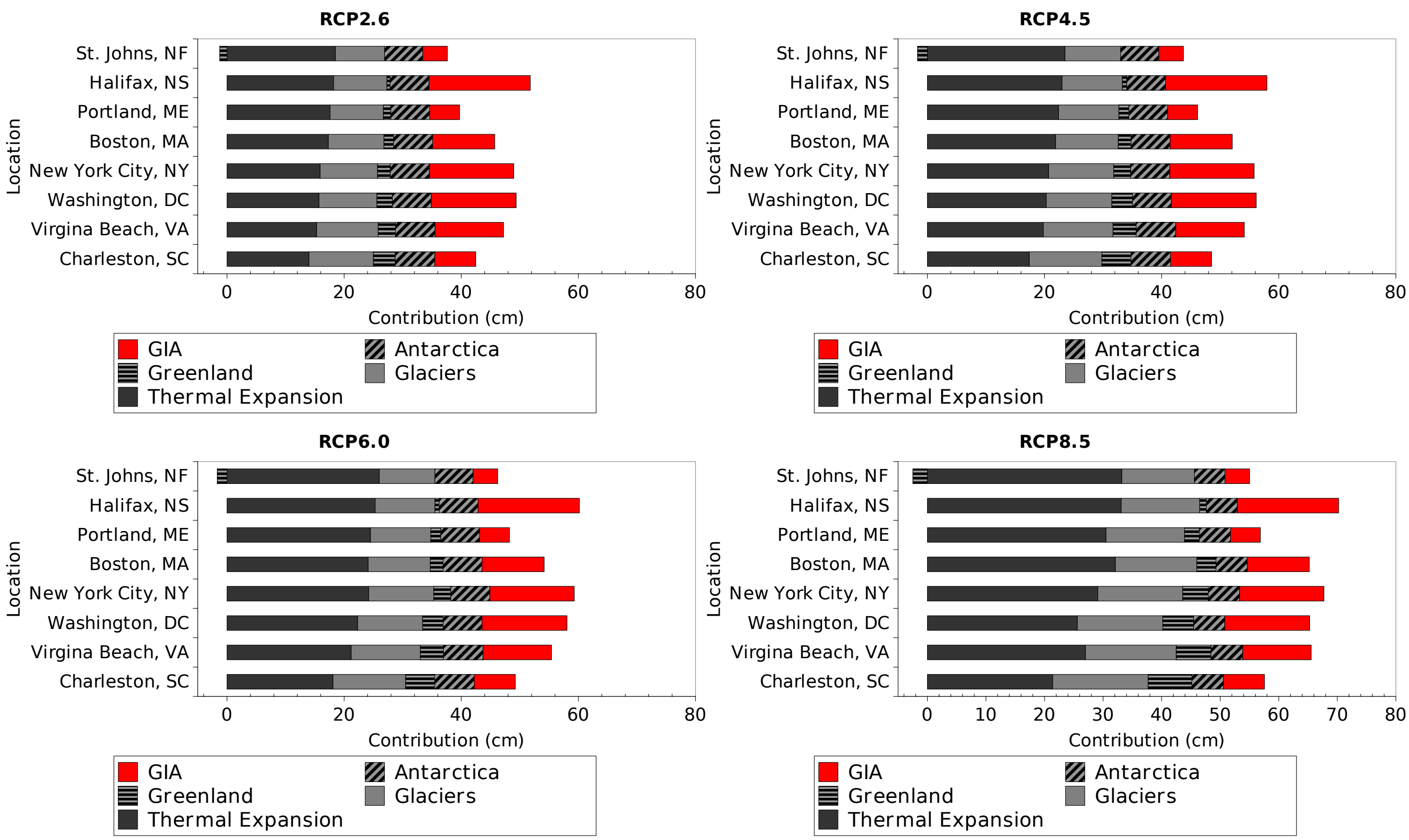

Figure 4.1: The total contributions to changes in sea level at 2100CE as given in each previous chapter. As in Figure 3.8 we find that the greatest source of sea level change is that of thermal expansion and the other effects as discussed in Section 3.2. GIA, depending on the site, is the second greatest contributor to sea level change and also shows the greatest spatial variability.

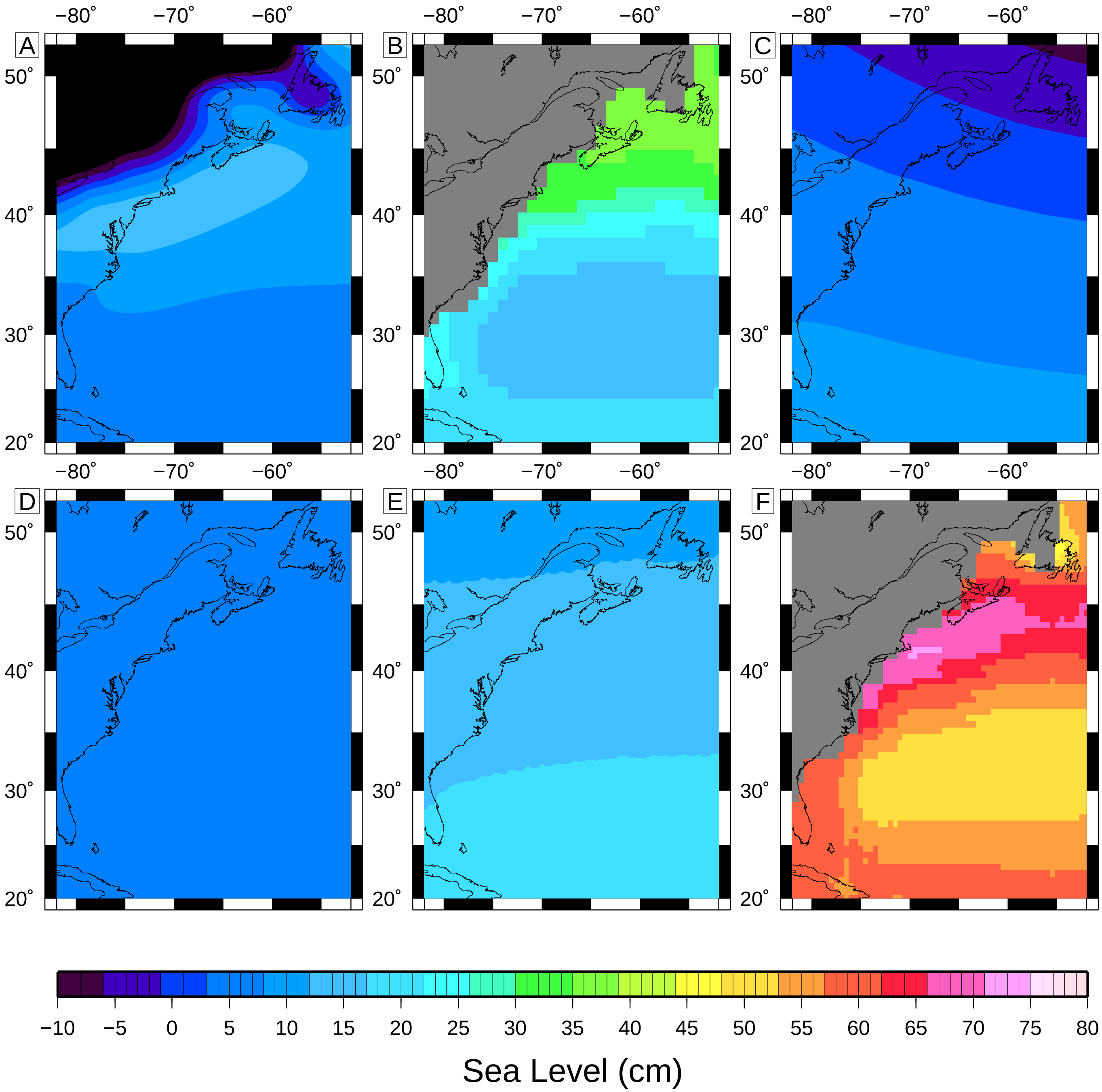

Figure 4.2: Spatial plots of each of the component signals at considered in this thesis for the RCP8.5 scenario at the year 2100CE(excepting the thermal expansion component as it is the difference of 2085CE-2100CE and 2006CE-2015CE). Frames A through F are GIA, thermal expansion, the Greenland ice sheet, the Antarctic ice sheets, GICs and the sum of each of these, respectively.

	2100CE	St. John's NF	Halifax NS	Portland ME	Boston MA	New York City, NY	Washington DC	Virginia Beach, VA	Charleston SC
	GIA	4.2±5.9	17.3±4.8	5.1±2.3	10.6±1.4	14.4±1.5	14.5±1.4	11.7±1.5	7.0±2.0
RCP2.6	Thermal Expansion	18.5±13.7	18.2±13.6	17.6±13.4	17.3±13.4	15.9±13.4	15.7±12.6	15.3±12.2	14.0±10.4
	Glaciers	8.4±1.8	9.1±2.0	9.1±2.0	9.5±2.1	9.8±2.2	9.9±2.2	10.5±2.3	11.0±2.5
	Greenland	-1.2±0.6	0.6±0.3	1.3±0.7	1.6±0.8	2.2±1.1	2.6±1.3	3.0±1.5	3.7±1.9
	Antarctica	6.5±9.2	6.6±9.4	6.6±9.4	6.7±9.5	6.7±9.5	6.6±9.4	6.8±9.6	6.7±9.5
	Total	36.4±17.6	51.8±17.3	39.7±16.6	45.7±16.6	49.0±16.7	49.3±16.0	47.3±15.9	42.4±14.6
RCP4.5	Thermal Expansion	23.5±16.5	23.0±16.8	22.4±16.5	21.9±16.3	20.7±16.0	20.3±14.9	19.8±14.5	17.4±13.0
	Glaciers	9.5±2.2	10.3±2.4	10.3±2.4	10.7±2.5	11.1±2.7	11.2±2.7	11.9±2.9	12.4±3.0
	Greenland	-1.7±1.0	0.7±0.4	1.7±1.0	2.2±1.2	2.9±1.6	3.5±2.0	4.0±2.3	5.0±2.8
	Antarctica	6.5±11.1	6.6±11.2	6.6±11.2	6.7±11.4	6.7±11.4	6.6±11.2	6.8±11.6	6.7±11.4
	Total	42.0±20.9	57.9±20.9	46.1±20.3	52.1±20.1	55.8±19.9	56.1±19.0	54.2±19.0	48.5±17.9
RCP6.0	Thermal Expansion	26.0±20.2	25.3±20.5	24.5±20.5	24.1±20.1	24.2±20.3	22.3±18.6	21.2±17.7	18.1±15.3
	Glaciers	9.5±2.0	10.2±2.2	10.3±2.3	10.6±2.4	11.1±2.5	11.1±2.5	11.8±2.7	12.4±2.9
	Greenland	-1.7±1.0	0.7±0.4	1.7±1.0	2.2±1.2	2.9±1.6	3.5±2.0	4.0±2.3	5.0±2.8
	Antarctica	6.5±11.1	6.6±11.2	6.6±11.2	6.7±11.4	6.7±11.4	6.6±11.2	6.8±11.6	6.7±11.4
	Total	44.5±23.9	60.1±24.0	48.2±23.6	54.2±23.3	59.3±23.5	58.0±22.0	55.5±21.5	49.2±19.6
RCP8.5	Thermal Expansion	33.2±22.6	33.1±22.4	30.5±22.6	32.1±21.9	29.1±22.1	25.6±21.9	27.0±20.2	21.4±18.1
	Glaciers	12.4±2.5	13.4±2.7	13.4±2.7	13.9±2.8	14.5±2.9	14.6±3.0	15.5±3.2	16.3±3.4
	Greenland	-2.5±1.5	1.1±0.6	2.6±1.5	3.3±1.9	4.4±2.6	5.3±3.1	5.9±3.4	7.5±4.4
	Antarctica	5.2±11.7	5.3±11.9	5.3±11.9	5.3±11.9	5.3±11.9	5.3±11.9	5.4±12.2	5.4±12.2
	Total	52.5±26.3	70.2±26.0	56.9±25.8	65.2±25.2	67.7±25.5	65.3±25.3	65.5±24.1	57.6±22.6

Table 4.1: Contributions to changes in sea level as well as the relevant uncertainties as outlined in previous chapters.

Acknowledgements

We acknowledge the World Climate Research Programme's Working Group on Coupled Modelling, which is responsible for CMIP, and we thank the climate modelling groups (listed in Table 3.1 of this paper) for producing and making available their model output. For CMIP the U.S. Department of Energy's Program for Climate Model Diagnosis and Intercomparison provides coordinating support and led development of software infrastructure in partnership with the Global Organization for Earth System Science Portals.

Bibliography

C. Amante and B.W. Eakins. Etopo1 1 arc-minute global relief model: Procedures, data sources and analysis. *NOAA Technical Memorandum NESDIS NGDC-24*, 2009. doi: doi:10.7289/V5C8276M.

A Arendt, T. Bolch, J.G. Cogley, A. Gardner, J.O. Hagen, R. Hock, G. Kaser, W.T. Pfeffer, G. Moholdt, F. Paul, V. Radić, L. Andreassen, S. Bajracharya, N. Barrand, M. Beedle, E. Berthier, R. Bhambri, A. Bliss, I. Brown, D . Burgess, E . Burgess, F. Cawkwell, T. Chinn, L. Copland, B. Davies, H. D e Angelis, E. Dolgova, K. Filbert, R. R. Forester, A. Fountain, H. Frey, B. Giffen, N. Glasser, S. Gurney, W. Hagg, D. Hall, U.K. Haritashya, G. Hartmann, C. Helm, S. Herreid, I. Howat, G. Kapusti n, T. Khromova, C. Kienholz, M. Köonig, J. Kohler, D. Kriegel, S. Kutuzov, I. Lavrentiev, R. Le Bris, J. Lund, W. Manley, C. Mayer, E. Miles, X. Li, B. Menounos, A. Mercer, N. Mölg, P. Mool, G. Nosenko, A. Negrete, C. Nuth, R. Pettersson, A. Racoviteanu, R . Ranzi, P. Rastner, F. Rau, B. Raup, J. Rich, H. Rott, C. Schneider, Y. Seliverstov, M. Sharp, O. Siguròsson, C. Stokes, R. Wheate, S. Winsvold, G. Wolken, F. Wyatt, and N. Zheltyhina. Randolph Glacier Inventory - A Dataset of Global Glacier Outlines : Version 3.2. Global Land Ice Measurements from Space.

D.L. Balk, U. Deichmann, G. Yetman, F. Pozzi, S.I. Hay, and A. Nelson. Determining global population distribution: Methods, applications and data. *Advances in Parasitology*, 62:119–156, 2006. doi: 10.1016/S0065-308X(05)62004-0.

J.L. Bamber, J.A. Griggs, R.T.W.L. Hurkmans, J.A. Dowdeswell, S.P. Gogineni, I. Howat, J. Mouginot, J. Paden, S. Palmer, E. Rignot, and D. Steinhage. A new bed elevation dataset for greenland. *The Cryosphere*, 7(2):499–510, 2013. doi: 10.5194/tc-7-499-2013. URL `http://www.the-cryosphere.net/7/499/2013/`.

Center for International Earth Science Information Network - CIESIN - Columbia University, International Food Policy Research Institute - IFPRI, The World Bank, and Centro Internacional de Agricultura Tropical - CIAT. Global Rural-Urban Mapping Project, Version 1 (GRUMPv1): Urban Extents Grid. Palisades, NY: NASA Socioeconomic Data and Applications Center (SEDAC), 2011. URL `http://dx.doi.org/10.7927/H4GH9FVG`.

J.A. Church, P.U. Clark, A. Cazenave, J.M. Gregory, S. Jevrejeva, A. Levermann, M.A. Merrifield, G.A. Milne, R.S. Nerem, P.D. Nunn, A.J. Payne, W.T. Pfeffer, D. Stammer, and A.S. Unnikrishnan. Sea level change. *Climate Change 2013: The Physical Science Basis. Contribution of Working Group I to the Fifth Assessment Report of the Intergovernmental Panel on Climate Change*, 2013.

U. Cubasch, D. Chen D. Wuebbles, M.C. Facchini, D. Frame, N. Mahowald, and J.G. Winther. Introduction. *Climate Change 2013: The Physical Science Basis. Contribution of Working Group I to the Fifth Assessment Report of the Intergovernmental Panel on Climate Change*, 2013.

J.L. Davis and J.X. Mitrovica. Glacial isostatic adjustment and the anomalous tide gauge record of eastern north america. 379, 1996.

P. Digranes, Y. Kristoffersen, and N. Karajev. An analysis of shear waves observed in vsp data from the superdeep well at kola, russia. *Geophysical Journal International*, 126(2):545–554, 1996. ISSN 1365-246X. doi: 10.1111/j.1365-246X.1996.tb05309.x. URL `http://dx.doi.org/10.1111/j.1365-246X.1996.tb05309.x`.

A.M. Dziewonski and D.L. Anderson. Preliminary reference earth model. *Physics of the Earth and Planetary Interiors*, 25:297–356, 1981.

S.E. Engelhart and B.P. Horton. Holocene sea level database for the atlantic coast of the united states. *Quaternary Science Reviews*, 54(0):12 – 25, 2012. ISSN 0277-3791. doi: http://dx.doi.org/10.1016/j.quascirev.2011.09.013. URL `http://www.sciencedirect.com/science/article/pii/S0277379111002927`. Coastal Change during the Late Quaternary.

S.E. Engelhart, W.R. Peltier, and B.P. Horton. Holocene relative sea-level changes and glacial isostatic adjustment of the u.s. atlantic coast. *Geology*, 2011. doi: 10.1130/G31857.1. URL `http://geology.gsapubs.org/content/early/2011/07/01/G31857.1.abstract`.

A.C. Eringen. *Mechanics of continua*. Wiley, 1967. URL `http://books.google.ca/books?id=34EpAQAAMAAJ`.

W.E. Farrell and J.A. Clark. On postglacial sea level. *Geophysical Journal of the Royal Astronomical Society*, 46(3):647–667, 1976. ISSN 1365-246X. doi: 10.1111/j.1365-246X.1976.tb01252.x. URL `http://dx.doi.org/10.1111/j.1365-246X.1976.tb01252.x`.

P. Fretwell, H.D. Pritchard, D.G. Vaughan, J.L. Bamber, N.E. Barrand, R. Bell, C. Bianchi, R.G. Bingham, D.D. Blankenship, G. Casassa, G. Catania, D. Callens, H. Conway, A.J. Cook, H.F.J. Corr, D. Damaske, V. Damm, F. Ferraccioli, R. Forsberg, S. Fujita, Y. Gim, P. Gogineni, J.A. Griggs, R.C. A. Hindmarsh, P. Holmlund, J.W. Holt, R.W. Jacobel, A. Jenkins, W. Jokat, T. Jordan, E.C. King, J. Kohler, W. Krabill, M. Riger-Kusk, K.A. Langley, G. Leitchenkov, C. Leuschen, B.P. Luyendyk, K. Matsuoka, J. Mouginot, F.O. Nitsche, Y. Nogi, O.A. Nost, S.V. Popov, E. Rignot, D.M. Rippin, A. Rivera, J. Roberts, N. Ross, M.J. Siegert, A.M. Smith, D. Steinhage, M. Studinger, B. Sun, B.K. Tinto, B.C. Welch, D. Wilson, D.A. Young, C. Xiangbin, and A. Zirizzotti. Bedmap2: improved ice bed, surface and thickness datasets for antarctica. *The Cryosphere*, 7(1):375–393, 2013. doi: 10.5194/tc-7-375-2013. URL `http://www.the-cryosphere.net/7/375/2013/`.

S. Hanson, R. Nicholls, N. Ranger, S. Hallegatte, J. Corfee-Morlot, C. Herweijer, and J. Chateau. A global ranking of port cities with high exposure to climate extremes. *Climatic Change*, 104(1):89–111, 2011. ISSN 0165-0009. doi: 10.1007/s10584-010-9977-4. URL `http://dx.doi.org/10.1007/s10584-010-9977-4`.

M. Huss and D. Farinotti. Distributed ice thickness and volume of all glaciers around the globe. *Journal of Geophysical Research: Earth Surface*, 117(F4):n/a–n/a, 2012. ISSN 2156-2202. doi: 10.1029/2012JF002523. URL `http://dx.doi.org/10.1029/2012JF002523`.

ICPO. WCRP Coupled Model Intercomparison Project - Phase 5. *Special Issue of the CLIVAR Exchanges Newsletter No.56*, 15(2), 2011.

C.A. Katsman, W. Hazeleger, S. Drijfhout, G. van Oldenborgh, and G. Burgers. Climate scenarios of sea level rise for the northeast atlantic ocean: a study including the effects of ocean dynamics and gravity changes induced by ice melt. *Climatic Change*, 91(3-4):351–374, 2008. ISSN 0165-0009. doi: 10.1007/s10584-008-9442-9. URL `http://dx.doi.org/10.1007/s10584-008-9442-9`.

R.A. Kendall, J.X. Mitrovica, and G.A. Milne. On post-glacial sea level - ii. numerical formulation and comparative results on spherically symmetric models. *Geophysical Journal International*, 161(3):679–706, 2005. ISSN 1365-246X. doi: 10.1111/j.1365-246X.2005.02553.x. URL `http://dx.doi.org/10.1111/j.1365-246X.2005.02553.x`.

F.W. Landerer and S.C. Swenson. Accuracy of scaled grace terrestrial water storage estimates. *Water Resources Research*, 48, 2012. doi: 10.1029/2011WR011453.

K. Latychev, J.X. Mitrovica, J. Tromp, M.E. Tamisiea, D. Komatitsch, and C.C. Christara. Glacial isostatic adjustment on 3-d earth models: a finite-volume formulation. *Geophysical Journal International*, 161(2):421–444, 2005. ISSN 1365-246X. doi: 10.1111/j.1365-246X.2005.02536.x. URL `http://dx.doi.org/10.1111/j.1365-246X.2005.02536.x`.

A.E.H. Love. *A Treatise on the Mathematical Theory of Elasticity*. Cambridge University Press, 1927. ISBN 9781107618091.

S.J. Marshall. *The Cryosphere*. Princeton Primers in Climate. Princeton University Press, 2011. ISBN 9781400840618.

B. Marzeion, A.H. Jarosch, and M. Hofer. Past and future sea-level change from the surface mass balance of glaciers. *The Cryosphere*, 6(6):1295–1322, 2012. doi: 10.5194/tc-6-1295-2012. URL http://www.the-cryosphere.net/6/1295/2012/.

J. Mitrovica and G.A. Milne. On post-glacial sea level: I. general theory. *Geophysical Journal International*, 154:253–267, 08/2003 2003. doi: 10.1046/j.1365-246X.2003.01942.x. URL http://adsabs.harvard.edu/abs/2003GeoJI.154..253M.

J.X. Mitrovica, M.E. Tamisiea, J.L. Davis, and G.A. Milne. Recent mass balance of polar ice sheets inferred from patterns of global sea-level change. *Nature*, 409:1026–1029, 2001.

J.X. Mitrovica, N. Gomez, E. Morrow, C. Hay, K. Latychev, and M.E. Tamisiea. On the robustness of predictions of sea level fingerprints. *Geophysical Journal International*, 187(2):729–742, 2011. ISSN 1365-246X. doi: 10.1111/j.1365-246X.2011.05090.x. URL http://dx.doi.org/10.1111/j.1365-246X.2011.05090.x.

W.R. Peltier. The impulse response of a maxwell earth. *Reviews of Geophysics*, 12(4):649–669, 1974. ISSN 1944-9208. doi: 10.1029/RG012i004p00649.

W.R. Peltier. Global glacial isostasy and the surface of the ice-age earth: the ice-5g (vm2) model and grace. *Annual Review of Earth and Planetary Sciences*, 32:111–149, May 2004.

W.R. Peltier and J.T. Andrews. Glacial-isostatic adjustment-i. the forward problem. *Geophysical Journal of the Royal Astronomical Society*, 46(3):605–646, 1976. ISSN 1365-246X. doi: 10.1111/j.1365-246X.1976.tb01251.x. URL http://dx.doi.org/10.1111/j.1365-246X.1976.tb01251.x.

W.R. Peltier and R. Drummond. Rheological stratification of the lithosphere: A direct inference based upon the geodetically observed pattern of the glacial isostatic adjustment of the north american continent. *Geophysical Research Letters*, 35(16):n/a–n/a, 2008. ISSN 1944-8007. doi: 10.1029/2008GL034586. URL http://dx.doi.org/10.1029/2008GL034586.

V. Radić and R. Hock. Regional and global volumes of glaciers derived from statistical upscaling of glacier inventory data. *Journal of Geophysical Research: Earth Surface*, 115(F1):n/a–n/a, 2010. ISSN 2156-2202. doi: 10.1029/2009JF001373. URL http://dx.doi.org/10.1029/2009JF001373.

G. Ranalli. *Rheology of the Earth*. Springer, 1995. ISBN 9780412546709.

J. Ritsema, A. Deuss, H.J. van Heijst, and J.H. Woodhouse. S40rts: a degree-40 shear-velocity model for the mantle from new rayleigh wave dispersion, teleseismic traveltime and normal-mode splitting function measurements. *Geophysical Journal International*, 184(3):1223–1236, 2011. ISSN 1365-246X. doi: 10.1111/j.1365-246X.2010.04884.x.

A. Shepherd, E.R. Ivins, G A, V.R. Barletta, M.J. Bentley, S. Bettadpur, K.H. Briggs, D.H. Bromwich, R. Forsberg, N. Galin, M. Horwath, S. Jacobs, I. Joughin, M.A. King, J.T.M Lenaerts, J. Li, S.R.M Ligtenberg, A. Luckman, S.B. Luthcke, M. McMillan, R. Meister, G. Milne, J. Mouginot, A. Muir, J. Nicolas, J. Paden, A.J. Payne, H. Pritchard, E. Rignot, H. Rott, L.S. Sørensen, T.A. Scambos, B. Scheuchl, E.J.O Schrama, B. Smith, A.V Sundal, J.H. van Angelen, W.J van de Berg, M.R van den Broeke, D.G. Vaughan, I. Velicogna, J. Wahr, P.L. Whitehouse, D.J. Wingham, D. Yi, D. Young, and H.J. Zwally. A reconciled estimate of ice-sheet mass balance. *Science*, 338(6111):1183–1189, 2012. doi: 10.1126/science.1228102. URL http://www.sciencemag.org/content/338/6111/1183.abstract.

A.B.A. Slangen, C.A. Katsman, R.S.W. van de Wal, L.L.A. Vermeersen, and R.E.M. Riva. Towards regional projections of twenty-first century sea-level change based on ipcc sres scenarios. *Climate Dynamics*, 38(5-6):1191–1209, 2012. ISSN 0930-7575. doi: 10.1007/s00382-011-1057-6. URL http://dx.doi.org/10.1007/s00382-011-1057-6.

M. Tamisiea, J.X. Mitrovica, J. Davis, and G.A. Milne. Ii: Solid earth physics: Long wavelength sea level and solid surface perturbations driven by polar ice mass variations: Fingerprinting greenland and antarctic ice sheet flux. *Space Science Reviews*, 108:81–93, 07/2003 2003. doi: 10.1023/A:1026178014950. URL http://adsabs.harvard.edu/abs/2003SSRv..108...81T.

O. Tange. GNU Parallel - The Command-Line Power Tool. *;login: The USENIX Magazine*, 36(1):42–47, Feb 2011. URL `http://www.gnu.org/s/parallel`.

L. Tarasov and W.R. Peltier. Greenland glacial history and local geodynamic consequences. *Geophysical Journal International*, 150(1):198–229, 2002. ISSN 1365-246X. doi: 10.1046/j.1365-246X.2002.01702.x. URL `http://dx.doi.org/10.1046/j.1365-246X.2002.01702.x`.

L. Tarasov, A.S. Dyke, R.M. Neal, and W.R. Peltier. A data-calibrated distribution of deglacial chronologies for the north american ice complex from glaciological modeling. *Earth and Planetary Science Letters*, 315-316 (0):30–40, 2012. Sea Level and Ice Sheet Evolution: A {PALSEA} Special Edition.

E. Thomas, T. Gapotchenko, J.C. Varekamp, E.L. Mecray, and M.R. Buchholtz ten Brink. Maps of benthic foraminifera distribution and environmental changes in long island sound between the 1940s and the 1990s. In Valerie F. Paskevich and Lawrence J. Poppe, editors, *U.S. Geological Survey Open-File Report 00-304: Georeferenced Sea-Floor Mapping and Bottom Photography in Long Island Sound*. U.S. Geological Survey, 2000.

I. Velicogna and J. Wahr. Greenland mass balance from grace. *Geophysical Research Letters*, 32(18):n/a–n/a, 2005. ISSN 1944-8007. doi: 10.1029/2005GL023955. URL `http://dx.doi.org/10.1029/2005GL023955`.

L. Wake, G.A. Milne, and E. Leuliette. 20th century sea-level change along the eastern us: Unravelling the contributions from steric changes, greenland ice sheet mass balance and late pleistocene glacial loading. *Earth and Planetary Science Letters*, 250(3-4):572 – 580, 2006. doi: http://dx.doi.org/10.1016/j.epsl.2006.08.006.

P. Wu and W.R. Peltier. Viscous gravitational relaxation. *Geophysical Journal International*, 70(2):435–485, 1982.